POLITECHNIKA GDAŃSKA

Gdansk University of Technology

Faculty of Electrical and Control Engineering

ROZPRAWA DOKTORSKA

Ph.D. Thesis

Filip Kutt, M. Sc.

Models of Brushless Synchronous Generator for Studying Autonomous Electrical Power System

Modele bezszczotkowego generatora synchronicznego do badania autonomicznego systemu elektroenergetycznego

GDANSK 2012

POLITECHNIKA GDAŃSKA

Wydział Elektrotechniki i Automatyki

ROZPRAWA DOKTORSKA

Models of Brushless Synchronous Generator for Studying Autonomous Electrical Power System

Modele bezszczotkowego generatora synchronicznego do badania autonomicznego systemu elektroenergetycznego

mgr inż. Filip Kutt

Promotor:
dr hab. inż. Mieczysław Ronkowski, prof. nadzw. PG

GDANSK 2012

The work presented in the thesis was carried out during my Ph.D. studies at the Chair of Power Electronics and Electrical Machines, Faculty of Electrical and Control Engineering at the Gdansk University of Technology (GUT), PhD grant of the Ministry of Science and Higher Education, and PhD scholarship in the frame of "Stypendia naukowe dla doktorantów, kształcących się na kierunkach uznanych za szczególnie istotne z punktu widzenia rozwoju Województwa Lubuskiego". Some parts of the work was elaborated in the frame of "More Open Electrical Technologies" (MOET) Integrated Project executed within European Commission 6th Framework Programme.

First of all, I would like to thank dr hab. inż. Mieczysław Ronkowski, prof. of GUT, the supervisor of this thesis, for his guidance and support.

Furthermore, I thank my colleagues from the Group of Electromechatronics for their support and friendly atmosphere.

Also I want to thank professor Jacek F. Gieras for his consultation and useful suggestions.

I am particularly grateful for the assistance and resources given by Mr Tadeusz Blekiewicz, Faculty of Ocean Engineering and Ship Technology of GUT. Thanks to his generosity the Chair of Power Electronics and Electrical Machines received two GT40PCz8 brushless synchronous generators. Moreover, thanks to this support I have been able to built the prototype brushless synchronous generators at very low costs.

I would like to express my gratitude to Mr. Wiesław Lis, proprietor of the company "EPiMP Maszyny Elektryczne", for his guidance and support in the design process and manufacturing of the prototype synchronous generator.

Finally, I am very grateful to my wife Iwona for her love, patience and faith. I would also like to thank my whole family, particularly my parents for their care over the years.

List of symbols:

$\boldsymbol{\psi}$	winding flux linkage
$\mathbf{i}$	winding current
$\mathbf{v}$	armature-winding voltage
P	number of magnetic poles on the machine
θ_r	rotor position angle
ϕ_s	angular displacement along the stator circumference
ϕ_r	angular displacement along the rotor circumference
k_{sfd}	armature to field turn ratio
k_{kfd}	damper cage to field turn ratio
$L_{xsxs}(\theta_r)$	armature-phase self inductance (x is a, b or c)
$\mathbf{r}_s$	armature phase resistance
$L_{xsys}(\theta_r)$	armature phase-phase mutual inductance (x is a, b or c, y is a, b or c and $x \neq y$)
L_{kqkq}	quadrature axis rotor damper self inductance
L_{fdfd}	field-winding self inductance
L_{kdkd}	direct axis rotor damper self inductance
L_{fdkd}, L_{kdfd}	field-winding and direct axis rotor damper mutual inductance
L_s	stator self inductance in (fundamental harmonic component)

L_{sf}	mutual inductance between stator and rotor field (fundamental harmonic component)
L_f	rotor field self inductance (fundamental harmonic component)
L_{skd}	mutual inductance between stator and rotor damper in direct axis (fundamental harmonic component)
L_{kd}	Rotor damper self inductance in direct axis (fundamental harmonic component)
L_{skq}	mutual inductance between stator and rotor cage in quadrature axis (fundamental harmonic component)
L_{kq}	rotor damper self inductance in quadrature axis (fundamental harmonic component)
L_{fkd}	mutual inductance between rotor field and rotor damper in direct axis (fundamental harmonic component)
L_{md}, L_{mq}	direct and quadrature-axis stator self and stator to rotor mutual inductance in arbitrary reference frame model
$\boldsymbol{f}_{abcs}$	$\boldsymbol{f}_{abcs}{}^{T} = [f_{as} \quad f_{bs} \quad f_{cs}]$
$\boldsymbol{f}_{qd0s}$	$\boldsymbol{f}_{qd0s}{}^{T} = [f_{qs} \quad f_{ds} \quad f_{0s}]$
$\boldsymbol{f}_{qdr}$	$\boldsymbol{f}_{qdr}{}^{T} = [f_{kq} \quad f_{fd} \quad f_{kd}]$
$\boldsymbol{\Psi}_{abcs}$	stator flux linkages in machine variables
$\boldsymbol{\Psi}_{qd0s}$	stator flux linkages in arbitrary reference frame variables
$\boldsymbol{\Psi}_{qd0s}$	rotor flux linkages in arbitrary reference frame variables

$\mathbf{L}_s(\theta_r)$	stator self and mutual inductances matrix
$\mathbf{L}_r$	rotor self and mutual inductances matrix
$\mathbf{L}_{sr}(\theta_r)$	stator and rotor self and mutual inductances matrix
$\mathbf{i}_{abcs}$	stator currents in machine variables
$\mathbf{i}_{qd0s}$	stator currents in arbitrary reference frame variables
$\mathbf{i}_{qdr}$	rotor currents in arbitrary reference frame variables
$\mathbf{v}_{abcs}$	stator voltages in machine variables
$\mathbf{v}_{qd0s}$	stator voltages in arbitrary reference frame variables
$\mathbf{v}_{qdr}$	rotor voltages in arbitrary reference frame variables
W_c	electromagnetic coenergy
T_e	electromagnetic torque
T_l	mechanical torque
G_x	rotational inductance (x denotes reference to inductance, e.g., G_{asas} is calculated using inductance L_{asas})
ω_{rm}, ω_r	rotor mechanical and electrical angular velocity
MMF_x	magneto motive force
A_{xs}, A_{xfd}	stator and rotor MMF harmonics amplitudes (x denotes number of harmonic)
A_{xkd}, A_{xkq}	direct and quadrature axis damper winding MMF harmonics amplitudes (x denotes number of harmonic)

$N_x(\phi_s)$, $N_x(\phi_r)$	stator and rotor winding distribution functions (x denotes a, b or c)
$\delta(\phi_s - \theta_r)$	airgap length distribution
α_d	average airgap length along d axis
α'_k	relative values of airgap distribution harmonics (k denotes harmonic number, where 1 denotes DC component)
i_m, i_{md}, i_{mq}	machine magnetising current and its components, respectively, in direct and quadrature axis
$\mathbf{K}_s$	arbitrary reference frame model transformation matrix (Clark - Park transformations)
k_{sat}	saturation coefficient
e_{0xs}	electromotive force (x denotes a, b or c)
E_{0xnyh}	electromotive force amplitude of y’th harmonic (x denotes a, b or c, and y denotes number of harmonic)

List of abbreviations:

AEPS	Autonomous Electrical Power System
GCB	Generator Control Breaker
BTB	Bus Tie Breaker
TRU	Transformer Rectifier Unit
ATRU	Auto Transformer Rectifier Unit
MEA	More Electrical Aircraft
MOET	More Open Electrical Technology
ECS	Environmental Control System
GUT	Gdansk University of Technology
BSG	Brushless Synchronous Generator
SM	Synchronous Machine
SM	Synchronous Machine
SG	Synchronous Generator
GCU	Generator Control Unit
GVR	Generator Voltage Regulator
PF	Power Factor
PMG	Permanent Magnet Generator
CF	Constant Frequency

VF	Variable Frequency
CSD	Constant Speed Drive
VS	Variable Speed
VSCF	Variable Speed Constant Frequency
IDG	Integrated Drive Generator
CHP	Combined Heat and Power
µCHP	Micro Combined Heat and Power
HF	High Frequency
MSG	Main synchronous generator

CONTENTS

1 INTRODUCTION

For many research, education and outreach programs the generation of electric energy have become collective concerns and motivating factor. It has been recognized that the development and demonstration of advanced power electronics technologies provides one of the largest opportunities for more efficient energy utilization and versatile energy generation. Presently, as the result of those opportunities, the distributed generation systems, and autonomous electric power systems (AEPS) are more and more applied. It should be underlined that high speed brushless synchronous generator (BSG) is key unit of the electromechanical energy conversion chain, particularly of the AEPS [4,10,12,23,26,31,36,42,45,54,62,64,67,83,86,88,90,94,97,100,101,104,106,109, 111].

AEPS are applied to transport systems (aircrafts, ships, hybrid and electric cars), and to land networks (at area separated from access to main electrical grid, and also in case of electrical failure). Depending on the electrical power demand the electric generators deliver power from a few kilowatts in cars, and up to megawatts on board of ships and modern aircrafts.

The two converging technologies, driving and extending the innovative ideas towards a future vision of an integrated energy system, are the transportation and electrical grids. In the future the energy conversion will be carried out electromechanically and combined with energy storage and combustion machines or hydraulics devices. As a result, different energy conversion domains can be applied and work together, either parallel or in a secondary loop, for example using electricity from waste heat (figure 1.1). Those new concepts will generate a range of new electric power systems characterised by highly demanding specifications and performance [62].

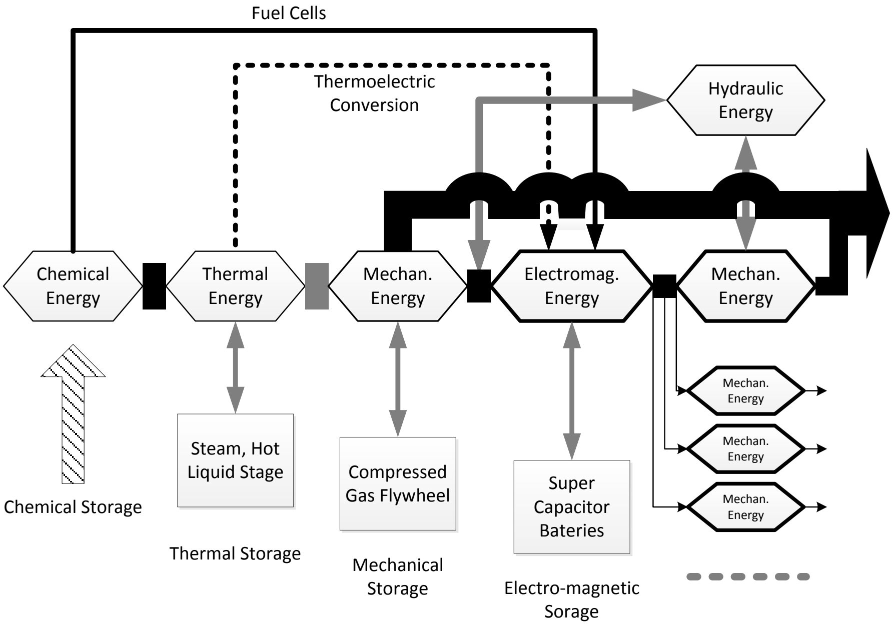

Figure 1.1 Perspective vision of a possible energy flow through an advanced AEPS [62]

Generally, the AEPS structure is not essentially different from the global electrical network, except for the number of working generators which is usually much smaller. In national or continental electrical power network the number of generators or power plants is high – from few hundred up to few thousand. In the AEPS there is usually one generator. It means that one generator has high influence on the parameters of the electric power, i.e., voltage, frequency, and also the harmonic content of voltage and current, whereas in the main continental grid it does not.

A general simplified structure of AEPS is shown in Figure 1.2. Depending upon the place where the AEPS is installed, the prime mover can be either a combustion engine in a car, ship and in a portable generator unit, or a jet engine in an aircraft, or a gas, steam and wind turbine in the local power plant.

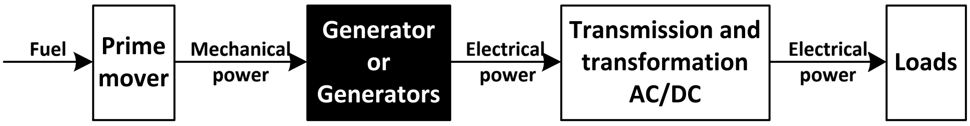

Figure 1.2 General structure of AEPS

Presently, the most advanced AEPS are applied in the avionic transport systems, particularly in the aircrafts. The AEPS have made significant advances over the years as aircraft have become more dependent upon electrically powered services [10].

At AEPS of an aircraft the power is supplied from the electric generators (at least two due to safety reasons), which are powered from the jet engines, is a particular example of the AEPS. The generator is a small part of the load of the jet engine, unlike in the land power plant where the turbo generator, the hydro generator or the wind turbine is powered from the prime mover which can deliver roughly the same mechanical power as the generator can convert into the electrical power. It means that the generator in the AESP of an aircraft operates with a variable speed depending upon the speed of the jet engine. In the older aircraft the generators were driven by a variable speed to constant speed mechanical transmission system to keep constant frequency of voltage at the AEPS. In the modern aircraft the generators work with variable speed/frequency (400-800Hz), and to keep constant frequency of voltage at the AEPS the power electronics converters are used [4,10,26,31,36,45,67,73,83,86,95,97,100,101,102,109,110].

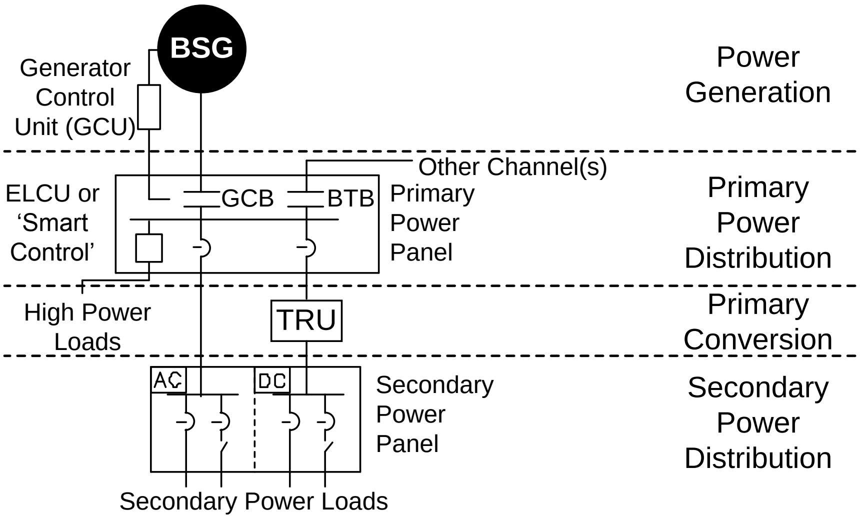

Figure 1.3 The AEPS on board of an aircraft [10]

The AEPS on board of the modern aircraft [10], as any other AEPS, is a set-up of components that allow generation, distribution and utilization of the electrical energy. In figure 1.3 the generic aircraft electrical system is shown with components such as the circuit breakers (GCB – generator control breaker, BTB – bus tie breaker), and the transformer rectifier unit (TRU).

Modern aircrafts are built on the concept of the MEA (More Electric Aircraft) [25,101]. In figure 1.4 and figure 1.5 the power distribution systems are shown, respectively, for the conventional and the MEA system.

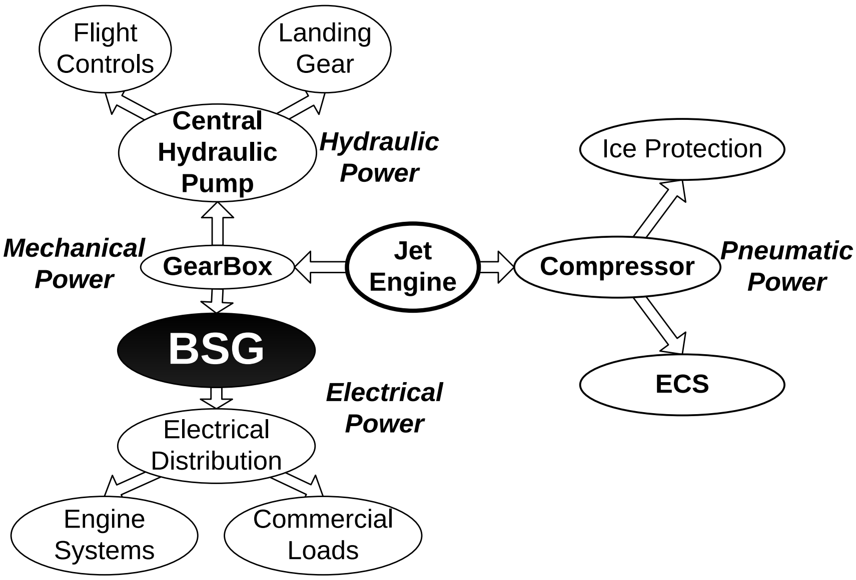

Figure 1.4 Conventional Power Distribution System of an Aircraft [67]

In the MEA system, the hydraulic system is completely replaced by the electric system [109,113], and the variable-speed gearbox is unnecessary (simple constant ratio transmission form compressor is used). The main advantage of this solution is higher reliability of the entire system. However, all units cannot or should not be replaced by an electric equipment. Systems that are crucial to sustain life, such as the ECS (Environmental Control System), and to flight safety, such as the ice protection system, are supplied by electrical and compressed/bleed[1] air systems. However, even these systems are supplied by electric power alone in the Boeing 787 “Dreamliner” (low pressure bleed air is used only for the engine cowl anti icing) [24].

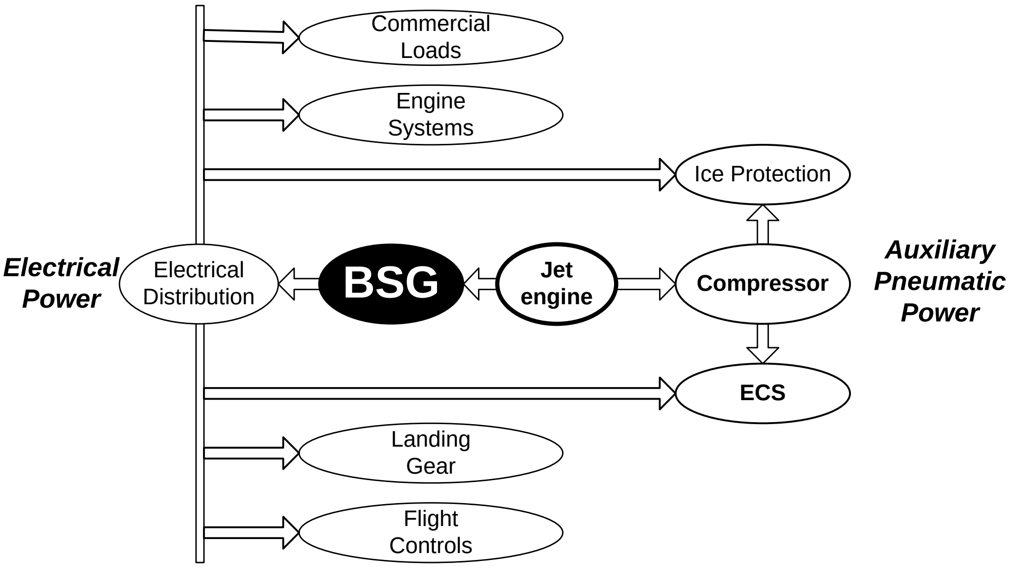

Figure 1.5 MEA Power Distribution System [67]

Nowadays large aircrafts (e.g. A330 with 300 passengers) have a total electric power demand about 250 kW. If all the functions (air conditioning, deicing, e.t.c.) of the future aircraft have to be supplied by electrical energy, then the total demands of electric power is about 1MW. Thus, a new BSGs have to be designed in order to supply such a large power demands. For the power system of the A380 a 3-phase variable-frequency generator has been designed [83]. It can also work as the jet engine starter in order to put together two functions, .i.e., it is called starter/generator (S/G). In generator mode the BSG is driven by aircraft engine using a gearbox and provides 200 kW at 230/400 V with variable frequency from 360 to 800 Hz.

Generally, in aeronautic applications the volume and weight of the power generation devices are the key issue. As it is well known, a high speed power generation devices will have the volume and weight smaller than a low speed device.

---

[1] Bleed air – compressed air taken from jet engine after the compression stage and before the fuel is injected.

On the other hand, as the consequence of the high speed operation, the centrifugal forces on the rotor and the limitation of the rotor and shaft diameters are increased [4].

High power/torque density and high efficiency are two of the most desirable features of an electromechanical generator and electromechanical actuator/motor for the aircraft power grid application. Improvement of these features has been one of the main aspects of research work on the electric machines and electromechanical actuator in the last several decades [4].

Some of the European Union countries have launched a project MOET (More Open Electrical Technologies). The MOET was charged with establishing a new industrial standard for the design of electrical system for commercial aircraft (business and regional and rotorcraft as well), based on the MEA concept. The MOET was comprised of 46 companies (13 being SMEs) and 15 Research Centers or Universities from 14 European countries. One of these participants was Politechnika Gdańska/Gdansk University of Technology (GUT). The project was coordinated by AIRBUS France. This integrated project was partially funded by the EU, through FP6 and the Framework of the Aeronautics Industry R&D Objectives. The main objective of the project was to develop the MEA and “Power by Wire” concept. It has involved changes in the power management in commercial aircrafts by replacing the hydraulic and compressed air systems by the electric system. The three-year MOET project was finished in December 2009 [113].

As continuation of the MOET project a European Conference on More Electric Aircraft MEA 2012 was organized in Bordeaux, France, in November 2012. The main scope of the conference was to present and exchange the research and development results in the fields of the new generation of wide-body aircraft, as well as a highly sophisticated electric power management, together with an increased number of all electric actuators. High power efficiency of generators, control devices and actuators as well as real-time power balancing with respect to the requirements, directly contribute to reduction of fuel consumption, and therefore pave the way to the green aircraft concepts. But increased potential sensitivity to electromagnetic compatibility hazards has to be accounted for, and even more, since composite structure is expected to spread out at the same time [112].

In the project MOET the Chair of Power Electronics and Electrical Machines, at the GUT, has been in charge of modelling of the power generation system chain, i.e., the BSG, transmission and the autotransformer rectifier unit (ATRU) for advanced “more electric” aircraft. However, due to limited access to the modelled prototype of the BSG, designed and built by Thales company [83], there were some limitations to verify experimentally the developed models.

In modern science and technology the concept of systems plays an important role; many problems in the field of AEPS are solved in a systems-oriented approach [66]. Applicability of this approach is critically dependent on the availability of adequate models, that is, such as to allow effective tradeoffs between computational speed, complexity, and accuracy. As a practical matter, the approaches to the construction of models of AEPS are principally twofold. One is to split up the AEPS into sub-systems and/or components, whose models (or submodels) are either already known from previous experience or must be developed or extended (modified). These subsystem and/or components models are then interconnected to form a model of the whole AEPS. This approach – usually referred to as the modelling – is thus chiefly analytical (mathematical). The other approach, in turn, is based on experimentation. Input and output signals of the system are measured/recorded and then subjected to data analysis in order to infer a model of the AEPS. This approach is usually referred to as the identification. Another classification of model inference methods results from the manner of handling the ever growing complexity of today's AEPS. As the simulation of sophisticated AEPS, in their entirety, tends to take impractical amounts of time, it is a common practice to avoid detailed system-as-a-whole modelling and resort to either a combination of simplified power electronics converter model and detailed BSG model, or to the inverse combination, whichever appropriate to the modelling task. The main concern in this thesis are the modelling and experimental approaches, with particular attention to various aspects of the combined power electronics converter and BSG models.

The main proposition to be justified and supported throughout the thesis has been formulated as follows:

To develop such models of BSG which, when used for studying AEPS, permit to concurrently achieve the following characteristics: sufficient computing accuracy, short computing time, and high repeatability of computations. Furthermore, such models, referred to as *multiport circuit* representation, should allow analyses of AEPS under both normal and fault operating conditions.

The lumped parameters models (referred in the literature as *circuit models*) of BSG taking into account the nonlinearity (saturation) of magnetic materials are widely described in literature [20,21,22,32,33,34,39,41,48,51,52,53,65,78,82, 84,87,89,92,93,96,99,103,107,108]. In turn, the circuit models of BSG considering the space-poliharmonic (nonsinusoidal) air-gap flux density distribution (referred in the literature as *harmonic models*) are developed using either the FEM methods [3] or indirect coupled field-circuit models approach [13]. The simplified pharmonic models are developed using either the winding function approach [35,49,74,76] or the time/frequency harmonic domain approach [30,57,68,69].

Using the FEM approach you can determine the magnetic field distribution in a considered magnetic structure of the machine. However, this method requires high computing power for the used simulation software, and the knowledge of the geometry and materials property of the considered machine is required.

The winding function approach allows to develop circuit models using the air-gap geometry, and the physical layout of the stator and rotor windings MMFs of the considered machine. However, the circuit models of the synchronous machines, taking into account both the magnetic circuit saturation and poliharmonic character of the air-gap flux density, are not generally used for studying the AEPS. Therefore, the following thesis can be formulated as following:

> **“The circuit models based studying of brushless synchronous generator performance, taking into account the magnetic circuit saturation and space-poliharmonic distribution of the air-gap flux density, provides adequate accuracy for analysis of autonomous electrical power system”.**

To prove the above thesis, the author has used an analytical and simulation approach, as well as experimental verification on the laboratory setup based on the designed and built prototype BSG with the cylindrical-rotor field.

The thesis consist of nine chapters. Chapter 1 is an introduction – the subject and scope of the thesis is presented. Chapter 2 is devoted to presentation of BSG topologies used in AEPS. Chapter 3 covers the concept and design of the prototype BSG with the cylindrical-rotor field. Chapter 4 is focused on FEM analysis of the prototype BSG. In chapter 5 the development of the BSG circuit models is presented. Chapter 6 is devoted to implementation of the developed BSG models into the Synopsys/Saber simulator. Chapter 7 is devoted to design of the test bench for experimental analysis of the prototype BSG. In Chapter 8 are presented the results of simulations and experimental analysis of the prototype BSG. Finally, in chapter 9 a summary and general conclusions are outlined. The thesis is supplemented by six appendices.

2 BRUSHLESS SYNCHRONOUS GENERATOR (BSG) IN AUTONOMOUS ELECTRICAL POWER SYSTEMS (AEPS)

2.1 INTRODUCTION

Nearly all of the electric power used throughout the world is generated by synchronous machines driven either by hydro or steam turbines or combustion engines. Just as the induction machine is the workhorse when it comes to converting energy from electrical to mechanical, the synchronous machine is the principal mean of converting energy from mechanical to electrical.

BSG has a brushless excitation system, i.e., ac exciter with rotating solid-state device (rectifier) [4,19,23,31,36,37,45,61,73,77,80,86,100,101,106]. The ac exciter is a reversed synchronous generator (field winding is stationary, and armature winding is rotating) supplying by the rotating rectifier the field winding of the main generator of BSG.

2.2 AUTONOMOUS ELECTRICAL POWER SYSTEMS

2.2.1 AIRCRAFT ELECTRICAL POWER SYSTEMS

Electrical power systems have made significant advances over the years as aircraft have become more dependent upon electrically powered services [10]. Presently, advanced BSGs are widely used in these systems. The main advantage of the brushless excitation system is a very small excitation current of the ac exciter, compared to nominal current of the main generator. This means that the generator control unit (GCU) can be much smaller and more reliable. Brushless system also requires much less maintenance, and due to the subexciter the BSG is self-excited machine. Advanced BSG are used in aircraft electrical power systems to increase its reliability and consequently the safety of the aircraft and its passengers. Topology of AEPS in aircraft has changed throughout years. Figure 2.1 shows different AC systems incorporating BSGs and DC systems incorporating

DC machines as the generators. DC systems are presently used only as a backup systems [97] and in military applications [10].

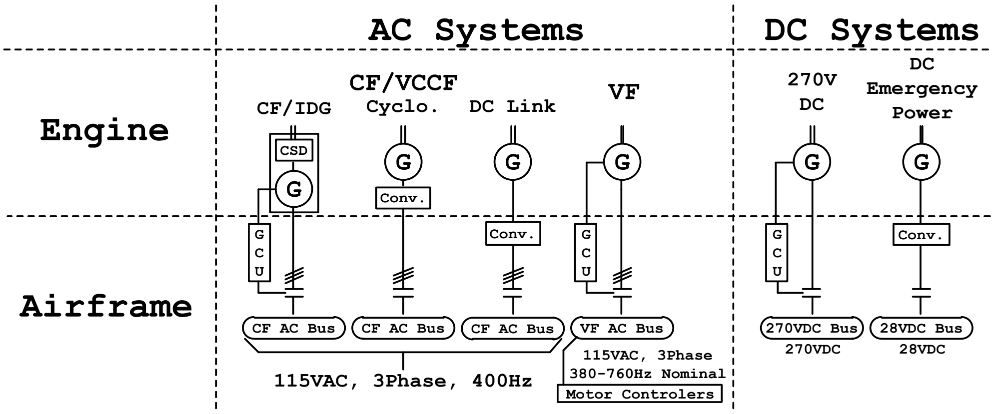

Figure 2.1 BSG applied in aircrafts AEPSs [10]

We can divide AC systems of AEPSs into two main groups: the constant frequency (CF) and the variable frequency (VF) systmes. The CF systems use either a constant speed drive (CSD), which provides constant rotation speed of the generator, or a variable speed generator (VS) with a converter. Rising demand for power in aircraft AEPSs was the reason for introducing the VF system. This system has allowed to reduce mass by abandoning the CSD. The disadvantage of the VF system is necessity to use power electronic converters for constant frequency loads (electric motors). In Table 2.1 are shown different types of generators used in civil and military aircrafts.

Table 2.1 Types of generators used in civil and military aircrafts [10]

Generation type	**Civil application**	**Military application**
IDG/CF 115 VAC/400Hz	B777 2 x 120kVA A340 4 x 90 kVA B737NG 2 x 90 kVA MD-12 4 x 120 kVA B747-X 4 x 120 kVA B717 2 x 40 kVA B767-400 2 x 120 kVA 728 2 x 40 kVA	
VSCF (Cycloconverter) 115 VAC/400Hz		F-18E/F 2 x 60/65 kVA
VSCF (DC link) 115 VAC/400Hz	B777 2 x 20 kVA (Backup) MD-90 2 x 75 kVA	
VF 115 VAC/400-760Hz typical	Global Ex 2 x 40 kVA Horizon 2 x 20/25 kVA A380 4 x 150 kVA	Boeing JSF 2 x 50 kVA X-32A/B/C
VF 235 VAC/360-800Hz	B787 4x250kVA	
270 VDC		F-22 Raptor 2 x 70 kVA Lockheed-Martin JSF X-32A/B/C 2 x 50 kVA

Development of power electronics, electrical power systems and rising consumer demand for travel comfort led to expansion of the on board electric equipment in civil as well as in military aircrafts. Concepts of MEA and MOET have led to development of power-by-wire control strategy in aircraft. For this concept the hydraulic and compressed air systems are replaced by the electrical equipment such as electro-mechanic and electro-hydraulic actuators and electric heaters for ice protection system. As a result, modern aircraft is equipped with electric generators producing up to and beyond 1MVA of electric power. Figure 2.2 shows total electrical power generated on board of different type aircrafts.

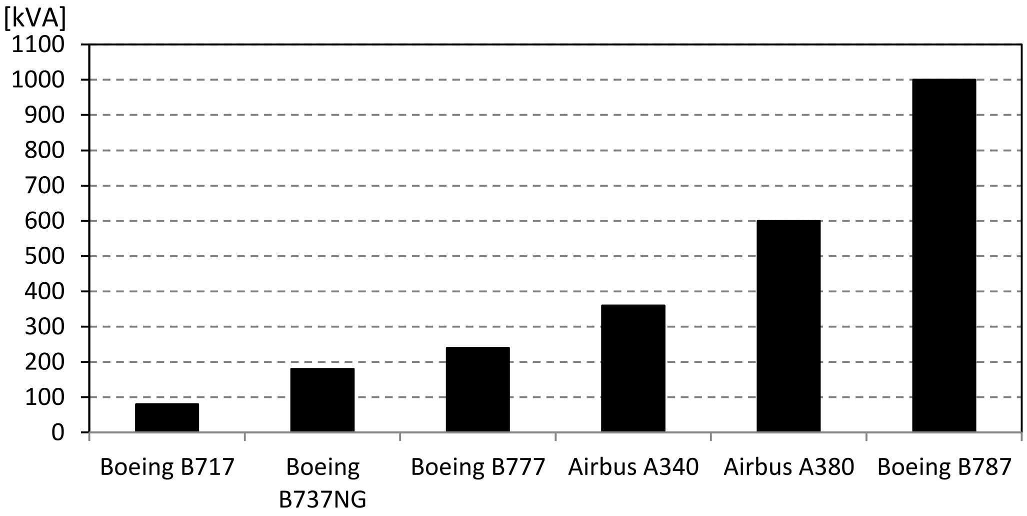

Figure 2.2 Total electrical power genrated on board of selected type of aircrafts[2]

Presently, Boeing 787 'Dreamliner' is the only aircraft developed and manufactured on the concept. Its four main generators have a power 1MVA.

Large power BSG applied in modern aircrafts are also used as starters for the jet engines. Therefore, it is referred to as starter/generator device. In order to analyse and design its control system an accurate simulation model is required to represent the complex electromechanical conversion system, taking into account in the starter/generator the magnetic circuit nonlinearity and poliharmonic distribution of the field in air-gap.

2.2.2 STATIONARY AEPS

Stationary AEPS are also fast growing part of general production of electric power [94]. The combined heat and power (CHP) systems are widely used at a global (national) level. These systems are designed to supply useful energy in terms of heat and electricity. Decentralisation of heat and electric energy production is due to main disadvantage of centralized CHP production, which are production high losses due to long distance transfer of energy from power plant to customers – homes and business centers. The micro CHP (μCHP) [64,42,88,90] systems

---

[2] Based on table 2.1.

or units are small power plants for homes. According to EU directive (92/42/EE) the µCHP unit delivers less than 50 kW. These units, installed directly in households units, are the solution for mentioned problem of high losses in transfer of energy from large CHP plants. Due to high efficiency of more than 85% of µCHP these systems allow for the reduction in greenhouse gases. They also give the advantage of decreasing utilities bills in the long term. For a single family house a system of 10kW (electrical power) is more than enough. Assuming that the µCHP units are designed primly as heaters, and additionally to deliver a fraction of electrical energy required by household, a system of 6kW (heat) and 1kW (electrical), i.e., 6 to 1 ratio, is usually enough. Figure 2.3 shows typical application of µCHP unit in single family house.

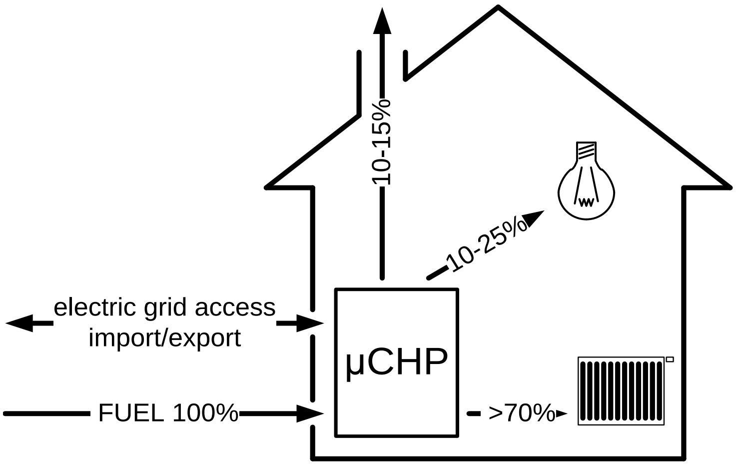

Figure 2.3 Typical application of micro CHP in single family house [42,111]

The most common solution of prime mover for electric generator in µCHP unit is a Stirling engine [12], which operates using difference of temperatures of media on the input and output of furnace. Also combustion engines are widely used due to simplicity and low cost of construction. Figure 2.4 shows different types of cogeneration technologies used in µCHP units.

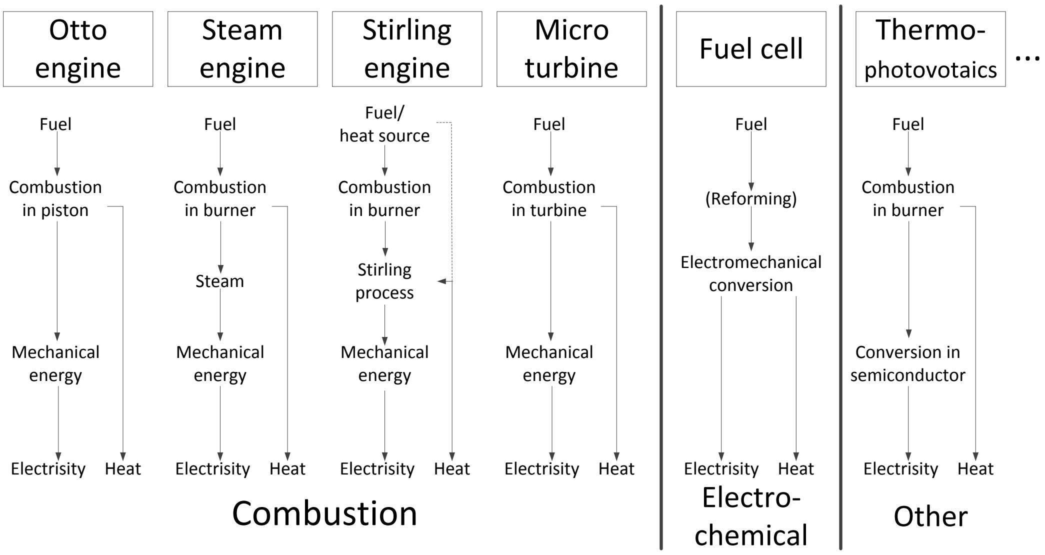

Figure 2.4 Types of cogeneration technologies used in µCHP units [12]

2.3 GENERATORS USED IN DIFFERENT TYPES OF AEPSS

Generally, in aircraft AEPSs two or more BSGs are used. A general structure of the modern BSG is shown in Figure 2.5. BSG has a brushless excitation system, i.e., ac exciter with rotating solid-state device (rectifier) [4,19,23,31,36,37,45,61,73,77,80,86,100,101,106]. The ac exciter is a reversed synchronous generator (field winding is stationary, and armature winding is rotating) supplying by the rotating rectifier the field winding of the main generator of BSG. Apart from the main generator and the ac exciter, there is also a third element – subexciter, i.e., a permanent magnet generator (PMG) supplying the stationary field winding of the ac exciter. Due to the subexciter the BSG is self-excited machine.

In different types of aircraft AEPSs the BSG can have a slightly different stucture. In VF system the BSG has 3-phase main generator, whereas in VSCF system is used a 6-phase main generator that is combined with cycloconverter (figure 2.6). In IDG/CF system a 3-phase main generator is applied and it operates with constant frequency.

In all mentioned above BSG the ac exciter can also have 3 or 6-phases with diode rectifier of 3 or 6 diodes respectively or bridge rectifiers, respectively.

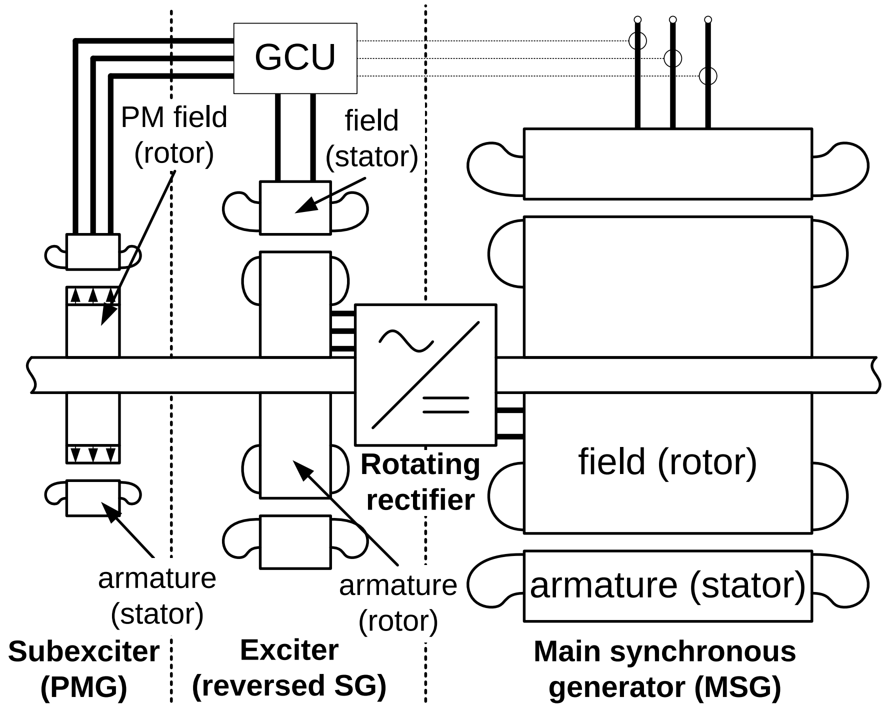

Figure 2.5 Structure of modern BSG

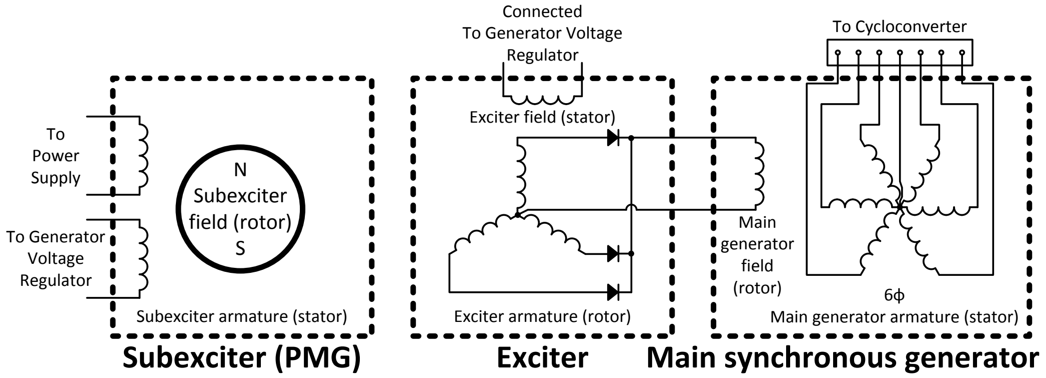

Figure 2.6 Electrical schematic of VSCF using BSG [10]

The generator control unit (GCU or GVR – generator voltage regulator) is supplied by subexciter (PMG) and controls the main generator voltage by changing the excitation current for the stationary field of the ac exciter.

In the µCHP units different types of prime movers for electric generator are used. This leads to wide operation range of generator speed from 1000 to 100000 rpm. Figure 2.7 shows common generators used in µCHP units.

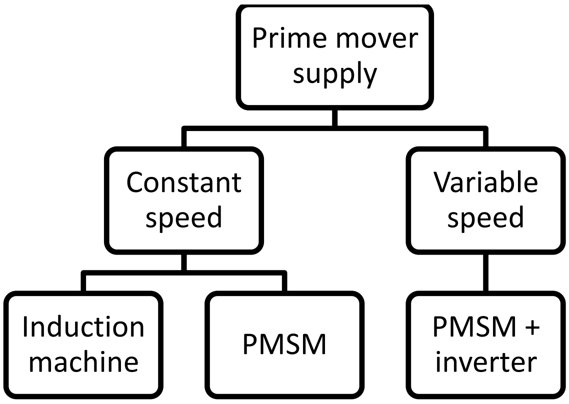

Figure 2.7 Common types of electrical machines used as generators in the µCHP units [4]

In systems equipped with Stirling engine two types of PMG are used – rotational (Honda FreeWat) and linear (MicroGen), and the induction motor (WhisperGen). These systems, similarly as those with internal combustion engine (Otto engine), can operate as units of constant speed or variable speed with speed ranging from 1k to 10k rpm. In case of stem or gas micro turbines the rotational speed is from 50k up to few hundred thousand rpm. These systems use high speed PMG and inverter to fed the home electrical appliances. It is also possible to use electrically excited synchronous generator, in all systems presented on figure 2.4. In constant speed units the SG can correct the power factor and in variable speed units it can also maintain constant voltage.

2.4 SELECTED BSG FOR CONSIDERATIONS

In this thesis, basing on the MOET project experience, a 3-phase BSG dedicated to VF systems has been selected for modelling and analysis. Generally, the rated power of BSG used in MEA systems is in the range up to 250kVA. However, due to limited funds received for the thesis a prototype BSG has been designed and build as a scaled model.

2.5 TYPES OF MODELS OF BSG REQUIRED FOR AEPS DESIGN AND ANALYSIS

For the evaluation of aircraft on-board electric power systems and electric servosystems with regard to their weight, behaviour and reliability novel modelling and simulation tools are being developed. The tools are intended for use in the analysis and conceptual design and of such electrical systems. Diverse methodologies are integrated in the tools to cover the mentioned aspects at the same time. The tools consist of dedicated model libraries containing object-oriented, physical models of electrical power system components.

The model libraries are hierarchically structured to accommodate various models of different complexity, such as interfaces (plugs, databuses, etc.), basic electrical components (wiring, contactors, busbars, etc.), more integrated electrical components (generators, rectifiers, converters, etc.), power users (motor drives, heatings, etc.) and entire system architectures. Thus, the libraries provide an infrastructure for the elaboration or adaptation of simulation models of electrical system structure [58].

Generally, considering the four modelling levels of MEA power system, the four types of models can be characterized, as shown in Figure 2.8.

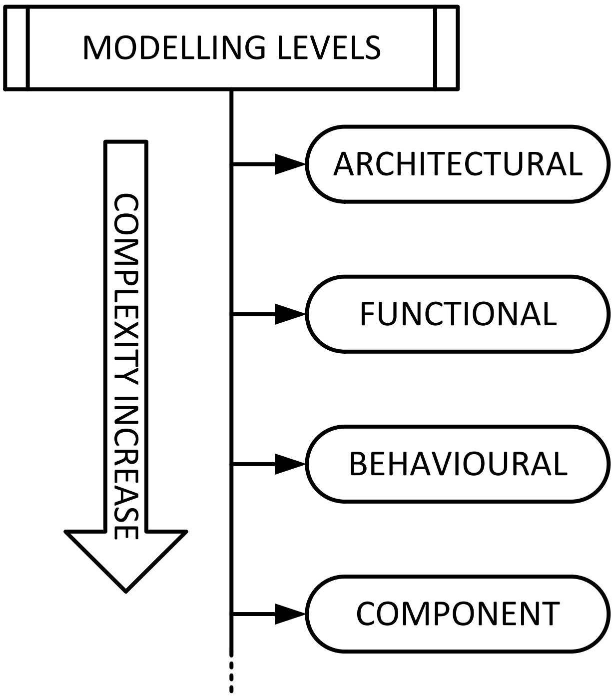

Figure 2.8 Schematic of MEA power system modelling levels

At the architectural level the models represent the steady-state power consumptions (no dynamic response). The models are usually used for power budget studying.

At the functional level the models represent the steady-state power consumptions and transient behaviour (inrush current, energy consumption dynamics with regards to input voltage transients, etc.). Such models do not include switching. The band frequency to be modelled is between 0 to 133Hz for periodic phenomena. The models are usually used for network logic and network stability studying.

At the behavioural level the models are detailed functional models. They represent the actual dynamic waveforms, i.e., the same representativeness as the functional model ones, and the full representativeness of the waveforms (switching, HF rejection, etc.). Nevertheless, the phenomena above 250 kHz shall not be included. The models are usually used for network power quality studying.

At the component level the models include a representative model of each single component of the MEA system or sub-system. The models are usually used for verification of local operation, and deep analysis of each component behaviour.

Other general requirements for the equipment model are following:

- the model must have links to external environment, i.e., input and output power interfaces/ports representative of the real equipment in terms of electrical and/or mechanical behaviour (steady state and transient response).
- the model shall be easily integrated in a global network test bench at aircraft level and shall not induce any specific parameters request which could be not compatible with other equipment models.
- the equipment models shall be fully representative of the electrical and/or mechanical behaviour with regard to the electrical network and/or mechanical characteristics, while building the global models of AEPS.
- the behaviour of AC 3-phase models shall be representative in case of phase loss scenarios/faults.

One essential requirement for a simulation of AEPS consisting of many nonlinear components is high computational efficiency. A key technique in achieving this is the use of an advanced network solver such as Synopsys/Saber and the modelling language MAST [58].

2.6 SUMMARY.

The importance of BSG performance in AEPS has been well recognized. BSG are highly nonlinear, complex electromechanical device, whose dynamic behaviour directly impacts the performance and reliability of the EEPS network. Apart from providing the ultimate electricity source, the BSG are usually used to start the turbine engine. To analyse the dynamic behaviour of the BSG, an effective and accurate simulation model is desired. Further, the model needs to account for dynamics involving electrical and mechanical domains [58].

To gain the above mentioned goals the next chapters of thesis focuses on:

- concept and design the prototype BSG with cylindrical-rotor field;
- carrying out FEM analysis of the design prototype BSG;
- development the circuit models of BSG;
- implementation the developed BSG models into the Synopsys/Saber simulator;
- concept and design the test bench for experimental analysis of the prototype BSG;
- carrying out simulations and experimental analysis of the prototype BSG, and verification the developed models.

3 CONCEPT AND DESIGN OF PROTOTYPE BSG

3.1 INTRODUCTION

The BSGs applied in AEPS work with variable frequency on board of a modern aircraft-has high rotation speed ranging from 8000 to 16000 rpm, and sometimes even more. Due to high speed operation the cylindrical-rotor field (smooth-air-gap) structure of the main generator is more adequate than salient-pole field used in constant frequency BSG with a CSD [83,110,50].

At the first step the main generator of the considered BSG was designed using the ratings of the Thales MEGEVE generator [50,83,110] as references parameters. In Table 3.1 are shown main electrical and mechanical parameters of the main generator of MEGEVE.

Table 3.1 Parameters of the main generator of BSG designed at the first step

Number of phases:	3
Connection of armature winding:	wye (Y) with neutral point (N)
Armature line voltage:	400 V
Armature line current:	289 A
Rated power:	200 kVA
Rotating speed	7600 - 16000 rpm
Frequency	380 - 800 Hz
Number of poles	6

The Thales MEGEVE BSG as well as the Goodrich BSG have been used for modelling, simulations and experimental treatment in the frame of the MOET project for the development of MEA. In Figure 3.1 are shown the dimensions of designed main generator. The calculated core length l of this main generator is $\text{equal to } 200\text{mm}$. However, the parameters of this generator, especially power and rotational speed, would make it very expensive to build. It would generate not only high cost prototype but also high-priced and large test bench.

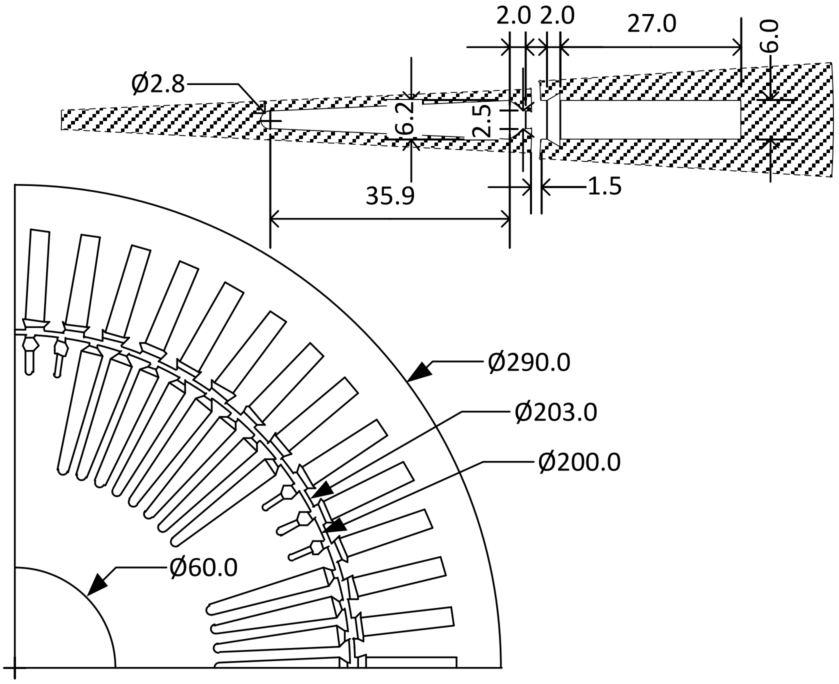

Figure 3.1 The rotor dimensions of the main generator of BSG designed at the first step - hales MEGEVE generator is taken as references machine

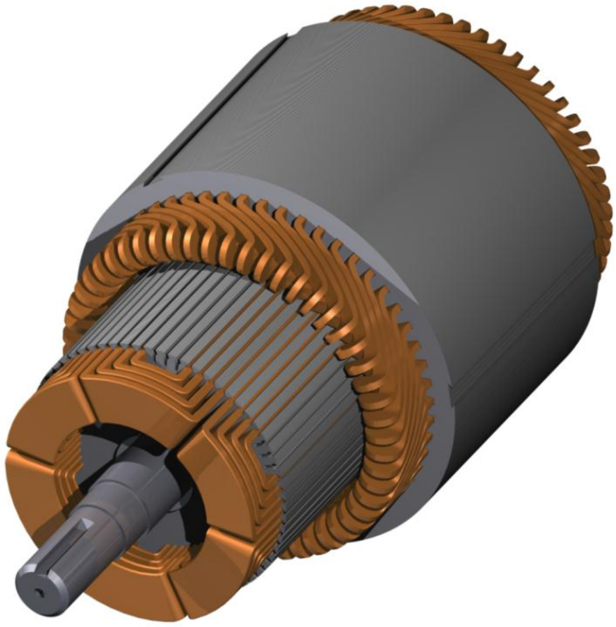

Figure 3.2 View of the main generator of BSG designed at the first step - Thales MEGEVE generator is taken as references machine

Due to insufficient funds for this thesis a prototype BSG was designed as scaled machine and built using parts of commercial salient-pole BSG type of GT40PCz8. It is Russian product used in MI-28 helicopter and its original name is ГТ40ПЧ8. The field core and the excitation winding of its main generator was replaced by a newly designed cylindrical-rotor field. Unfortunately, because only one part of the GT40PCz8 machine was redesigned, and its exciter and subexciter are designed to operate at the nominal speed 8000rpm, the prototype BSG could have been tested at speed not higher than nominal. On the other hand, this has given an opportunity to compare the tests results of the commercial GT40PCz8 (salient-pole field) and the prototype BSG (cylindrical-rotor field) at the same nominal speed.

Assumed approach to design process was based on the assumption that the cylindrical-rotor field of the main generator should have a high number of slots and the field winding is sinusoidally distributed. Due to assumed a high number of slots it was also possible to achieve a higher rotational speeds than the original one, because the centrifugal force is more equally balanced.

3.2 SPECIFICATION OF THE GT40PCZ8 GENERATOR

GT40PCz8 generator has a rated apparent power 40kVA and constant speed 8000 rpm, and is combined of the main generator, ac exciter and subexciter (PMG) at the common shaft.

In Table 3.2, table 3.3 and table 3.4 are shown data of the GT40PCz8 machine. The main generator excitation current the excitation current of the ac exciter are practically equal. The rated value of current of the main generator field winding is not given in the documentation of GT40PCz8 machine. Using analytical calculations and FEM simulation its was evaluated to be approximately 30 times greater than the ac exciter field current, i.e., about 60 A at the rated load of GT40PCz8 machine.

Table 3.2 Main generator data (ratings) of GT40PCz8

Number of phases:	3
Connection of armature winding:	wye (Y) with neutral point (N)
Armature line voltage:	208 V
Armature line current:	111A
Rated power:	40 kVA
Power factor:	0.8
Rotating speed	8000 rpm
Frequency	400 Hz
Number of poles	6
Excitation current	<= 1.9 A

Table 3.3 AC exciter data (ratings) of GT40PCz8

Number of phases:	6
Connection of armature winding:	wye (Y) with six rotating diodes
Rotating speed	8000 rpm
Frequency	800 Hz
Number of poles	12
Excitation current	2A

Table 3.4 Subexciter data (ratings) of GT40PCz8

Number of phases:	3
Connection of armature winding:	wye (Y)
Armature line voltage at no-load:	47V+4V/-2V
Armature line current (continuous):	<= 2 A
Rated power (continuous) :	170 VA
Rotating speed	8000 rpm
Frequency	800 Hz
Number of poles	12
Excitation	Permanent magnets

Detailed documentation of the GT40PCz8 machine is given in appendix A. The used design procedure of the cylindrical-rotor field for the main generator has been described in detail in appendix B.

3.3 DESIGN OF MAIN GENERATOR WITH CYLINDRICAL-ROTOR FIELD

The machine GT40PCz8 with salient-pole filed of the main generator cannot operate with speed higher than 8000rpm. The newly design cylindrical-rotor field of the main generator for the prototype BSG could reach speed up to 16000 rpm, if the ac exciter and subexciter of the machine GT40PCz8 were also redesigned. Due to limited funds of this thesis for building the prototype BSG, the unmodified parts of GT40PCz8 machine, such as the PMG subexciter, ac exciter and the armature of the main generator have been used [95]. On the other hand, this gives opportunity to compare two BSGs having different structures of the main generator field, i.e., salient pole and cylindrical (non-salient pole) rotors. This comparison can show the advantages and disadvantages of either of them, and also, what is more interesting, to compare the of simulation and measurement results for the both generators.

In Fig. 3.3 are shown the rating data overview of the selected structure of GT40PCz8 generator.

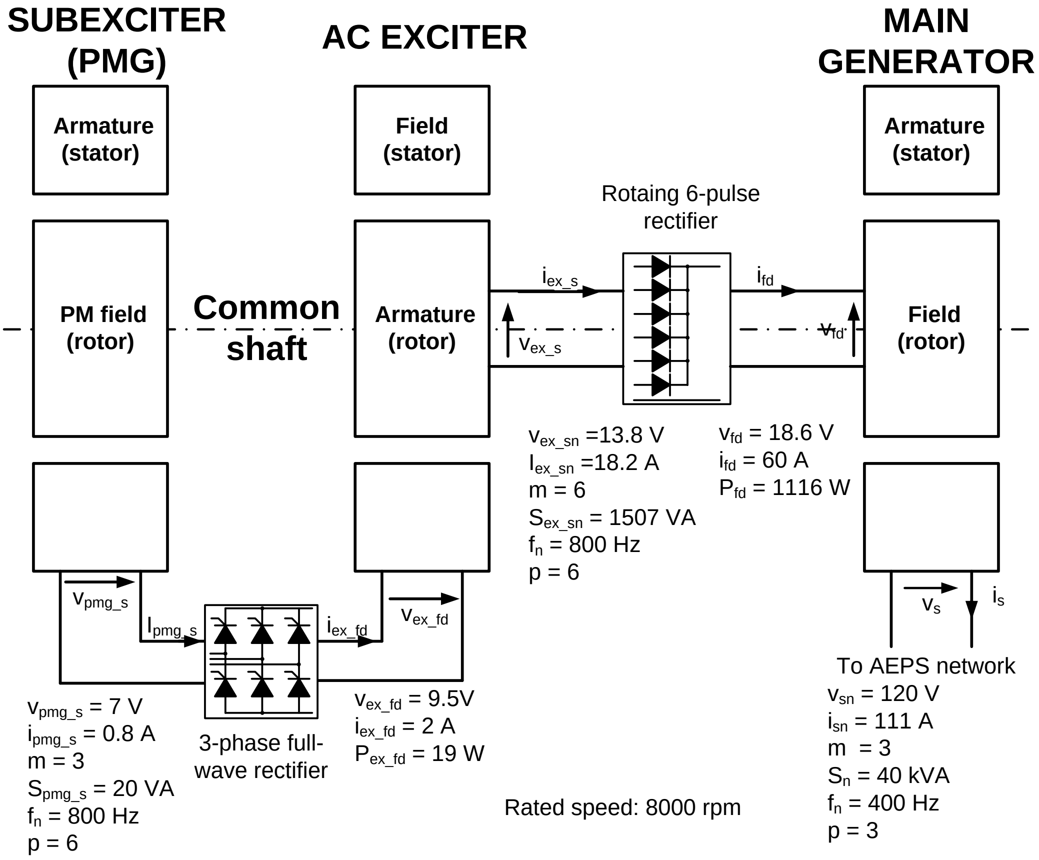

Figure 3.3 Rating data overview of the selected structure of GT40PCz8 brushless synchronous generator

Figure 3.4 shows dimensions of the armature core which is the unchanged part of the designed prototype BSG. The main generator armature slots are skewed by three times stator slot: $\alpha = 13.3(3)^\circ$.

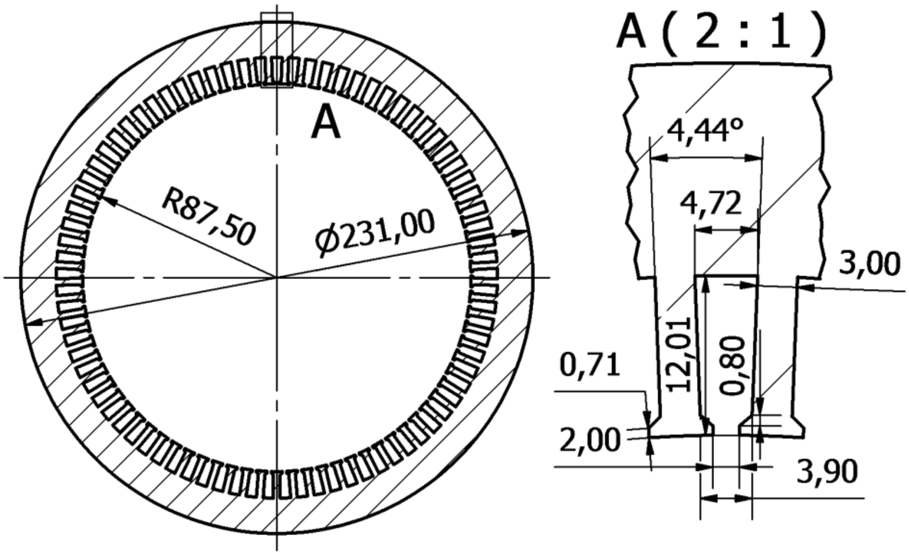

Figure 3.4 Stator core dimensions of the main generator of GT40PCz8

The main dimensions of the main generator armature core are presented in table 3.5.

Table 3.5 Main dimensions of the main generator of GT40PCz8

Parameter	Value	Description
D_s	231mm	Inner diameter of the stator
D_{es}	175mm	Outer diameter of the stator
l	73mm	Core length
δ	0.6mm	Airgap length

The armature winding parameters are presented in table 3.6.

Table 3.6 Armature winding parameters of the main generator of GT40PCz8

Parameter	Value	Description
Q_s	81	Number of stator slots
N_s	27	Number of armature winding turns/phase
Θ_s	1160A	Fundamental component of armature MMF at nominal load
S_{cs}	7mm^2	Cross-section area of armature winding conductor

The armature coils are made of two profile wires in parallel each of them having $1 \times 4.5 = 4.5mm^2$ and the total cross section of armature winding is $7mm^2$. Number of slots per pole per phase is:

$$q = \frac{Qs}{2p \times m} = \frac{81}{6 \times 3} = 4.5 \tag{3.1}$$

The rated armature winding current density is $J_s = I_s/S_{cs} = 111/7 \approx 16\frac{A}{mm^2}$. Therefore, the machine is cooled using compressed air. Figure 3.5 shows the plane view of one phase armature winding.

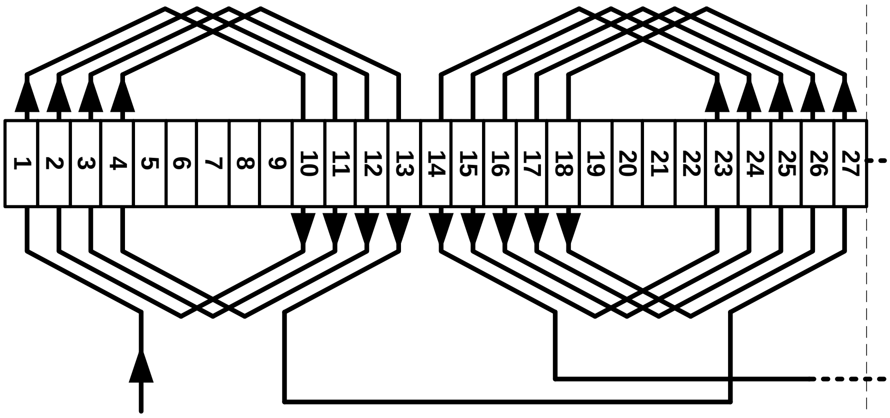

Figure 3.5 Plane view of one phase armature winding: 1/3 of main generator armature (2 of 6 coil)

Armature winding is a two-layer winding and each slot contains only one turn of each two coils that goes into it. There are three coils having 4 turns each, and three coils having 5 turns each, connected in series for each phase.

The field of the main generator was designed on the base of the main dimensions: inner and outer diameter of the original part of generator GT40PCz8. Figure 3.6 shows two types of the field ferromagnetic sheets of the main generator. Salient pole (A) is the original main field of GT40PCz8 machine. Cylindrical-rotor (non-salient pole) (B) is the designed and built prototype field.

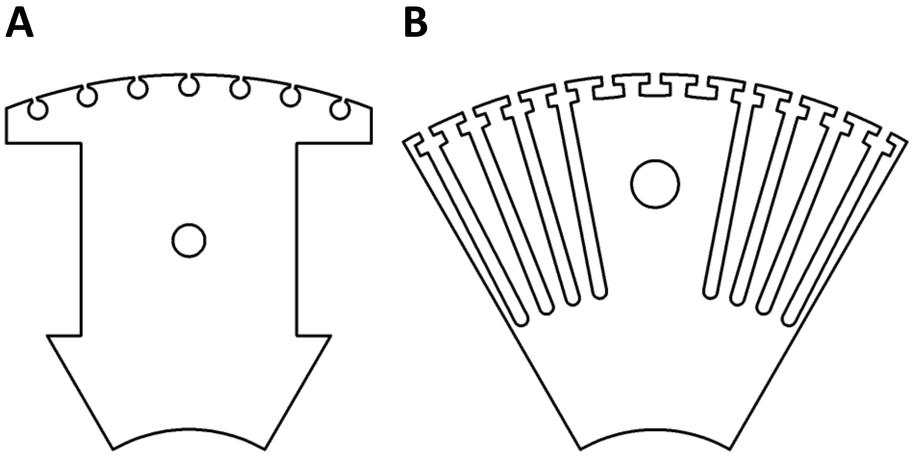

Figure 3.6 Two types of the main generator field (1/6 of the sheet is shown): A – salient-pole (original) rotor, B – cylindrical-rotor (newly designed)

Figure 3.7 shows dimensions of the developed cylindrical-rotor of the main generator.

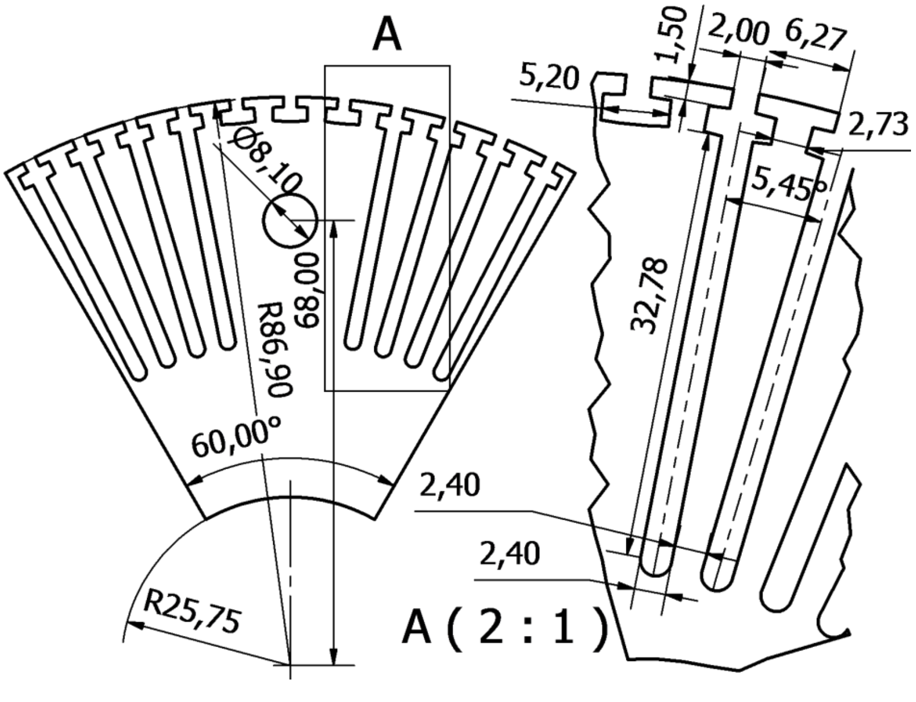

Figure 3.7 Dimensions of the cylindrical-rotor of the prototype main generator

Table 3.7 shows the dimensions of the cylindrical-rotor of the prototype main generator.

Table 3.7 Main dimensions of the cylindrical-rotor of the prototype main generator

Parameter	Value	Description
D_r	$173.8\mathrm{mm}$	Outer diameter of the main generator rotor
D_{ri}	$51.5\mathrm{mm}$	Inner diameter of the main generator rotor
l	$73\mathrm{mm}$	Core length
δ	$0.6\mathrm{mm}$	Air-gap length

Analytical procedure used to design the cylindrical-rotor of the prototype main generator are presented in appendix B. The field winding of the of the main generator of GT40PCz8 has 42 turns per pole. Since the original main generator and the prototype main generator have the same air-gap length, but different effective air-gap length (due to influence of the exciter core in quadrature axis), the number of rotor coil turns in the cylindrical-rotor field is 40 turns per pole.

Table 3.8 Field winding parameters of the cylindrical-rotor of the prototype main generator

Parameter	Value	Description
I_f	$45\mathrm{A}$	Calculated value of the excitation current of the Main Generator under nominal load.
Q_f	48	Number of rotor slots
N_f	240	Number of field winding turns (all poles in series)
Θ_f	$2400\mathrm{A}$	Field current linkage at nominal load (one pole)
S_{cf}	$4.5\mathrm{mm}^2$	Cross-sectional area of field winding conductor

The field winding current density is $J_f = I_f/S_{cf} = 45/4.5 \approx 10\frac{A}{mm^2}$.

The designed field of the main generator has in direct axis a damper cage made of brass. The cage is inserted into three slots on a large tooth of each pole. The shape of the filed teeth was selected for profile wire of field winding and simple shape of slots wedges. The magnetic core of designed cylindrical rotor is assembled of sheets like these shown in figure 3.8. The sheets are riveted together through holes in large tooth of each pole.

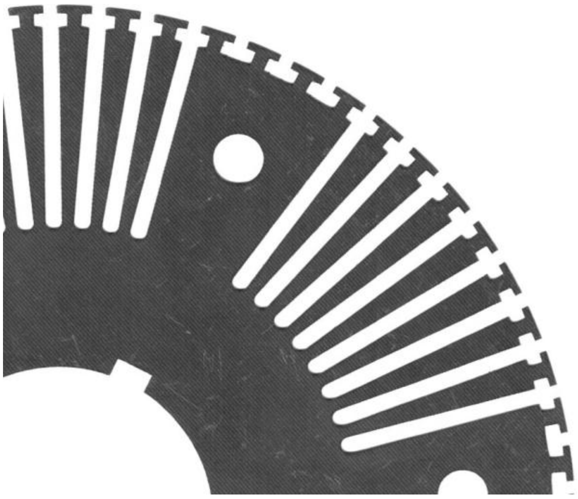

Figure 3.8 Part of the sheet of the cylindrical-rotor of the prototype main generator

Steel sheets used for rotor core are cut from standard generator steel type M530-50A-241. The steel was bought from the Celma Cieszyn – producer of electric machines (part of Cantoni group). Thickness of the sheets is $0.5mm$.

3.4 SUMMARY

Due to insufficient funds for this thesis a prototype BSG has been designed as a scaled machine, and built using parts of commercial salient-pole BSG – type GT40PCz8. The field core and the field winding of its main generator was replaced by a newly designed cylindrical-rotor field. On the other hand, this has also given opportunity to compare two BSGs having different structures of the main generator field, i.e., salient-pole and cylindrical (smooth air-gap) rotors. The comparison studying, using simulation and measurement results, can show advantages and disadvantages either of them.

The design approach was based on the assumption that the cylindrical-rotor field of the main generator should have a high number of slots and sinusoidally distributed field winding. Due to high number of slots it was also possible to achieve a higher rotor speed than the original one, because the centrifugal force is more equally balanced for cylindrical-rotor field.

In the next chapter of thesis the FEM analysis of the prototype BSG are carrying out to verify its parameters obtained by analytical calculation.

4 FEM ANALYSIS OF THE PROTOTYPE BSG

4.1 INTRODUCTION

The prototype BSG designed in the previous chapter shall be verified using finite element method (FEM) [105]. A series of simulations is carried out using the FLUX2D software. The generator geometry is drawn using Python script. The script is not depend upon the version of the FLUX2D software, if the FLUX2D supports Python scripts. Therefore, the generator simulations are more versatile. Results of FEM simulation, presented in this chapter, are used to verify the calculated dimensions and parameters of the prototype BSG.

4.2 VERIFICATION OF THE DESIGN USING FEM

In Figure 4.1 is shown meshed geometry of the simulated prototype main generator. Due to two layer stator winding, it was necessary to draw 1/3 of the machine pole pair. For stator and rotor slots a rectangular mesh was used, and for other surfaces of the machine geometry a triangle mesh was used.

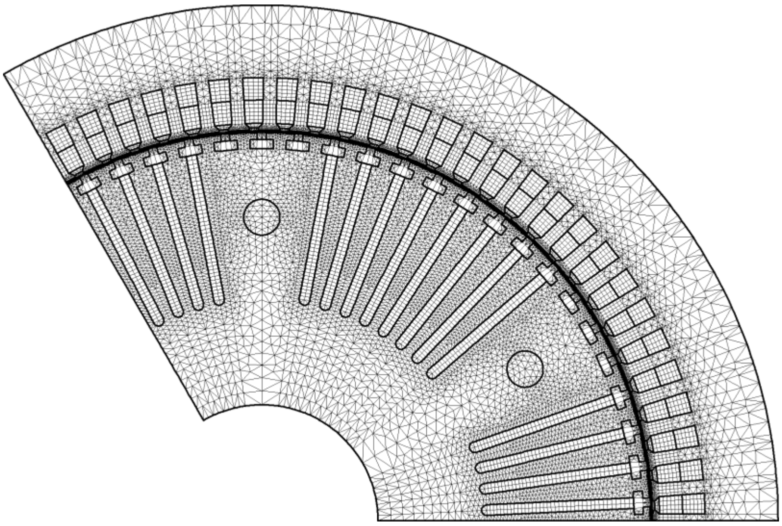

Figure 4.1 Meshed geometry of 1/3 part of the prototype main generator

For the FEM simulations a magnetic materials with different parameters were chosen for the stator and the rotor cores, respectively. The material chosen for the stator has at beginning relative permeability μ_r=8000, and saturation magnetization 1.6 T. The parameters of the rotor core, due to laser cutting of the steel sheets, have significantly changed magnetic characteristic of the rotor core in the teeth area. The rotor permeability was evaluated using the data of M530-50A steel sheets (at beginning μ_r=500 and the saturation magnetization 1.55T).

Due to those diminished parameters of the magnetic core of the main generator, the field current for the no load and nominal load performance have to be changed. Using FEM calculations it was evaluated as follows: $28A$ for no load, and $60A$ for nominal load, respectively.

Results presented in this section are only a part of carried out simulations. More detailed results of the FEM simulations of the considered generator are presented in appendix C.

The simulation results of the main generator are presented for two loads: no load ($I_s = 0, I_f \cong 0.5 I_{fn}$), and nominal load ($I_s = I_{sn}, I_f \cong I_{fn}, \cos(\varphi_n) = 0.8$).

In Figure 4.2 and figure 4.3 are show the results of simulation at no load conditions. For this simulation the field winding is only supplied by about 50% of nominal field current. The fundamental component amplitude of the airgap flux density for this load condition is $0.76\mathrm{T}$.

In Figure 4.4 and figure 4.5 are shown simulation the results for nominal load. For this simulation the field winding is supplied by nominal current ($60A$), and the armature is loaded by rated current with power factor 0.8. The fundamental component amplitude of air-gap flux density for the nominal load condition is $0.76\mathrm{T}$.

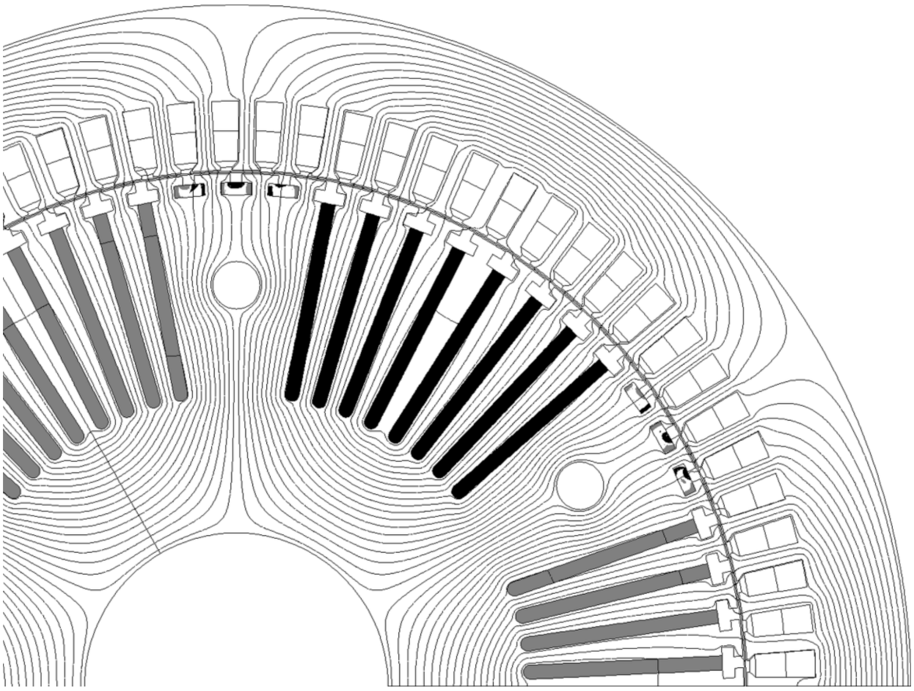

Figure 4.2 Current density (shades: black – negative direction of current, grey – positive direction of current) and equipotential lines for no load conditions: $I_s = 0, I_f = 28A$

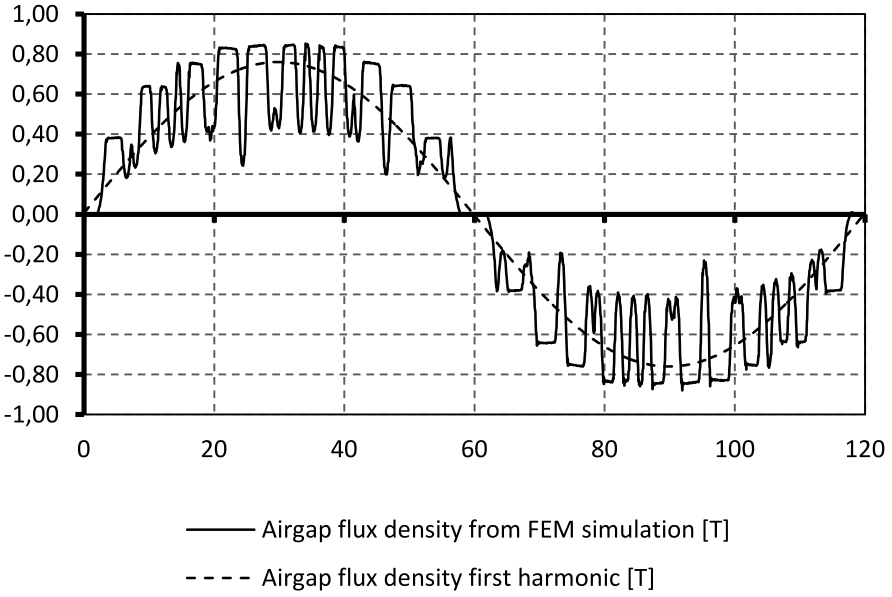

Figure 4.3 Air-gap flux density (normal component) versus rotor position angle for no load conditions: $I_s = 0, I_f = 28A$

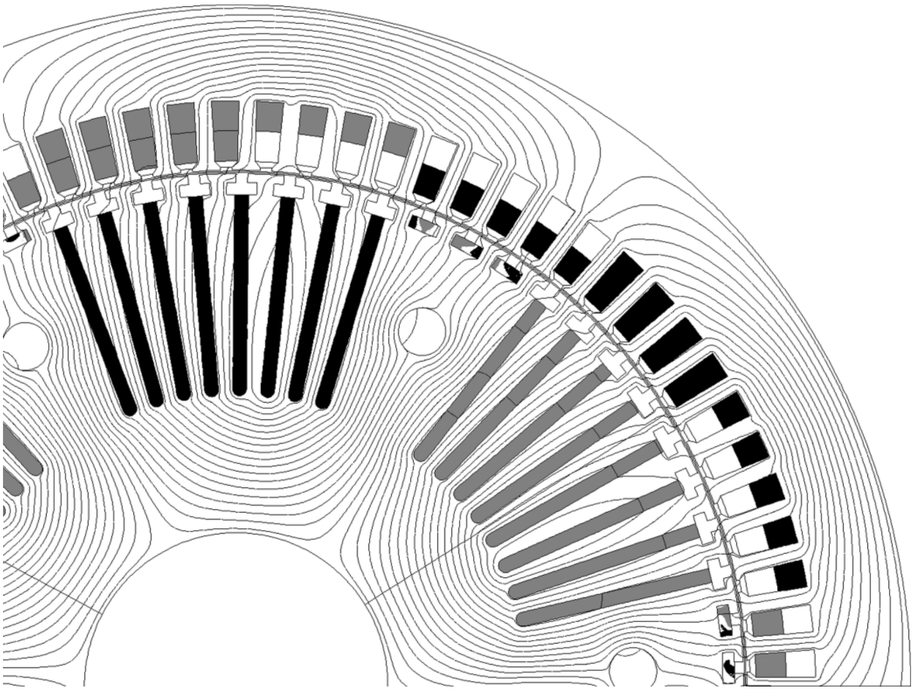

Figure 4.4 Current density (shades: black – negative direction of current, grey – positive direction of current) and equipotential lines for nominal load conditions: $I_s = 109A, I_f = 60A, \cos(\varphi_n) = 0.8$

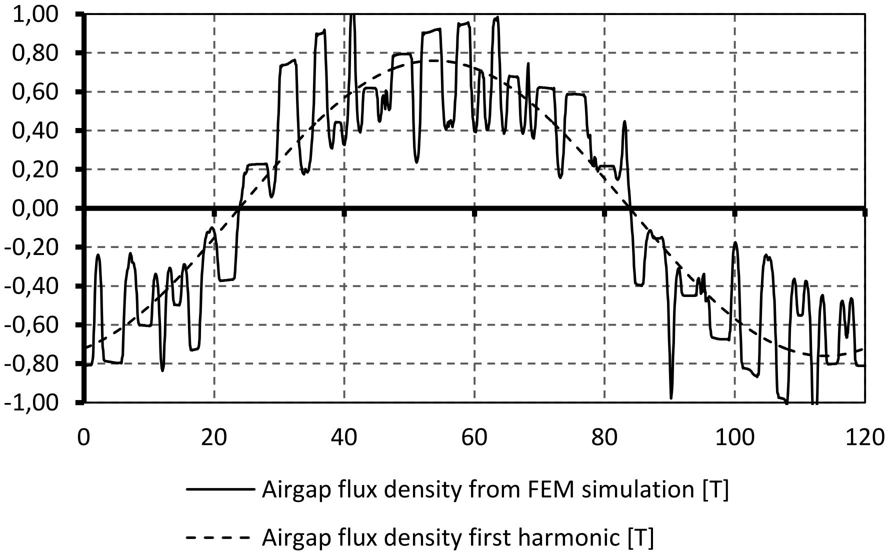

Figure 4.5 Air-gap flux density (normal component) versus rotor position angle for nominal load conditions: $I_s = 109A, I_f = 60A, \cos(\varphi_n) = 0.8$

The maximum values of flux densities of the prototype main generator are presented in table 4.1.

Table 4.1 Maximum values of flux densities of the prototype main generator

Part of magnetic circuit	Value [T]
Air-gap	0.8
Stator yoke	1.35
Stator tooth	1.55
Rotor yoke	1.1
Rotor tooth	1.65

4.3 SUMMARY

The parameters of the main generator of the prototype BSG (designed in the previous chapter) have been verified using FEM software (FLUX2D). Similar studying were carried out for the ac exciter and PMG subexciter. Commercial salient-pole main generator (GT40PCz8) has also been studied to verify some assumptions taken for FEM analysis, such as current densities and number of turns of the unmodified parts of the prototype BSG.

The prototype BSG with the cylindrical field is characterized by a higher compactness, i.e., its mass/volume factor is relatively small, compared to the BSG with the salient-pole field. Moreover, its no-load phase voltage, and the phase voltage and line currents under load, should contain less higher harmonics than the voltages and current of the silent-pole generator.

The carried out design and magnetic field analysis of the prototype BSG are very reliable, due to the application of the two approaches: analytical (based on the sizing equations) and numerical (using field simulator FLUX2D). Using the two approaches in this thesis you could avoid the additional costs of building farther prototypes of the machine under design.

The next chapter of this thesis is devoted to the circuit models development of the BSG for studying AEPS.

5 MODELS DEVELOPMENT OF BSG

5.1 INTRODUCTION

This chapter focuses on development of the following models of the BSG:

- functional level model;
- behavioural level model.

The functional level model is developed using space-monoharmonic model of synchronous machine, i.e., sinusoidal air-gap flux density distribution is assumed. The model port variables are described in arbitrary reference frame *qd*0 [7,44,48,58,59,60,81,91,98]. The Lumped parameters of this model are assumed constant. The model is devoted to represent simple performance states of the BSG in the AEPS, as described in chapter 2.

The behavioural level model is described in machine variables [7,11,15,49,85,104]. It represents the real electrical and mechanical port variables of the BSG. For this model the physical phenomena such as space-poliharmonic (nonsinusoidal) air-gap flux density distribution and magnetic material saturation can be taken into account.

5.2 GENERAL CONSIDERATION ON BSG MODEL STRUCTURE

A general model structure of considered BSG is shown in Figure 5.1. The BSG can be defined as a multiport electromechanical converter/transducer having electrical and mechanical ports. For the generator performance the mechanical energy is supplied to the shaft, and the excitation field energy is supplied to the field winding of the main synchronous generator (MSG) by the exciter. The internal structure of the MSG model describes: transformer couplings, electromechanical couplings, energy accumulation and energy dissipation.

For the MSG the electrical ports are described by voltages ($\mathbf{v}_{abcs}$ – stator, $\mathbf{v}_{fd}$ – rotor) and currents ($\mathbf{i}_{abcs}$ – stator, $\mathbf{i}_{fd}$ – rotor), in turn the mechanical port is described by rotor mechanical angular velocity (ω_{rm}) and mechanical torque ($\mathrm{T_l}$).

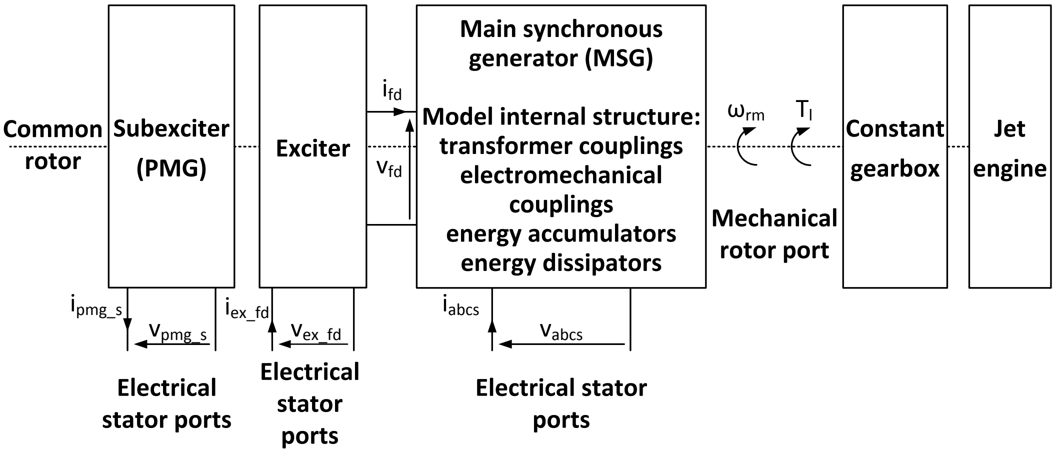

Figure 5.1 General structure of BSG model – for the generator performance the direction of positive power flows is assumed

Usually at the functional and behavioural level the BSG of is described as a synchronous generator (SG) with the assumption that the excitation current i_{fd} is the current of the MSG field winding [7]. In turn, the exciter is modelled using a simplified proportional functional model:

$$i_{fd} = k_{i\_ex} i_{ex\_fd} \tag{5.1}$$

where i_{ex_fd} is the excitation current of the exciter. The value of k_{i_ex} is calculated using the nominal excitation currents of the exciter and the MSG. The MSG nominal field current is calculated using the field winding cross section, and next verified using FEM simualtions.

5.3 GENERAL MODEL STRUCTURE OF MAIN GENERATOR

The model can be described in machine variables or in arbitrary reference frame. The model in machine variables is described using variables which represent actual connections of the MSG terminal box. It also describes the internal energy storage and dissipation in two damper windings (denoted by *kq* and *kd*). In Figure 5.2 a physical description of considered MSG is shown. In case of 3-phase machine a general voltage equation is formulated as following [7]:

$$\mathbf{v}_{abcs} = -\mathbf{r}_s\mathbf{i}_{abcs} + \frac{d\boldsymbol{\psi}_{abcs}}{dt} \tag{5.2}$$

$$\mathbf{v}_{qdr} = \mathbf{r}_r\mathbf{i}_{qdr} + \frac{d\boldsymbol{\psi}_{qdr}}{dt} \tag{5.3}$$

where $\mathbf{v}_{abcs}$ and $\mathbf{i}_{abcs}$ are respectively the stator 3-phase voltage and current vector ($\boldsymbol{f}_{abcs}{}^T = [f_{as} \quad f_{bs} \quad f_{cs}]$), $\mathbf{v}_{qdr}$ and $\mathbf{i}_{qdr}$ are respectively rotor voltage and current vector ($\boldsymbol{f}_{qdr}{}^T = [f_{kq} \quad f_{fd} \quad f_{kd}]$) in orthogonal direct and quadrature axis, $\mathbf{r}_s$ and $\mathbf{r}_r$ are the diagonal matrices of the stator and rotor winding resistances.

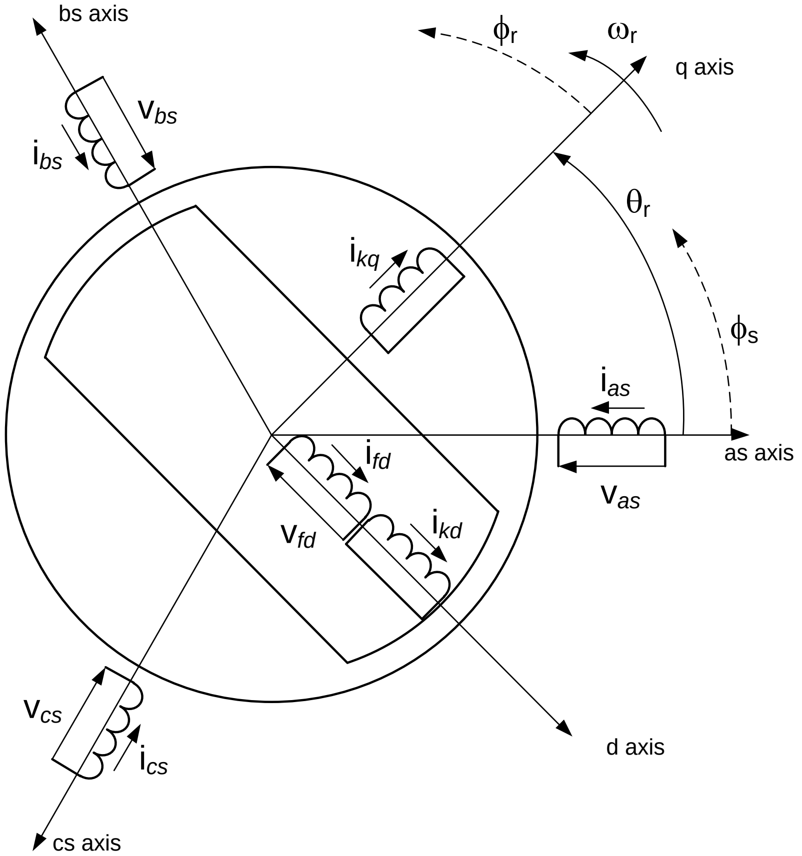

Figure 5.2 Physical description of two-pole salient-pole main synchronous generator with hybrid reference frames: axes *as*, *bs* and *cs* fixed in stator; axes *q* and *d* fixed in rotor [7]

The stator windings denoted by *as*, *bs and cs* are symmetrical and placed at the magnetic axes *as*, *bs* and *cs,* displaced by 120 degrees (electrical), respectively. The rotor electrical components are: the field winding denoted by *fd*, and two damper windings denoted by *kq* and *kd* placed at magnetic axes *d* and *q* are at right angle, respectively.

The flux linkage vectors $\boldsymbol{\psi}_{abcs}$ and $\boldsymbol{\psi}_{qdr}$ in the equations (5.2) and (5.3) are defined as follows [7]:

$$\begin{bmatrix} \boldsymbol{\psi}_{abcs} \\ \boldsymbol{\psi}_{qdr} \end{bmatrix} = \begin{bmatrix} \mathbf{L}_s(\theta_r) & \mathbf{L}_{sr}(\theta_r) \\ \left(\mathbf{L}_{sr}(\theta_r)\right)^{\mathrm{T}} & \mathbf{L}_r \end{bmatrix} \begin{bmatrix} -\mathbf{i}_{abcs} \\ \mathbf{i}_{qdr} \end{bmatrix} \tag{5.4}$$

In equations (5.4) the matrices denote: $\mathbf{L}_{\mathrm{s}}(\theta_{\mathrm{r}})$ is the stator windings self and mutual inductance matix:

$$\mathbf{L}_s(\theta_r) = \begin{bmatrix} L_{asas}(\theta_r) & L_{asbs}(\theta_r) & L_{ascs}(\theta_r) \\ L_{bsas}(\theta_r) & L_{bsbs}(\theta_r) & L_{bscs}(\theta_r) \\ L_{csas}(\theta_r) & L_{csbs}(\theta_r) & L_{cscs}(\theta_r) \end{bmatrix} \tag{5.5}$$

$\mathbf{L}_r$ is the rotor windings (field and damper cages) self and mutual inductance:

$$\mathbf{L}_r = \begin{bmatrix} L_{kqkq} & 0 & 0 \\ 0 & L_{fdfd} & L_{fdkd} \\ 0 & L_{kdfd} & L_{kdkd} \end{bmatrix} \tag{5.6}$$

$\mathbf{L}_{sr}(\theta_r)$ is the mutual inductance between stator and rotor windings:

$$\mathbf{L}_{sr}(\theta_r) = \begin{bmatrix} L_{askq}(\theta_r) & L_{asfd}(\theta_r) & L_{askd}(\theta_r) \\ L_{bskq}(\theta_r) & L_{bsfd}(\theta_r) & L_{bskd}(\theta_r) \\ L_{cskq}(\theta_r) & L_{csfd}(\theta_r) & L_{cskd}(\theta_r) \end{bmatrix} \tag{5.7}$$

Where θ_r is the electrical angular displacement of the rotor, the subscripts s, r, f and k denote stator, rotor, field and cage windings, respectively.

The electromagnetic torque in terms of the energy stored in the coupling field is defined as:

$$T_e = \left(\frac{P}{2}\right) \frac{\partial W_c\left(\mathbf{i}_{abcs}, \mathbf{i}_{qdr}, \mathbf{L}_s(\theta_r), \mathbf{L}_{sr}(\theta_r), \mathbf{L}_r\right)}{\partial \theta_r} \tag{5.8}$$

where $W_c\big(\mathbf{i}_{abcs}, \mathbf{i}_{qdr}, \mathbf{L}_s(\theta_r), \mathbf{L}_{sr}(\theta_r), \mathbf{L}_r\big)$ is magnetic coenergy is defined based on [17] as:

$$\begin{aligned}
&W_c\big(\mathbf{i}_{abcs}, \mathbf{i}_{qdr}, \mathbf{L}_s(\theta_r), \mathbf{L}_{sr}(\theta_r), \mathbf{L}_r\big)\\
&\quad= \int_0^{i_{as}} \big(i_{as}L_{asas}(\theta_r)\big)di_{as} + \int_0^{i_{bs}} \big(i_{as}L_{bsas}(\theta_r) + i_{bs}L_{bsbs}(\theta_r)\big)di_{bs}\\
&\quad+ \int_0^{i_{cs}} \big(i_{as}L_{csas}(\theta_r) + i_{bs}L_{csbs}(\theta_r) + i_{cs}L_{cscs}(\theta_r)\big)di_{cs}\\
&\quad+ \int_0^{i_{kq}} \big(i_{as}L_{askq}(\theta_r) + i_{bs}L_{bskq}(\theta_r) + i_{cs}L_{cskq}(\theta_r) + i_{kq}L_{kqkq}\big)di_{kq}\\
&\quad+ \int_0^{i_{fd}} \big(i_{as}L_{asfd}(\theta_r) + i_{bs}L_{bsfd}(\theta_r) + i_{cs}L_{csfd}(\theta_r) + i_{fd}L_{fdfd}\big)di_{fd}\\
&\quad+ \int_0^{i_{kd}} \big(i_{as}L_{askd}(\theta_r) + i_{bs}L_{bskd}(\theta_r) + i_{cs}L_{cskd}(\theta_r) + i_{fd}L_{fdkd}\\
&\quad+ i_{kd}L_{kdkd}\big)di_{kd}
\end{aligned} \tag{5.9}$$

For the torque calculation the energy stored in magnetic components is calculated/approximated assuming linearity of magnetic core:

$$\begin{aligned}
&W_c\big(\mathbf{i}_{abcs}, \mathbf{i}_{qdr}, \mathbf{L}_s(\theta_r), \mathbf{L}_{sr}(\theta_r), \mathbf{L}_r\big)\\
&\quad= \frac{1}{2}L_{asas}(\theta_r)i_{as}^2 + L_{bsas}(\theta_r)i_{as}i_{bs} + \frac{1}{2}L_{bsbs}(\theta_r)i_{bs}^2\\
&\quad+ L_{csas}(\theta_r)i_{as}i_{cs} + L_{csbs}(\theta_r)i_{bs}i_{cs} + \frac{1}{2}L_{cscs}(\theta_r)i_{cs}^2\\
&\quad+ L_{asfd}(\theta_r)i_{as}i_{fd} + L_{bsfd}(\theta_r)i_{bs}i_{fd} + L_{csfd}(\theta_r)i_{cs}i_{fd} + \frac{1}{2}L_{fdfd}i_{fd}^2\\
&\quad+ L_{askd}(\theta_r)i_{as}i_{kd} + L_{bskd}(\theta_r)i_{bs}i_{kd} + L_{cskd}(\theta_r)i_{cs}i_{kd}\\
&\quad+ L_{fdkd}i_{fd}i_{kd} + \frac{1}{2}L_{kdkd}i_{kd}^2 + L_{askq}(\theta_r)i_{as}i_{kq} + L_{bskq}(\theta_r)i_{bs}i_{kq}\\
&\quad+ L_{cskq}(\theta_r)i_{cs}i_{kq} + \frac{1}{2}L_{kqkq}i_{kq}^2
\end{aligned} \tag{5.10}$$

and the derivative of (5.10) over the angle θ_r is calculated by introducing:

$$G_x(\theta_r) = \frac{dL_x(\theta_r)}{d\theta_r} \tag{5.11}$$

The G coefficient have units of henrys. It is usually referred as *rotational inductance* [9]. And the electromagnetic torque is calculated:

$$\begin{aligned}T_e = {} & \frac{1}{2}G_{asas}(\theta_r)i_{as}^2 + G_{bsas}(\theta_r)i_{as}i_{bs} + \frac{1}{2}G_{bsbs}(\theta_r)i_{bs}^2 \\ & + G_{csas}(\theta_r)i_{as}i_{cs} + G_{csbs}(\theta_r)i_{bs}i_{cs} + \frac{1}{2}G_{cscs}(\theta_r)i_{cs}^2 \\ & + G_{asfd}(\theta_r)i_{as}i_{fd} + G_{bsfd}(\theta_r)i_{bs}i_{fd} + G_{csfd}(\theta_r)i_{cs}i_{fd} \\ & + G_{askd}(\theta_r)i_{as}i_{kd} + G_{bskd}(\theta_r)i_{bs}i_{kd} + G_{cskd}(\theta_r)i_{cs}i_{kd} \\ & + G_{askq}(\theta_r)i_{as}i_{kq} + G_{bskq}(\theta_r)i_{bs}i_{kq} + G_{cskq}(\theta_r)i_{cs}i_{kq}\end{aligned} \tag{5.12}$$

The torque and rotor speed are related by (in generator performance):

$$T_e = -J\frac{d\omega_{rm}}{dt} - B_m\omega_{rm} + T_l \tag{5.13}$$

where J is the inertia expressed in $kg \times m^2$, B_m friction coefficient, ω_{rm} mechanical angular speed of the rotor, ω_r electrical angular speed of the rotor. Electrical and mechanical speeds are related by number of poles P:

$$\omega_r = \frac{d\theta_r}{dt} \tag{5.14}$$

$$\omega_r = \left(\frac{P}{2}\right)\omega_{rm} \tag{5.15}$$

The mechanical torque T_l is positive for a torque input to the shaft of the generator performance of the BSG.

It is worth mentioning that the model does not include the additional electromagnetic torque developed by the ac exciter and the sub exciter. This torque can be calculated as:

$$T_{add} = \frac{i_{fd}^2 \times r_{fd}}{\omega_{rm}\,\eta_{add}} \tag{5.16}$$

where r_{fd} is main generator stage field winding resistance and η_{add} is combined efficiency of the ac exciter and the subexciter.

5.4 FUNCTIONAL LEVEL MODEL OF THE MAIN GENERATOR

The functional model has been developed in arbitrary reference frame. In order to describe this model, the equations and parameters of the model in machine variables, presented in previous section are transformed into the arbitrary reference frame by applying the Clarke and Park transformation [7,59,60]:

$$\mathbf{K}_s = \frac{2}{3}\begin{bmatrix} \cos(\theta_r) & \cos\left(\theta_r - \frac{2\pi}{3}\right) & \cos\left(\theta_r + \frac{2\pi}{3}\right) \\ \sin(\theta_r) & \sin\left(\theta_r - \frac{2\pi}{3}\right) & \sin\left(\theta_r + \frac{2\pi}{3}\right) \\ \frac{1}{2} & \frac{1}{2} & \frac{1}{2} \end{bmatrix} \tag{5.17}$$

Using this transformations the voltage equations are written in *qd*0 arbitrary reference frame. Transformed voltage equations for the MSG model are defined as [7]:

$$\mathbf{v}_{qd0s} = -\mathbf{r}_s \mathbf{i}_{qd0s} + \omega_\mathrm{r} \boldsymbol{\psi}_{qds} + \frac{d\boldsymbol{\psi}_{qd0s}}{dt} \tag{5.18}$$

$$\mathbf{v}'^{r}_{qdr} = \mathbf{r}'_\mathrm{r} \mathbf{i}'^{r}_{qdr} + \frac{d\boldsymbol{\psi}'^{r}_{qdr}}{dt} \tag{5.19}$$

where

$$\left(\boldsymbol{\psi}_{qds}\right)^\mathrm{T} = [\psi_{ds} \quad -\psi_{qs} \quad 0] \tag{5.20}$$

The voltages are refer to the stator windings. The flux linkage equations are defined as [7]:

$$\begin{bmatrix} \boldsymbol{\psi}_{qd0s} \\ \boldsymbol{\psi}'^{r}_{qdr} \end{bmatrix} = \begin{bmatrix} \mathbf{K}_s \mathbf{L}_s(\theta_r)(\mathbf{K}_s)^{-1} & \mathbf{K}_s \mathbf{L}'_{sr}(\theta_r) \\ \frac{2}{3}\left(\mathbf{L}'_{sr}(\theta_r)\right)^\mathrm{T}(\mathbf{K}_s)^{-1} & \mathbf{L}'_r \end{bmatrix} \begin{bmatrix} -\mathbf{i}_{qd0s} \\ \mathbf{i}'^{r}_{qdr} \end{bmatrix} \tag{5.21}$$

where $\mathbf{L}_\mathrm{s}(\theta_\mathrm{r})$ is the stator windings self and mutual inductance and is defined as:

$$\mathbf{L}_s(\theta_r) = \begin{bmatrix} L_{ls} + L_A - L_B \cos 2(\theta_r) & -\frac{1}{2}L_A - L_B \cos 2\left(\theta_r - \frac{\pi}{3}\right) & -\frac{1}{2}L_A - L_B \cos 2\left(\theta_r + \frac{\pi}{3}\right) \\ -\frac{1}{2}L_A - L_B \cos 2\left(\theta_r - \frac{\pi}{3}\right) & L_{ls} + L_A - L_B \cos 2\left(\theta_r - \frac{2\pi}{3}\right) & -\frac{1}{2}L_A - L_B \cos 2(\theta_r + \pi) \\ -\frac{1}{2}L_A - L_B \cos 2\left(\theta_r + \frac{\pi}{3}\right) & -\frac{1}{2}L_A - L_B \cos 2(\theta_r + \pi) & L_{ls} + L_A - L_B \cos 2\left(\theta_r - \frac{2\pi}{3}\right) \end{bmatrix} \tag{5.22}$$

$\mathbf{L}'_r$ is the rotor windings (field and damper cages) self and mutual inductance and is defined as:

$$\mathbf{L}_r = \begin{bmatrix} L_{lkq} + L_{mq} & 0 & 0 \\ 0 & L_{lfd} + L_{md} & L_{md} \\ 0 & L_{md} & L_{lkd} + L_{md} \end{bmatrix} \tag{5.23}$$

$\mathbf{L}'_{sr}(\theta_r)$ is the mutual inductance between stator and rotor windings defined as:

$$\mathbf{L}'_{sr}(\theta_r) = \begin{bmatrix} L_{mq}\cos(\theta_r) & L_{md}\sin(\theta_r) & L_{md}\sin(\theta_r) \\ L_{mq}\cos\left(\theta_r - \frac{2\pi}{3}\right) & L_{md}\sin\left(\theta_r - \frac{2\pi}{3}\right) & L_{md}\sin\left(\theta_r - \frac{2\pi}{3}\right) \\ L_{mq}\cos\left(\theta_r + \frac{2\pi}{3}\right) & L_{md}\sin\left(\theta_r + \frac{2\pi}{3}\right) & L_{md}\sin\left(\theta_r + \frac{2\pi}{3}\right) \end{bmatrix} \tag{5.24}$$

where L_{md} and L_{mq} are magnetising inductances in direct and quadrature axis.

$$L_{md} = \frac{3}{2} \times \max_{0 \le \theta_r \le \frac{2\pi}{P}} L_{asas}(\theta_r) \tag{5.25}$$

$$L_{mq} = \frac{3}{2} \times \min_{0 \le \theta_r \le \frac{2\pi}{P}} L_{asas}(\theta_r) \tag{5.26}$$

If the machine has a cylindrical rotor (no saliency) the magnetising inductances are:

$$L_{md} = L_{mq} = \frac{3}{2} L_s \tag{5.27}$$

where L_s is the armature winding phase self-inductance independent from rotor position.

Functional model describes MSG in the qd0 arbitrary reference frame variables using transformation (5.17). The general structure of functional model is described as in (5.18) and (5.19). The mechanical rotor port of the model (figure 5.1) is described using (5.8), (5.13), (5.14) and can be written as:

$$T_e = \left(\frac{3}{2}\right)\left(\frac{P}{2}\right)\left(\psi_{ds} i_{qs} - \psi_{qs} i_{ds}\right) \tag{5.28}$$

The electrical rotor ports are from the model (5.19) – v_{fd} and i_{fd}. The electric stator ports are defined as:

$$v_s = \frac{\sqrt{v_{ds} + v_{qs}}}{\sqrt{2}} \tag{5.29}$$

$$i_s = \frac{\sqrt{i_{ds} + i_{qs}}}{\sqrt{2}} \tag{5.30}$$

The zero components (v_{0s} and i_{0s}) are neglected due to assumed symmetry and sinusoidal distribution of air-gap flux density. The v_s and i_s are RMS values of stator phase voltage and line current.

5.5 BEHAVIOURAL LEVEL MODEL OF MAIN GENERATOR

5.5.1 GENERAL MODEL STRUCTURE

For the behavioural model can be taken into account such physical phenomena as:

- space-poliharmonic air-gap flux density distribution,
- saturation of magnetic materials,
- hysteresis and eddy current loses,
- skin effect in conductive elements.

This model can describe the behaviour of the BSG in steady and transient states as well. In order to model the normal and fault performance of the BSG the saturation of magnetic core and space-philharmonic distribution of air-gap flux density have to be implemented in the developed model. These physical phenomena have been considered in the developed model because of the their significant influence on AEPS performance.

The general structure of the MSG model is presented in section 5.2. The modified winding function approach [35,49,74,76] is proposed for the calculation of the self and mutual inductances functions. These inductances are functions of rotor position. And are calculated form stator and rotor $MMFs$. The stator $MMFs$ are defined as:

$$MMF_{as}(\phi_s) = \frac{N_s'}{2} i_{as} \sum_{k=1}^{n} A'_{(2k-1)s} \cos\big((2k-1)\phi_s\big) \tag{5.31}$$

$$MMF_{bs}(\phi_s) = \frac{N_s'}{2} i_{bs} \sum_{k=1}^{n} A'_{(2k-1)s} \cos\left((2k-1)\left(\phi_s - \frac{2\pi}{3}\right)\right) \tag{5.32}$$

$$MMF_{cs}(\phi_s) = \frac{N_s'}{2} i_{cs} \sum_{k=1}^{n} A'_{(2k-1)s} \cos\left((2k-1)\left(\phi_s + \frac{2\pi}{3}\right)\right) \tag{5.33}$$

where ϕ_s is the angular displacement along the stator circumference, N_s' represents the number of turns of the equivalent sinusoidally distributed stator winding. Figure 5.3 shows the armature winding MMF (one phase) distribution in function of angular displacement along the stator circumference.

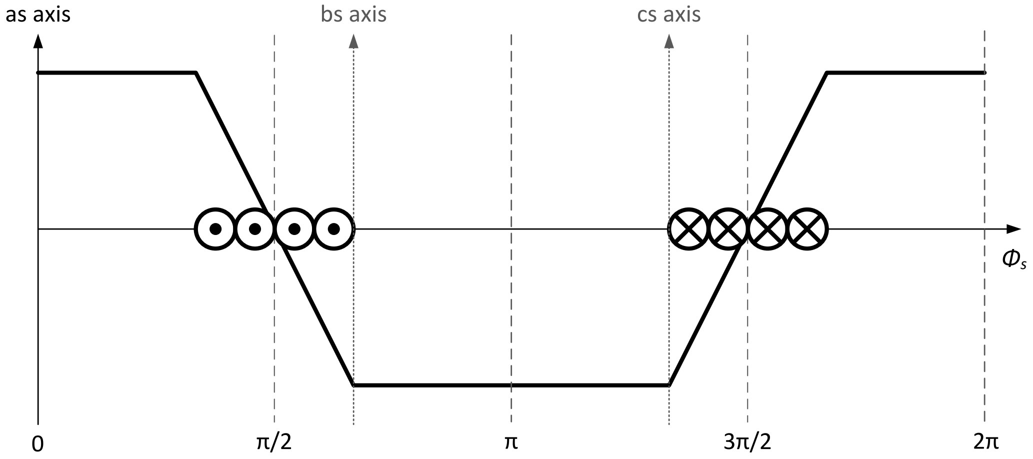

Figure 5.3 The armature winding MMF distribution in function of angular displacement along the stator circumference [7]

The relative values of the odd harmonics amplitudes of armature winding MMF are expressed as:

$$A'_{(2k-1)s} = A_{(2k-1)s}/A_{1s} \tag{5.34}$$

$A_{(2k-1)s}$ $(k \in \mathbb{Z}^+)$ are absolute values of the MMF odd harmonics. The absolute value of armature winding MMF fundamental component is defined as:

$$A_{1s} = \frac{N_s'}{2} \tag{5.35}$$

The $MMFs$ of rotor windings are defined as:

$$MMF_{fd}(\phi_r) = -\frac{N_{fd}'}{2} i_{fd} \sum_{k=1}^{n} A'_{(2k-1)fd} \sin\left((2k-1)\phi_r\right) \tag{5.36}$$

$$MMF_{kd}(\phi_r) = -\frac{N'_{kd}}{2} i_{kd} \sum_{k=1}^{n} A'_{(2k-1)kd} \sin\big((2k-1)\phi_r\big) \tag{5.37}$$

$$MMF_{kq}(\phi_r) = \frac{N'_{kq}}{2} i_{kq} \sum_{k=1}^{n} A'_{(2k-1)kq} \cos\big((2k-1)\phi_r\big) \tag{5.38}$$

where ϕ_r is the angular displacement along the rotor circumference, N'_{fd}, N'_{kd} and N'_{kq} represents the number of turns of the equivalent sinusoidally distributed field, direct axis damper and quadrature axis damper windings respectively. Figure 5.3 shows the rotor windings $MMFs$ distribution in function of angular displacement along the rotor circumference.

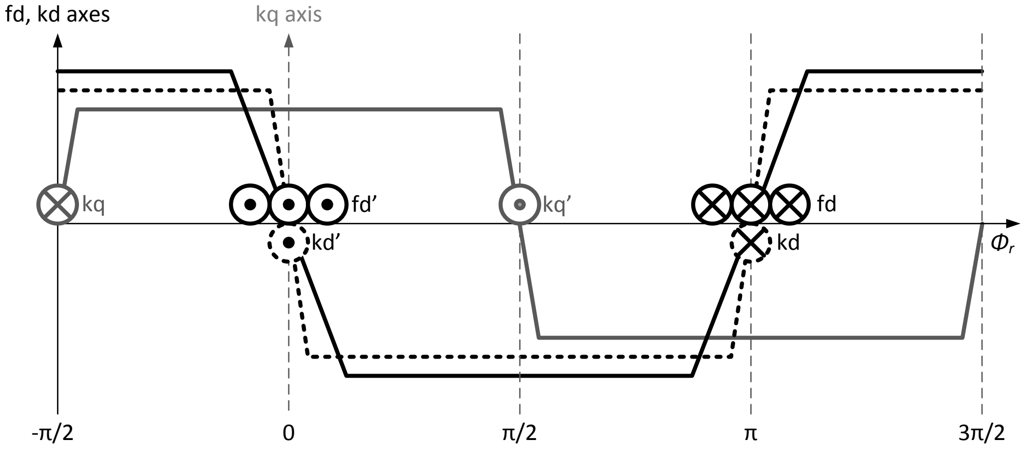

Figure 5.4 The rotor windings MMFs distribution in function of angular displacement along the rotor circumference [7]

The damper winding distributions are the equivalent circuits representing shorted damper cage bars in the poles of the machine rotor.

The relative values of the odd harmonics amplitudes of field, direct axis damper and quadrature axis damper windings $MMFs$ respectively expressed as:

$$A'_{(2k-1)fd} = A_{(2k-1)fd}/A_{1fd} \tag{5.39}$$

$$A'_{(2k-1)kd} = A_{(2k-1)kd}/A_{1kd} \tag{5.40}$$

$$A'_{(2k-1)kq} = A_{(2k-1)kq}/A_{1kq} \tag{5.41}$$

Amplitudes $A_{(2k-1)fd}$, $A_{(2k-1)kd}$ and $A_{(2k-1)kq}$ are absolute values of the $MMFs$ amplitudes of the odd harmonics of field, direct axis damper and quadrature axis damper windings). The absolute values of these windings $MMFs$ fundamental components are defined as:

$$A_{1fd} = \frac{N'_{fd}}{2} \tag{5.42}$$

$$A_{1kd} = \frac{N'_{kd}}{2} \tag{5.43}$$

$$A_{1kq} = \frac{N'_{kq}}{2} \tag{5.44}$$

The relation between stator and rotor angular displacements along the stator and rotor circumferences is defined using the angular displacement of the rotor:

$$\phi_s = \phi_r + \theta_r \tag{5.45}$$

Stator and rotor winding distribution is calculated from presented in equations (5.31), (5.32), (5.33), (5.36), (5.37) and (5.38) $MMFs$. For the stator windings:

$$N_{as}(\phi_s) = \frac{1}{i_{as}}\left(\frac{d}{d\phi_s} MMF_{as}(\phi_s, t)\right) \tag{5.46}$$

$$N_{bs}(\phi_s) = \frac{1}{i_{bs}}\left(\frac{d}{d\phi_s} MMF_{bs}(\phi_s, t)\right) \tag{5.47}$$

$$N_{cs}(\phi_s) = \frac{1}{i_{cs}}\left(\frac{d}{d\phi_s} MMF_{cs}(\phi_s, t)\right) \tag{5.48}$$

and the for the rotor windings:

$$N_{fd}(\phi_r) = \frac{1}{i_{fd}}\left(\frac{d}{d\phi_r} MMF_{fd}(\phi_r, t)\right) \tag{5.49}$$

$$N_{kd}(\phi_r) = \frac{1}{i_{kd}}\left(\frac{d}{d\phi_r} MMF_{kd}(\phi_r, t)\right) \tag{5.50}$$

$$N_{kq}(\phi_r) = \frac{1}{i_{kq}}\left(\frac{d}{d\phi_r} MMF_{kq}(\phi_r, t)\right) \tag{5.51}$$

Substituting equation (5.31) – (5.33) and (5.36) – (5.38) in (5.46) – (5.51), respectively, yields:

$$N_{as}(\phi_s) = -\frac{N_s'}{2}\sum_{k=1}^{n}(2k-1)A'_{(2k-1)s}\sin\big((2k-1)\phi_s\big) \tag{5.52}$$

$$N_{bs}(\phi_s) = -\frac{N_s'}{2}\sum_{k=1}^{n}(2k-1)A'_{(2k-1)s}\sin\left((2k-1)\left(\phi_s - \frac{2\pi}{3}\right)\right) \tag{5.53}$$

$$N_{cs}(\phi_s) = -\frac{N_s'}{2}\sum_{k=1}^{n}(2k-1)A'_{(2k-1)s}\sin\left((2k-1)\left(\phi_s + \frac{2\pi}{3}\right)\right) \tag{5.54}$$

$$N_{fd}(\phi_s) = -\frac{N_{fd}'}{2}\sum_{k=1}^{n}(2k-1)A'_{(2k-1)fd}\cos\big((2k-1)\phi_r\big) \tag{5.55}$$

$$N_{kd}(\phi_s) = -\frac{N_{kd}'}{2}\sum_{k=1}^{n}(2k-1)A'_{(2k-1)kd}\cos\big((2k-1)\phi_r\big) \tag{5.56}$$

$$N_{kq}(\phi_s) = -\frac{N_{kq}'}{2}\sum_{k=1}^{n}(2k-1)A'_{(2k-1)kq}\sin\big((2k-1)\phi_r\big) \tag{5.57}$$

The air-gap length variation is approximated as a periodic function of displacement about the airgap [7]:

$$\delta(\phi_s - \theta_r) = \frac{1}{\alpha_d}\frac{1}{\alpha_0' - \sum_{k=1}^{m}\alpha_k'\cos\big(2k(\phi_s - \theta_r)\big)} \tag{5.58}$$

where $1/\alpha_d$ is the absolute value (in meters) of the average airgap length along d axis and also denotes the minimum air-gap length as:

$$\frac{1}{\alpha_d} = \frac{1}{\alpha_0 + \sum_{k=1}^{m}\alpha_k} \tag{5.59}$$

and the relative values of α_k' ($k \in \langle 0, m\rangle$)are expressed as:

$$\alpha_k' = \frac{\alpha_k}{\alpha_d} \tag{5.60}$$

where m is the number of harmonics used to describe the distribution of the air-gap length – in developed model $m = 1$ for the salinet pole main generator stage and $m = 0$ for nonsalinet cylindrical main generator stage of BSG. Taking into account the above consideration, the following expressions for calculating the SG armature self and mutual inductances can be written as:

$$L_{xsxs}(\theta_r) = \mathrm{L}_{ls} + \frac{1}{i_{xs}} \int_{\pi}^{2\pi} \left[N_{xs}(\phi_s) \int_{\phi_s}^{\phi_s+\pi} \left[\mu_0 \frac{1}{\delta(\xi - \theta_r)} MMF_{xs}(\xi) rl \right] d\xi \right] d\phi_s \tag{5.61}$$

$$L_{xsys}(\theta_r) = \frac{1}{i_{ys}} \int_{\pi}^{2\pi} \left[N_{xs}(\phi_s) \int_{\phi_s}^{\phi_s+\pi} \left[\mu_0 \frac{1}{\delta(\xi - \theta_r)} MMF_{ys}(\xi) rl \right] d\xi \right] d\phi_s \tag{5.62}$$

where x and y denote a, b or c indexes (in (5.62) $x \neq y$). The field winding self inductance can be written as:

$$L_{fdfd} = \mathrm{L}_{lfd} + \frac{1}{i_{fd}} \int_{\pi/2}^{3\pi/2} \left[N_{fd}(\phi_r) \int_{\phi_r}^{\phi_r+\pi} \left[\mu_0 \frac{1}{\delta(\xi)} MMF_{fd}(\xi) rl \right] d\xi \right] d\phi_r \tag{5.63}$$

The direct axis damper winding self inductance can be written as:

$$L_{kdkd} = \mathrm{L}_{lkd} + \frac{1}{i_{kd}} \int_{\pi/2}^{3\pi/2} \left[N_{kd}(\phi_r) \int_{\phi_r}^{\phi_r+\pi} \left[\mu_0 \frac{1}{\delta(\xi)} MMF_{kd}(\xi) rl \right] d\xi \right] d\phi_r \tag{5.64}$$

The quadrature axis damper winding self inductance can be written as:

$$L_{kqkq} = \mathrm{L}_{lkq} + \frac{1}{i_{kq}} \int_{\pi}^{2\pi} \left[N_{kq}(\phi_r) \int_{\phi_r}^{\phi_r+\pi} \left[\mu_0 \frac{1}{\delta(\xi)} MMF_{kq}(\xi) rl \right] d\xi \right] d\phi_r \tag{5.65}$$

The mutual inductance between field and direct axis damper winding can be written as:

$$L_{fdkd} = \frac{1}{i_{kd}} \int_{\pi/2}^{3\pi/2} \left[N_{fd}(\phi_r) \int_{\phi_r}^{\phi_r+\pi} \left[\mu_0 \frac{1}{\delta(\xi)} MMF_{kd}(\xi) rl \right] d\xi \right] d\phi_r \tag{5.66}$$

$$L_{kdfd} = L_{fdkd} \tag{5.67}$$

The mutual inductances between stator windings and rotor windings can be written as:

$$L_{xsfd}(\theta_r) = \frac{1}{i_{fd}} \int_{\pi}^{2\pi} \left[N_{xs}(\phi_s) \int_{\phi_s}^{\phi_s+\pi} \left[\mu_0 \frac{1}{\delta(\xi - \theta_r)} MMF_{fd}(\xi) rl \right] d\xi \right] d\phi_s \tag{5.68}$$

$$L_{xskd}(\theta_r) = \frac{1}{i_{kd}} \int_{\pi}^{2\pi} \left[N_{xs}(\phi_s) \int_{\phi_s}^{\phi_s+\pi} \left[\mu_0 \frac{1}{\delta(\xi - \theta_r)} MMF_{kd}(\xi) rl \right] d\xi \right] d\phi_s \tag{5.69}$$

$$L_{xskq}(\theta_r) = \frac{1}{i_{kq}} \int_{\pi}^{2\pi} \left[N_{xs}(\phi_s) \int_{\phi_s}^{\phi_s+\pi} \left[\mu_0 \frac{1}{\delta(\xi - \theta_r)} MMF_{kq}(\xi) rl \right] d\xi \right] d\phi_s \tag{5.70}$$

where l is the axial length of the air-gap of the machine and r is the mean radius of the airgap, and ξ is dummy variable, the subscript l (in L_{lxx}) denote leakage inductance.

For further model development it is assumed that the first harmonic amplitudes of the mutual inductances between stator and rotor associated with the airgap field, may be expressed as:

$$L_{sf} = \left(\frac{N_s'}{2}\right)\left(\frac{N_{fd}'}{2}\right)\Lambda \tag{5.71}$$

$$L_{skd} = \left(\frac{N_s'}{2}\right)\left(\frac{N_{kd}'}{2}\right)\Lambda \tag{5.72}$$

$$L_{skq} = \left(\frac{N_s'}{2}\right)\left(\frac{N_{kq}'}{2}\right)\Lambda \tag{5.73}$$

where $\Lambda = rl\pi\mu_0\alpha_d$ is the magnetic permanence of the airgap. The average value of self armature winding inductance, can be expressed as:

$$L_s = \left(\frac{N_s'}{2}\right)^2 \Lambda \tag{5.74}$$

And the rotor self and mutual inductances can be expressed as:

$$L_f = \left(\frac{N_{fd}'}{2}\right)^2 \Lambda \tag{5.75}$$

$$L_{kd} = \left(\frac{N_{kd}'}{2}\right)^2 \Lambda \tag{5.76}$$

$$L_{kq} = \left(\frac{N'_{kq}}{2}\right)^2 \Lambda \tag{5.77}$$

$$L_{fkd} = \left(\frac{N'_{fd}}{2}\right)\left(\frac{N'_{kd}}{2}\right) \Lambda \tag{5.78}$$

The above described model can by simplified by applying adequate assumptions.

5.5.2 SPACE-POLIHARMONIC MODEL OF MAIN GENERATOR

Devices used in AEPS are often a source of higher time harmonics in voltages and currents. On the other, these devices can also be sensitive to higher time harmonics that are present in supplying voltage or current generated in AEPS. The importance of possible consequences in the aircraft AEPS it requires a proper analysis of those phenomena on the modelling stage of the system to be designed.

In order to study the AEPS, the BSG models taking into account the higher space harmonics of the air-gap flux density distribution have been developed. The BSG supply quite often nonlinear and non symmetrical loads and the influence of the one AEPS component such as the BSG on the entire system is significant. There is a necessity to investigate the influence of generated higher harmonics of voltage and current in BSGs on the performance of the AEPS.

The space-poliharmonic model of the main generator can be developed in machine variables or in arbitrary reference frame [27,46,47,71,72]. The advantage of models in machine variables is the possibility to include the asymmetry interactions of the internal elements of the machine.

The voltages and flux linkages are defined as in equations (5.2), (5.3) and (5.4). Applying the substitution of equations (5.71) – (5.78) the stator windings self and mutual inductance matrix (5.5) components after solving (5.61) – (5.70) can be written as:

$$L_{asas}(\theta_r) = L_{ls} + L_s \left(\begin{array}{c} \alpha'_0 \sum_{k=1}^{n} A'^2_{(2k-1)s} - \\ \left(\frac{1}{2} A'^2_{1s} + \sum_{k=1}^{n} A'_{(2\mathrm{k}-1)s} A'_{(2\mathrm{k}+2)s} \right) \alpha'_1 \cos(2\theta_r) \end{array} \right) \tag{5.79}$$

$$L_{asbs}(\theta_r) = -\tfrac{1}{2} L_s \left(\begin{array}{c} \left(A'^2_{1s} + \sum_{k=0}^{n} \left(-2A'^2_{(6\mathrm{k}+3)s} + A'^2_{(6\mathrm{k}+5)s} + A'^2_{(6\mathrm{k}+7)s} \right) \right) \alpha'_0 - \\ \left(A'^2_{1s} + \sum_{k=0}^{n} \left(\begin{array}{c} -A'_{(6\mathrm{k}+1)s} A'_{(6\mathrm{k}+3)s} - \\ A'_{(6\mathrm{k}+3)s} A'_{(6\mathrm{k}+5)s} + \\ 2A'_{(6\mathrm{k}+5)s} A'_{(6\mathrm{k}+7)s} \end{array} \right) \right) \alpha'_1 \cos\left(2 \left(\theta_r - \frac{\pi}{3} \right) \right) \end{array} \right) \tag{5.80}$$

$$L_{ascs}(\theta_r) = -\tfrac{1}{2} L_s \left(\begin{array}{c} \left(A'^2_{1s} + \sum_{k=0}^{n} \left(-2A'^2_{(6\mathrm{k}+3)s} + A'^2_{(6\mathrm{k}+5)s} + A'^2_{(6\mathrm{k}+7)s} \right) \right) \alpha'_0 + \\ \left(A'_{1s} + \sum_{k=0}^{n} \left(\begin{array}{c} -A'_{(6\mathrm{k}+1)s} A'_{(6\mathrm{k}+3)s} - \\ A'_{(6\mathrm{k}+3)s} A'_{(6\mathrm{k}+5)s} + \\ 2A'_{(6\mathrm{k}+5)s} A'_{(6\mathrm{k}+7)s} \end{array} \right) \right) \alpha'_1 \cos\left(2 \left(\theta_r + \frac{\pi}{3} \right) \right) \end{array} \right) \tag{5.81}$$

$$L_{bscs}(\theta_r) = -\tfrac{1}{2} L_s \left(\begin{array}{c} \left(A'^2_{1s} + \sum_{k=0}^{n} \left(-2A'^2_{(6\mathrm{k}+3)s} + A'^2_{(6\mathrm{k}+5)s} + A'^2_{(6\mathrm{k}+7)s} \right) \right) \alpha'_0 + \\ \left(A'_{1s} + \sum_{k=0}^{n} \left(\begin{array}{c} -A'_{(6\mathrm{k}+1)s} A'_{(6\mathrm{k}+3)s} - \\ A'_{(6\mathrm{k}+3)s} A'_{(6\mathrm{k}+5)s} + \\ 2A'_{(6\mathrm{k}+5)s} A'_{(6\mathrm{k}+7)s} \end{array} \right) \right) \alpha'_1 \cos\left(2 (\theta_r + \pi) \right) \end{array} \right) \tag{5.82}$$

In turn, the rotor self and mutual inductance matrix (5.6) components can be written as:

$$L_{fdfd} = L_{lfd} + L_f \left(\alpha'_0 \sum_{k=1}^{n} A'^2_{(2k-1)fd} + \alpha'_1 \left(\frac{1}{2} A'^2_{1fd} - \sum_{k=1}^{n} A'_{(2\mathrm{k}-1)fd} A'_{(2\mathrm{k}+2)fd} \right) \right) \tag{5.83}$$

$$L_{kdkd} = L_{lkd} + L_{kd} \left(\alpha'_0 \sum_{k=1}^{n} A'^2_{(2\mathrm{k}-1)kd} + \alpha'_1 \left(\frac{1}{2} A'^2_{1kd} - \sum_{k=1}^{n} A'_{(2\mathrm{k}-1)kd} A'_{(2\mathrm{k}+2)kd} \right) \right) \tag{5.84}$$

$$L_{kqkq} = L_{lkq} + L_{kq} \left(\alpha'_0 \sum_{k=1}^{n} A'^2_{(2k-1)kq} - \alpha'_1 \left(\frac{1}{2} A'^2_{1kq} + \sum_{k=1}^{n} A'_{(2\mathrm{k}-1)kq} A'_{(2\mathrm{k}+2)kq} \right) \right) \tag{5.85}$$

$$L_{fdkd} = L_{fkd} \begin{pmatrix} \alpha_0' \left(1 + \sum_{k=1}^{n} A'_{(2\mathrm{k}-1)fd} A'_{(2\mathrm{k}+1)kd} \right) \\ + \frac{\alpha_1'}{2} \left(1 - \sum_{k=1}^{n} A'_{(2\mathrm{k}-1)fd} A'_{(2\mathrm{k}+2)kd} - \sum_{k=1}^{n} A'_{(2\mathrm{k}+2)fd} A'_{(2\mathrm{k}-1)kd} \right) \end{pmatrix} \tag{5.86}$$

Finally, the mutual inductances between stator and rotor matrix (5.7) components can be written as:

$$L_{asfd}(\theta_r) = L_{sf} \begin{pmatrix} A'_{3s} \left(\alpha_0' A'_{1fd} + \frac{\alpha_1'}{2} \left(A'_{1fd} - A'_{3fd} \right) \right) \sin(\theta_r) + \\ \sum_{k=1}^{n} A'_{(2\mathrm{k}+2)s} \begin{pmatrix} \alpha_0' A'_{(2\mathrm{k}+2)fd} - \\ \frac{\alpha_1'}{2} A'_{(2\mathrm{k}-1)fd} - \\ \frac{\alpha_1'}{2} A'_{(2\mathrm{k}+5)fd} \end{pmatrix} \sin\left((2\mathrm{k}+2)(\theta_r) \right) \end{pmatrix} \tag{5.87}$$

$$L_{askd}(\theta_r) = L_{skd} \begin{pmatrix} A'_{3s} \left(\alpha_0' A'_{1kd} + \frac{\alpha_1'}{2} \left(A'_{1kd} - A'_{3kd} \right) \right) \sin(\theta_r) + \\ \sum_{k=1}^{n} A'_{(2\mathrm{k}+2)s} \begin{pmatrix} \alpha_0' A'_{(2\mathrm{k}+2)kd} - \\ \frac{\alpha_1'}{2} A'_{(2\mathrm{k}-1)kd} - \\ \frac{\alpha_1'}{2} A'_{(2\mathrm{k}+5)kd} \end{pmatrix} \sin\left((2\mathrm{k}+2)(\theta_r) \right) \end{pmatrix} \tag{5.88}$$

$$L_{askq}(\theta_r) = L_{skq} \begin{pmatrix} A'_{3s} \left(\alpha_0' A'_{1kd} - \frac{\alpha_1'}{2} \left(A'_{1kd} + A'_{3kd} \right) \right) \cos(\theta_r) + \\ \sum_{k=1}^{n} A'_{(2\mathrm{k}+2)s} \begin{pmatrix} \alpha_0' A'_{(2\mathrm{k}+2)kd} + \\ \frac{\alpha_1'}{2} A'_{(2\mathrm{k}-1)kd} + \\ \frac{\alpha_1'}{2} A'_{(2\mathrm{k}+5)kd} \end{pmatrix} \cos\left((2\mathrm{k}+2)(\theta_r) \right) \end{pmatrix} \tag{5.89}$$

For other phases (b, c) the angle between rotor and stator θ_r is shifted by $\frac{2\pi}{3}$ and $\frac{4\pi}{3}$, respectively. It should be noticed that according to equations (5.87), (5.88) and (5.89), in order to observe the harmonics presented in machine EMF, these harmonics have to be considered in armature winding distribution.

5.5.3 MAGNETIC SATURATION OF MAIN GENERATOR CORE

The magnetic saturation of the iron core of the main generator is modelled using the fallowing assumptions:

- entire machine core has the same level of saturation for given magnetising current;
- saturation affects the quadrature and direct axis at different level for given magnetising current [25,28,32,38,40,51,52,53,63,75] in salient-pole machine;
- all harmonics of the air-gap flux density distribution are influenced by the same saturation level.

Calculation of magnetic saturation is based on the evaluation of the induced voltage (EMF) saturation curve for the open armature circuit. This saturation is modelled using variable stator and rotor self and mutual inductances, defined as the functions of rotor angle and the total magnetisation current defined as:

$$i_m = \sqrt{i_{md}^2 + i_{mq}^2 + i_{0s}^2} \tag{5.90}$$

where:

$$i_{md} = i_{fd} + \frac{i_{ds}}{k_{sfd}} + \frac{i_{kd}}{k_{kfd}} \tag{5.91}$$

$$i_{mq} = \frac{i_{qs}}{k_{sfd}} + \frac{i_{kq}}{k_{kfd}} \tag{5.92}$$

the stator currents in arbitrary reference frame are:

$$[i_{qs} \quad i_{ds} \quad i_{0s}]^T = \mathbf{K}_s \, [i_{as} \quad i_{bs} \quad i_{cs}]^T \tag{5.93}$$

where, the magnetization current is referred to field winding. The k_{sfd} and k_{kfd} are coefficient that transform armature and *d* and *q* axes damper winding into field winding side, and are defined as:

$$k_{sfd} = \left(\frac{N_s'}{N_{fd}'}\right)\left(\frac{3}{2}\right) \tag{5.94}$$

$$k_{kfd} = \left(\frac{N'_{kd}}{N'_{fd}}\right) \tag{5.95}$$

Induced EMF at no load conditions can be calculated as:

$$e_{0xs} = -\frac{d\psi_{xs}}{dt} = -\left(i_{fd}\right)\frac{dL_{xsfd}(\theta_r)}{d\theta_r}\omega_r \tag{5.96}$$

Where x denotes a, b or c. The self and mutual inductances (5.71) – (5.78) can be defined as functions of magnetization current (5.90):

$$L_{s\_sat}(i_m) = k_{sat}(i_m)L_s \tag{5.97}$$

$$L_{sf\_sat}(i_m) = k_{sat}(i_m)L_{sf} \tag{5.98}$$

$$L_{f\_sat}(i_m) = k_{sat}(i_m)L_f \tag{5.99}$$

$$L_{skd\_sat}(i_m) = k_{sat}(i_m)L_{skd} \tag{5.100}$$

$$L_{kd\_sat}(i_m) = k_{sat}(i_m)L_{kd} \tag{5.101}$$

$$L_{skq\_sat}(i_m) = k_{sat}(i_m)L_{skq} \tag{5.102}$$

$$L_{kq\_sat}(i_m) = k_{sat}(i_m)L_{kq} \tag{5.103}$$

$$L_{fkd\_sat}(i_m) = k_{sat}(i_m)L_{fkd} \tag{5.104}$$

The flux linkages are defined as in (5.4) and because of the remanence voltage the $\mathbf{i}_{qdr}$ is defined as:

$$\mathbf{i}_{qdr}^{\mathrm{T}} = [i_{kq} \quad i_{fd} + i_{rem} \quad i_{kd}] \tag{5.105}$$

where i_{rem} is defined and calculated as constant value current which generates the remanence voltage. Using equation (5.96) and assuming the constant value current i_{rem} the remanence voltage amplitude is:

$$E_{0\_rem} = L_{sf} i_{rem} \omega_r \tag{5.106}$$

Saturation coefficient is obtained using no-load voltage characteristic defined as open circuit terminal voltage (v_{q0}) versus field current (i_{fd}) and remanence flux.

$$k_{sat}\left(i_{fd}\right) = \frac{L_{sf\_sat}\left(i_{fd}\right)}{L_{sf}} \tag{5.107}$$

where

$$L_{sf\_sat}\left(i_{fd}\right) = \frac{E_0 - E_{0\_rem}}{\omega_{\mathrm{r}} i_{fd}} \tag{5.108}$$

For the salient-pole main generator (commercial GT40PCz8 generator) the saturation coefficient is not equal in direct and quadrature axis [18,29,39,40,43,70,79]. The value of k_{sat} in quadrature axis is assumed to be equal 1 (no saturation) so the saturation coefficient can be expressed as:

$$k_{sat}(i_m, \phi_{im}) = \frac{L_{sf_{sat}}(i_m)}{L_{sf}} - \frac{\left(\frac{L_{sf_{sat}}(i_m)}{L_{sf}} - 1\right)}{2}(1 + \cos(2\,\phi_{im})) \tag{5.109}$$

where i_m is the amplitude and ϕ_{im} is the argument referred to rotor *qd*0 frame of magnetising current vector. It is assumed that in salient-pole generator saturation of the magnetic core is represented by k_{sat}. The self and mutual inductances depend upon the level of the magnetising current vector and its position in the arbitrary rotor reference frame *qd*0. The transition between direct and quadrature axis of magnetising current in saturation distribution is modelled using the trigonometric function (5.109).

Figure 5.5 shows the saturation coefficient k_{sat} as a function (5.109) of the angle of the magnetising current i_m referred to the rotor reference frame.

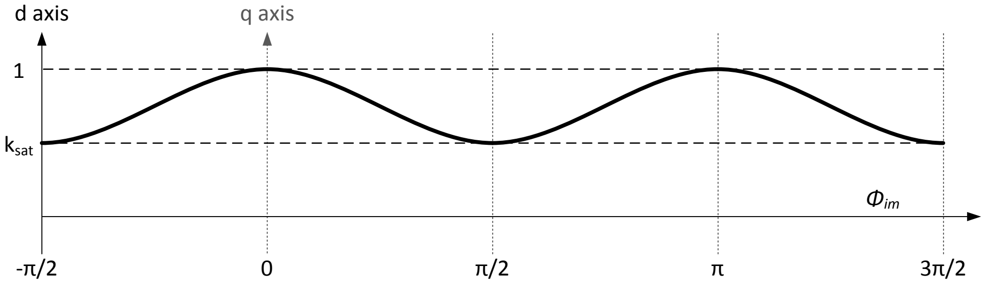

Figure 5.5 Saturation coefficient value as a function of magnetising current angel in rotor reference frame

5.6 SUMMARY

The development and generalization of the multiport dynamic network models for BSG has been presented. The models are derived for the two basic structures: the smooth air gap structure, and the salient-pole structure. Having in mind the applications of these models (refer to section 2.5), the considerations have focused on development of the following models of the BSG:

- functional level model;
- behavioural level model.

The functional level model is developed using space-monoharmonic model of synchronous machine, i.e., sinusoidal air-gap flux density distribution is assumed. The model port variables are described in arbitrary reference frame *qd*0. The Lumped parameters of this model are assumed constant. The model is devoted to represent simple performance states of the BSG in the AEPS.

The behavioural level model is described in machine variables. It represents the real electrical and mechanical port variables of the BSG. For this model the physical phenomena such as space-poliharmonic (nonsinusoidal) air-gap flux density distribution and magnetic material saturation have been taken into account.

The main advantage of developed behavioural level model of the considered BSG, apart from the one mention above, is a low computing power required for

BSG simulations. For this reason the winding function approach has been selected for development of this model.

The concern in the next chapter is with implementation of the developed BSG models in the Synopsys/Saber simulator for studies of AEPS.

6 IMPLEMENTATION OF THE DEVELOPED BEHAVIOURAL MODEL OF BSG IN SYNOPSYS/SABER SIMULATOR

6.1 INTRODUCTION

One essential requirement for a simulation environment of AEPS consisting of many nonlinear components is high computing efficiency. A key technique for achieving this goal is using an advanced network solver such as Synopsys/Saber and the modelling language MAST [16,114].

The Synopsys/Saber simulation environment – originally developed by Analogy, Inc., now owned by Synopsys [114] – is based on a mixed-signal hardware description language called MAST [16]. While using the modelling language MAST you are not only able to develop the various mathematical-based models you need, but you are also able to develop mixed-signal and multi-physical (mixed-technology) models. No more restrictive force-fitting of mechanical effects into the electrical domain is required, but total freedom to use the actual, physical mathematics that describe the desired behaviour – no matter the technology. Moreover, MAST models can be made at any level of abstraction – from simple transfer function descriptions, to detailed physics-based descriptions. They can also be mixed throughout multiple levels of hierarchy.

The MSG model implemented in Synopsys/Saber simulator take into account the 1’st (fundamental), 3’rd and 5’th space harmonic of stator and rotor windings MMFs. Also the average value and fundamental harmonic component of air-gap length distribution function are included in the model of salient-pole commercial generator GT40PCz8. The saturation of magnetic core is implemented in the simulator as described in the previous chapter.

For the commercial GT40PCz8 BSG the 5’th time harmonic of the EMF waveform is the only higher harmonic, which value exceeds 1% of the fundamental component. In turn for the designed prototype BSG the higher time harmonics of the

EMF waveform are small, and do not exceed the value of 1% of the fundamental component.

In this chapter the background for using the MAST language to model a BSG for studying the multi-physical behaviour of AEPS is discussed. Also some of the lumped (circuit) parameters for the implemented BSG model are calculated. Other lumped (circuit) parameters are evaluated using measurements results of the considered BSGs.

6.2 BSG MODEL DEVELOPMENT USING MAST LANGUAGE

The library of the Synopsys/Saber simulator contains a synchronous generator (SG) model in terms of qd0 variables. However, the insight into the core part of the model, i.e., the equation formulation, is protected fror the user. Because of that it is not possible to verify the library SG model, and also to make any modifications. Thus, for a specific studies of a AEPS it is necessary to develop SG model.

A behavioural model in MAST is considered to be a model whose behaviour is described using the features of the language itself – not by simply connecting pre-existing models together. A behavioural model may also include existing models, however not to the exclusion of having language-based functionality directly incorporated into the model description. The basic unit of system description in MAST is the template. Templates are synonymous to models. Templates may contain netlists, formulae, algorithms, or any combination of these.

The entire code of developed models as long as basic structure of model in MAST language is presented in appendix D. In this section we will only focus on the main features of MSG models such as implementation of nonlinearity and space-poliharmonic air-gap flux density.

In the MAST model the Table Look-Up Tool (TLU) foreign routine is used to define saturation characteristic. Fallowing assumptions are made for this approximation:

- linear interpolation is used

- linear extrapolation at low and high ends of no load characteristic is used

Data file containing points of no load EMF characteristic is constructed as follows:

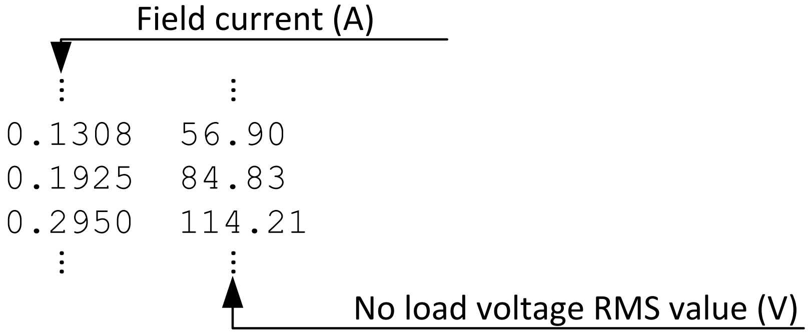

```
   ⋮       ⋮
0.1308  56.90
0.1925  84.83
0.2950  114.21
   ⋮       ⋮
```

Figure 6.1 View of file containing saturation data.

In the parameter section data pre-processing is made

```
# TLU data pre-processing (performs data checking, sorting and grid filling.)

  datap=tlu(0,1,sat_file,"",sat_interp,sat_extrap)
# TLU returns the sample points array for the independent variable

  sp1=tlu(1,addr(datap),1,sat_density) Sample Point Array
```

In the Values section TLU function is called to return the output value of the function for the given input values

```
#------TLU Function Evaluation
vsat=tlu(2,addr(datap),im)
v_rem=tlu(2,addr(datap),0)
```

Using (5.106), (5.107) and (5.108):

```
Lmsat=sqrt(2)*(vsat-v_rem)/((im*k_iex*sat_rpm*math_pi*p/30)+1e-6)    # saturation inductance

ifrem=sqrt(2)*v_rem/((sat_rpm*math_pi*p/30)*Lsfd+1e-6) # remanence flux

Ksat=Lmsat/Lsfd    # saturation coefficient
```

And for the salient pole main generator stage the saturation coefficient (5.109) is:

```
Ksat=Lmsat/Lsfd-(Lmsat/Lsfd-1)/2*(1+cos(2*asin((imd+1e-7)/(im+1e-7)))) # sat. coefficient
```

Inductances implemented in the template include saturation coefficient (Ksat) and first (fundamental), 3'rd and 5'th space harmonic od stator and rotor winding MMFs. The $L_{asas}(\theta_r)$ inductance in MAST template is defined as:

```
L_as_as = Lls + Ksat*Ls*(a1h*(1 + As3**2 + As5**2) –
0.5*a2h*(1 + 2*As3*(1 + As5))*cos(2*alpha*p))
```

And the flux linkage is written as:

```
phias = -1.0*ias*L_as_as - ibs*L_as_bs - ics*L_as_cs + ikq*L_as_kq +
 (ifd + ifrem)*L_as_fd + ikd*L_as_kd
```

The equation section contains machine electrical and mechanical equations and the equation to calculate total magnetising current:

```
# equation for calculation magnetising current
        iqs=2/3*(ias*cos(p*alpha)+ibs*cos(p*alpha-ang)+ics*cos(p*alpha+ang))
        ids=2/3*(ias*sin(p*alpha)+ibs*sin(p*alpha-ang)+ics*sin(p*alpha+ang))
        i0s=1/3*(ias+ibs+ics)
        md = -ids/kfd + ifd + ikd/kkd
        imq = -iqs/kfd + ikq/kkq
# module of magnetising current
        im=sqrt(imd**2 + imq**2 + (-i0s/kfd)**2)/k_iex

        ifd = ifd_ex*k_iex
# voltage equations
        ias: vas = -Rs*ias + d_by_dt(phias)
        ibs: vbs = -Rs*ibs + d_by_dt(phibs)
        ics: vcs = -Rs*ics + d_by_dt(phics)
        ifd: vfd_ex = Rex*ifd_ex + d_by_dt(phifd)
        ikd:   0 = Rkd*ikd + d_by_dt(phikd)
        ikq:   0 = Rkq*ikq + d_by_dt(phikq)

# mechanical equation
        Te = Tl - visc - mom
        mom=d_by_dt(Jw*wm)
        alpha: wm=d_by_dt(alpha)
```

Presented above part of MAST model code includes nonlinearity and space poliharmonic character of arigap flux density distribution. The variables and parameters of the model are presented in table 6.1. Figure 6.2 shows model symbol in Synopsys/Saber simulator.

Table 6.1 Parameters and variables of the MSG model:

Parameter/Variable	Description
ifd	Main generator field current
ifd_ex	Exciter field current
ias, ibs, ics	Armature current
ifd, ikd, ikq	Rotor currents (field and damper in d and q axes)
vas, vbs, vcs	Armature phase voltages
vfd_ex	Exciter field voltage
Rs	Armature winding resistance
Rex	Exciter field winding resistance
Rkd, Rkq	Rotor damper winding resistances (d and q axes)
phi	Prefix denotes linkage fluxes
Te	Electromagnetic torque
Tl	Load torque
visc	Torque due to friction
mom	Inertia torque
Jw	Rotor inertia
wm	Mechanical rotation speed
alpha	Mechanical rotor angle

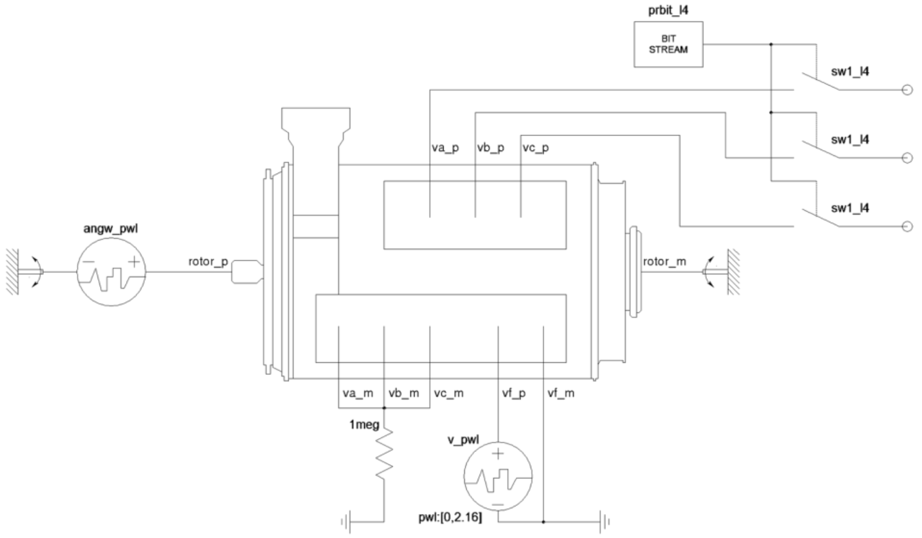

Figure 6.2 Synopsys/Saber BSG model simulation schematic

6.3 CIRCUIT PARAMETERS OF MODELS

Parameters for MSG models are determined using two ways:

- from calculations and verified by FEM simulations [1,8,13]
- from measurements results [55,56].

The distributions of self and mutual inductances are calculated using the BSG manufacture data sheet. The circuit parameters such as resistances and inductances (direct and quadrature axis values) are determined form measurements. Also from measurements (measured amplitudes of no load EMF waveform harmonics) the distribution of the air-gap length for salient-pole machine is calculated.

For the calculation of armature winding $MMF_a(\alpha)$ the skewing of the armature core slots is taking into account:

$$MMF_a(\phi_s) = \sum_{k=0}^{n} \frac{1}{n} MMF_{a1}\left(\phi_s - \frac{k}{n-1}\beta\right) \tag{6.1}$$

where $MMF_{a1}(\phi_s)$ is the armature winding MMF of one sheet of stator core assembly and n is number of stator core sheets in assembly. Figure 6.3 shows the skewing of stator slots.

Figure 6.4 shows the armature winding MMF distribution along the air-gap. The $MMFs$ of two studied main generator rotor solutions, the salient one and non-salient one ware also calculated (figure 6.5 and figure 6.6). Furthermore it is assumed that all calculated $MMFs$ have apart from fundamental component only odd components. In figure 6.4, figure 6.5 and figure 6.6 figure 6.6 amplitudes of the calculated $MMFs$ are presented. The negative value of a harmonic means that it is shifted by 180 degrees from the fundamental component.

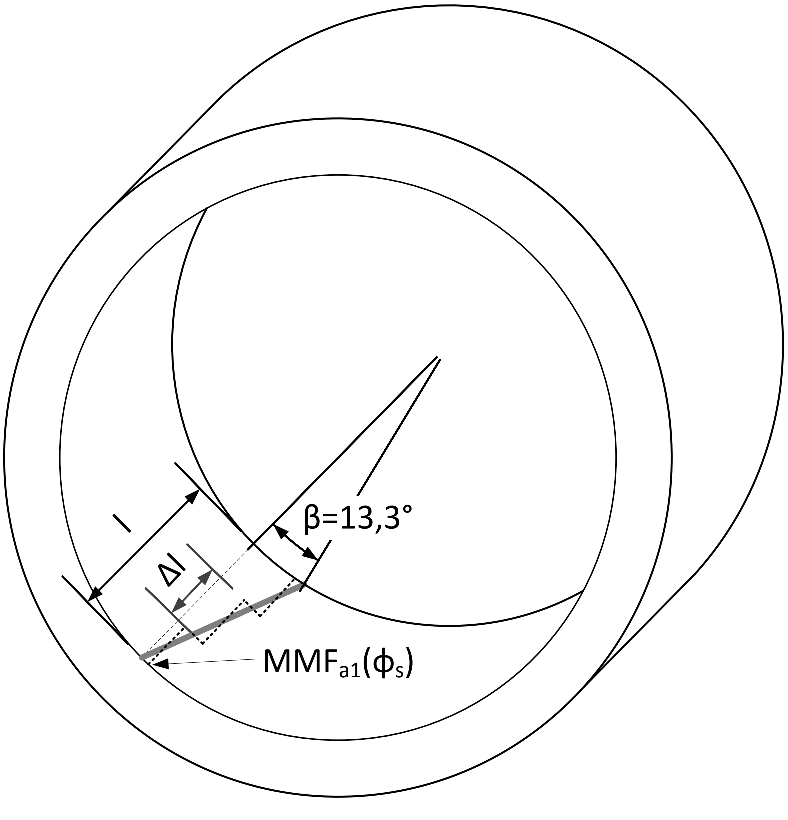

Figure 6.3 Skew of stator slot

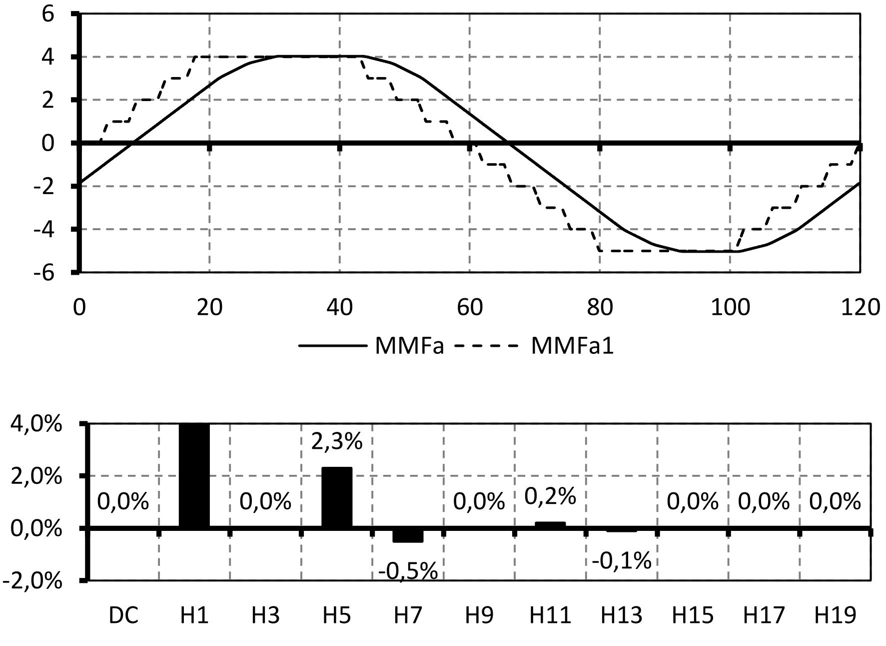

Figure 6.4 Armature winding (1/3 of machine) $MMF_a(\phi_s)$, assuming $I_s = 1A$. Amplitudes of $MMF_a(\phi_s)$ harmonics: $A_{1s} = 4.7A(100\%)$

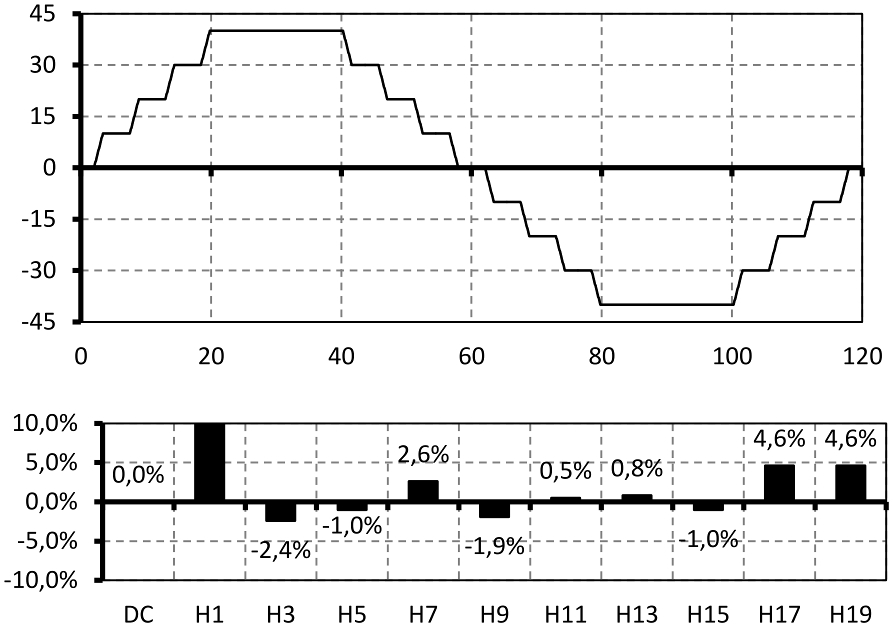

Figure 6.5 Designed prototype non-salient pole main generator field winding (1/3 of machine) $MMF_{fd}(\phi_r)$, assuming $I_{fd} = 1A$. Amplitudes of $MMF_{fd}(\phi_r)$ harmonics: $A_{1fd} = 41A(100\%)$

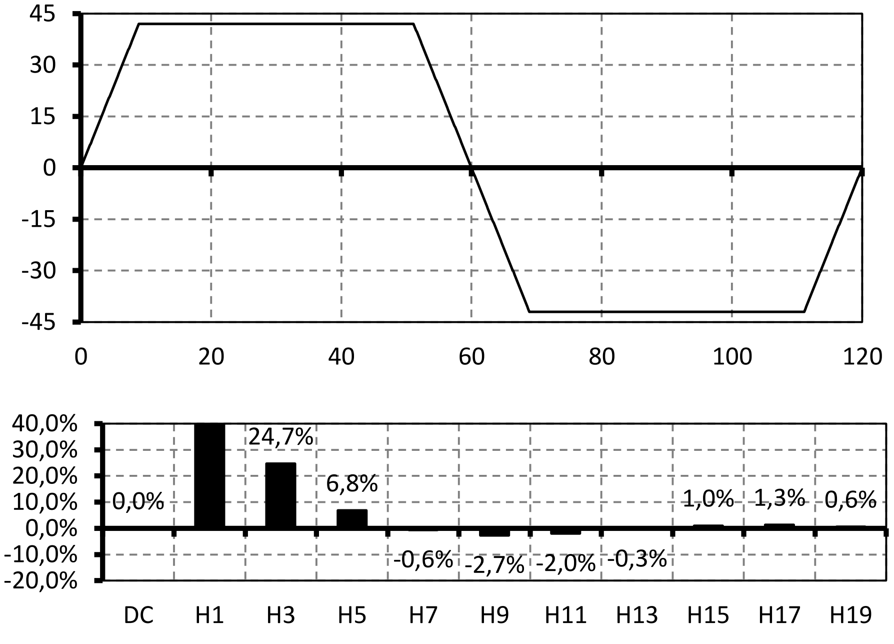

Figure 6.6 Commercial GT40PCz8 salient pole field winding (1/3 of machine) $MMF_{fd}(\phi_r)$, assuming $I_{fd} = 1A$. Amplitudes of $MMF_{fd}(\phi_r)$ harmonics: $A_{sp1fd} = 52A(100\%)$, where sp denotes salient-pole commercial BSG

To determine the coefficients α_0', α_1' (airgap length distribution) the BSG EMF (e_0) has been measured as a function of time and the harmonic analysis has been carried out (figure 6.7).

The instantaneous value of EMF e_{0as} can be expressed:

$$e_{0as} = \frac{d\psi_{as}}{dt} = \left(i_{fd}\right)\frac{dL_{asfd}(\theta_r)}{d\theta_r}\omega_r \tag{6.2}$$

knowing the mutual stator and rotor inductance $L_{asfd}(\theta_r)$ assuming only fundamental, 3'rd and 5'th harmonic are present:

$$\begin{aligned} &L_{asfd}(\theta_r) \\ &\quad = L_{sf}\left(\frac{1}{2}\left(2\alpha_0' + \alpha_1' - \alpha_1' A_{3fd}'\right)\sin(\theta_r)\right. \\ &\quad -\frac{1}{2}A_{3s}'\left(\alpha_1' - 2\alpha_0' A_{3fd}' + \alpha_1' A_{5fd}'\right)\sin(3\theta_r) \\ &\quad \left. + \frac{1}{2}A_{5s}'\left(-\alpha_1' A_{3fd}' + 2\alpha_0' A_{5fd}'\right)\sin(5\theta_r)\right) \end{aligned} \tag{6.3}$$

The following expressions for the amplitudes of fundamental E_{0an1h} and 5'th E_{0an5h} EMF harmonics (phase values for *as* winding), can be written respectively:

$$E_{0an1h} = L_{sf} i_{fd} 0.5\left(2\alpha_0' + \alpha_1' - \alpha_1' A_{3fd}'\right)\omega_r \tag{6.4}$$

$$E_{0an5h} = L_{sf} i_{fd} 2.5 A_{5s}'\left(-\alpha_1' A_{3fd}' + 2\alpha_0' A_{5fd}'\right)\omega_r \tag{6.5}$$

Using the equations (6.4) and (6.5) the values of the air-gap coefficients α_0' and α_1' for designed non salient pole main generator stage have been determined:

$$\alpha_0' = \frac{2.5 A_{5s}' A_{3fd}' E_{0as1h} + 0.5 E_{0as5h}\left(1 - A_{3fd}'\right)}{2.5\left(A_{3fd}' + A_{5fd}' - A_{3fd}' A_{5fd}'\right) A_{5s}' i_{fd} L_{sf}\omega_r} \tag{6.6}$$

$$\alpha_1' = \frac{5 A_{5s}' A_{5fd}' E_{0as1h} - E_{0as5h}}{2.5\left(A_{3fd}' + A_{5fd}' - A_{3fd}' A_{5fd}'\right) A_{5s}' i_{fd} L_{sf}\omega_r} \tag{6.7}$$

For commercial salient-pole GT40PCz8 BSG the A'_{xfd} value is replaced by A'_{spxfd} from figure 6.6.

Apart from the parameters of all windings $MMFs$ distributions of the no load EMF voltage of commercial salient pole GT40PCz8 BSG had to be studied in order to determine its harmonics: E_{0an1h} and E_{0an5h} needed for calculation of the air-gap length distribution parameters.

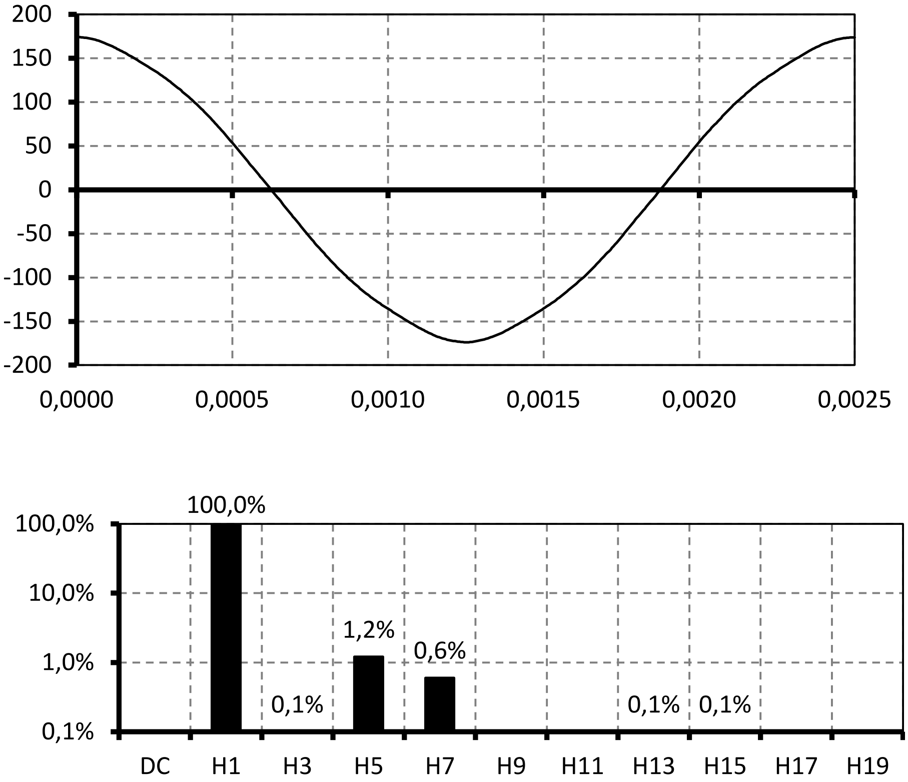

Figure 6.7 Commercial GT40PCz8 salient-pole BSG nominal no load phase voltage ($EMF_{as}(t)$) measurement.
Amplitudes of $EMF_{as}(t)$ harmonics: $E_{0an1h} = 171\ V\ (100\%)$

As can be observed in figure 6.7 the 5'th harmonic is only harmonic which exceeds 1% of the fundamental component and was used for calculation of α'_0 and α'_1.

Figure 6.8 shows the EMF and its harmonics for the prototype non-salient pole BSG. As can be observed the higher harmonics (3'rd and higher) are negligible.

For the analysis of designed prototype BSG a space monoharmonic model is sufficient.

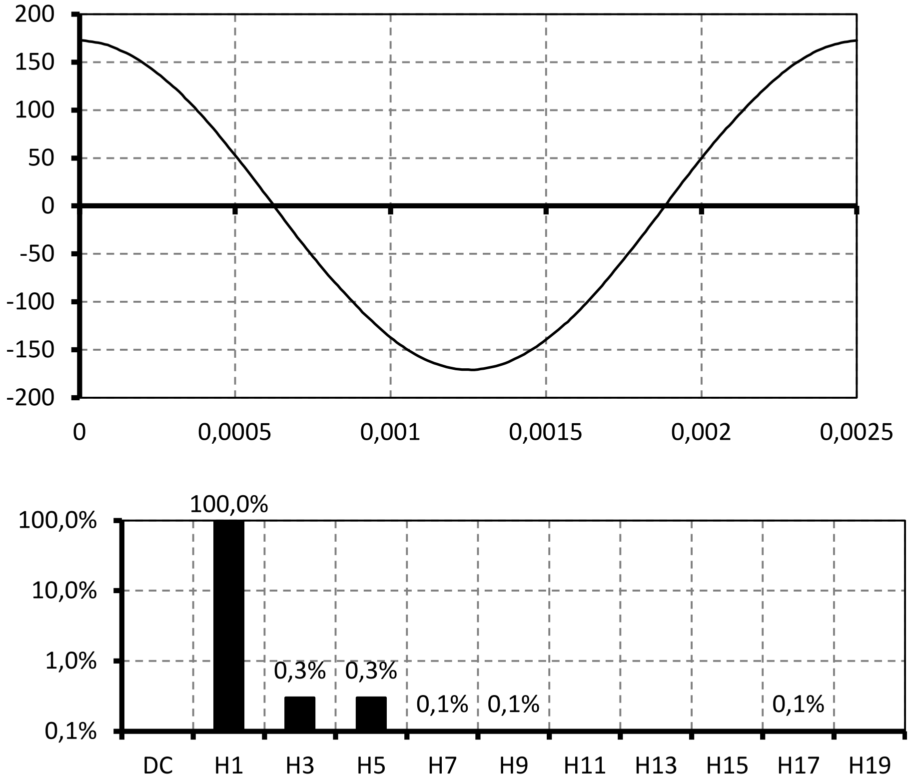

Figure 6.8 Designed cylindrical-rotor BSG nominal no load phase voltage ($EMF_{as}(t)$) measurement.
Amplitudes of $EMF_{as}(t)$ harmonics: $E_{0an1h} = 171\ V\ (100\%)$

The resistances of the MSG armature and field are measured. The values of non saturated inductances are approximated from machine geometry (appendix B) and are established from measurements (appendix E). The damper cages circuit parameters are referred to field winding in order to decrease the disproportion in values of the inductances and resistances between the stator and rotor cages.

$$N'_{kd} = N'_{kq} = N'_{fd} \qquad (6.8)$$

This helps with the numerical solver stability during simulations. The final circuit parameters for cylindrical-rotor and salient main generator of BSGs are as follows.

Salient-pole commercial GT40PCz8	Cylindrical-rotor protype BSG:
number Lmd=907E-6	number Lmd=572E-6
number Lls=35E-6	number Lls=35E-6
number Lsfd=4.21E-3	number Lsfd=2.04E-3
number Lskd=605E-6	number Lskd=381E-6
number Lskq=605E-6	number Lskq=381E-6
number Lmfd=29.3E-3	number Lmfd=11E-3
number Lmkd=605E-9	number Lmkd=381E-6
number Lmkq=605E-9	number Lmkq=381E-6
number Lfdkd=4.21E-3	number Lfdkd=2.04E-3
number Llfd=262E-6	number Llfd=834E-6
number Llkd=19E-6	number Llkd=55E-6
number Llkq=29E-6	number Llkq=80E-6
number Rs=0.022	number Rs=0.022
number Rfd=0.31	number Rfd=0.31
number Rkq=6E-3	number Rkq=6E-3
number Rkd=6E-3	number Rkd=6E-3
number Rex=4.71	number Rex=4.71
number k_iex=30	number k_iex=30
number p=3	number p=3
number fe=400	number fe=400
number Bm=1m	number Bm=1m
number Jw=0.01	number Jw=0.01

The saturation of the magnetic materials is implemented like described in section 6.2 and is measured as average no load EMF RMS value curve in function of the exciter field current at constant speed of 8000rpm (figure 6.9). The nominal value of line to line voltage for the studied BSGs is 208V (dotted line on figure 6.9).

As explained in chapter 4, because of selected material for the prototype main generator field metal sheet core (M530-50A) and the prototype building process (laser cutting) the commercial BSG has a no load nominal excitation current of about 0.5A and the designed prototype of 1.05A.

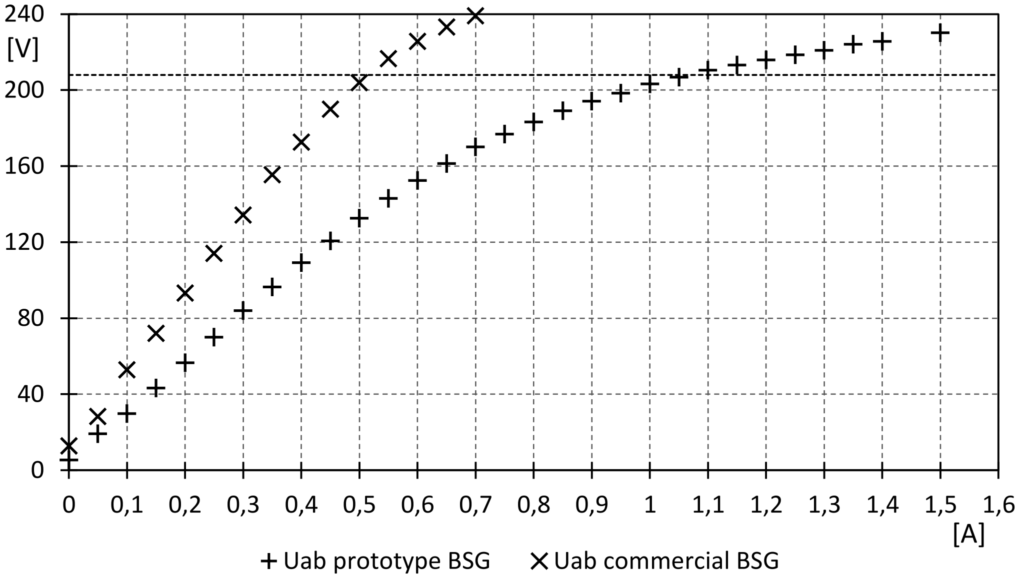

Figure 6.9 The no load EMF (line to line value) in function of exciter field current for commercial generator (Uab commercial GT40PCz8) and prototype generator (Uab prototype BSG) BSG

6.4 SUMMARY

The BSG models elaborated using MAST Language are presented in appendix D. Calculated parameters of commercial and prototype generator are implemented in Synopsys/Saber. The fundamental 3'rd and 5'th space harmonics of stator and rotor MMF are included in model as well as average value and first harmonic of air-gap length distribution for the salient-pole machine. The saturation of magnetic core is modelled by coefficient *Ksat* in MAST language model. This coefficient is calculated using the total magnetising current.

7 DESIGN OF BSG TEST-BENCH

7.1 INTRODUCTION

In this chapter the design of the BSG test-bench is presented. The idea for presented solution of the test-bench is drown is based on the existing test-bench in laboratory of the Faculty of Ocean Engineering and Ship Technology, where commercial generators GT40PCz8 are tested. In order to decrees the costs of the entire test-bench a DC motor was selected as a prime mover.

7.2 TEST-BENCH DESIGN

Most difficult part of designing the test bench was achieving the rotating speed of 8000rpm and power output of 50% of nominal generator power ($\sim 16\mathrm{kW}$). As prime mover for designed prototype BSG a DC motor was used. Parameters of this motor are presented in table 7.1.

Table 7.1 DC machine supplying BSG:

Parameter	Value	Description
P_n	$24\mathrm{kW}$	Nominal power of the machine
I_{an}	$124\mathrm{A}$	Nominal armature current
U_{an}	$220\mathrm{V}$	Nominal armature voltage
n_n	$1450\mathrm{rpm}$	Nominal rotation speed
I_{fn}	$1.2\mathrm{A}$	Nominal excitation current
U_{fn}	220	Nominal excitation voltage

In order to achieve speed of 8000rpm a synchronous belt transmission was selected. The parameters of the transmission are presented in table 7.2.

Table 7.2 Synchronous belt transmission parameters:

Parameter	Value
Speed ratio	5.54 up
Low speed	1450rpm
High speed	8030.8
Rated load	60.31kW
Belt pull	1076N
Rim/Belt Speed	27,8 m/s

Figure 7.1 shows the concept of the test bench based on selected DC motor and belt transmission. Detailed documentation of this concept is in appendix F.

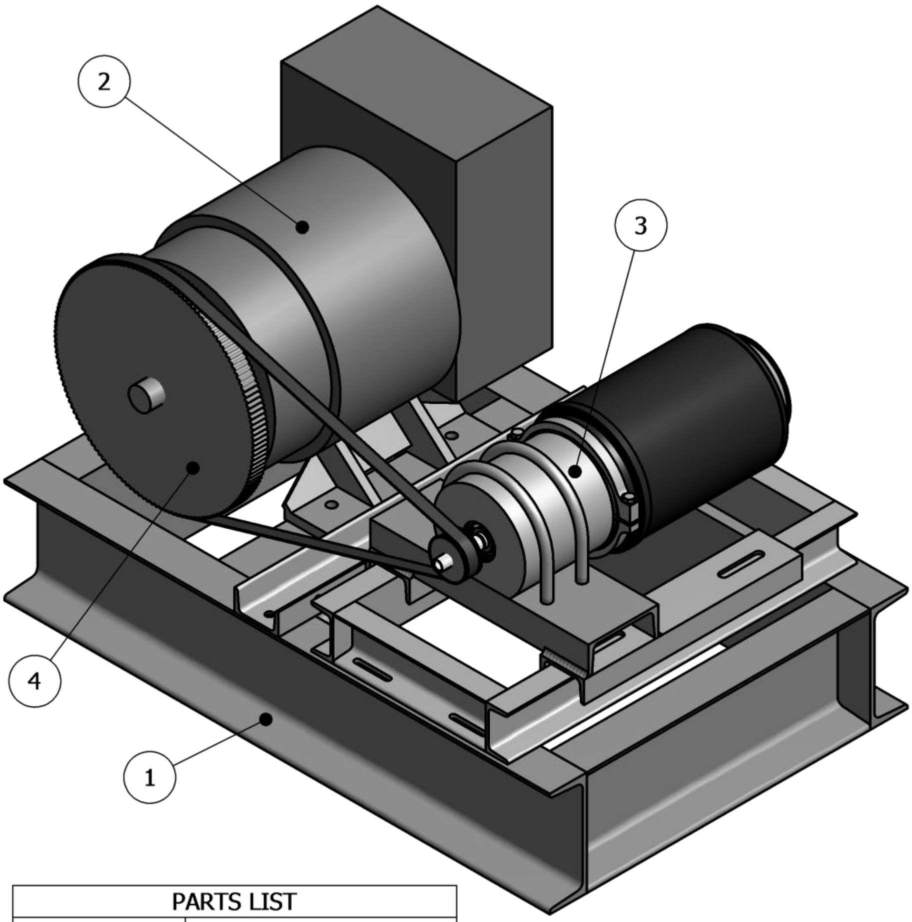

PARTS LIST	
ITEM NUMBER	PART NAME
1	Base
2	DC Motor
3	BSG
4	Belt Transmission

Figure 7.1 View of the concept of the test bench

The main components of the test-bench are: DC motor (2) and the prototype BSG (3). The generator GT40PCz8 enclosure is a flange mounted case. Figure 7.2 shows the view of generator housing with flange mounting and the shaft on the right.

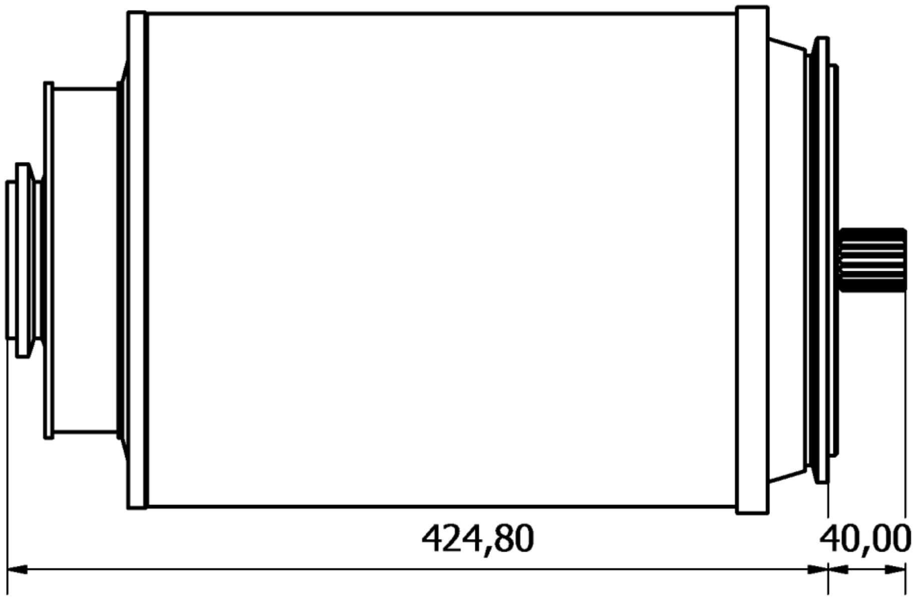

Figure 7.2 BSG enclosure view

The shaft of the machine consists of two parts – the inner shaft and the outer shaft. On the outer shaft component all rotors are placed for the PMG subexciter, the exciter and the main generator. Figure 7.3 shows BSG rotor parts including inner and outer shafts.

The inner shaft is powered from external shaft through a spline joint. This allows the BSG to operate in environment where it is under high forces in different direction without stressing the joint or the shaft. In a combat helicopter where BSG GT40PCz8 is used it is under extreme g-forces in all axes. Figure 7.4 shows the inner shaft of the BSG with its spline joint.

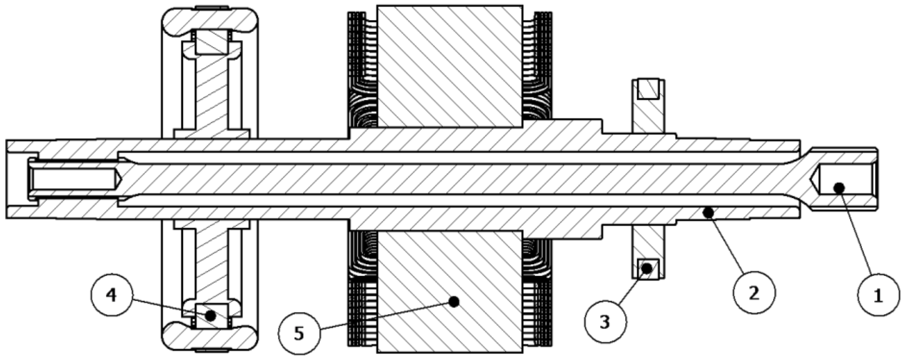

ROTOR PARTS	
NUMBER	PART NAME
1	Inner shaft
2	Outer shaft
3	Subexciter rotor
4	Exciter rotor
5	Main Generator rotor

Figure 7.3 BSG rotor parts

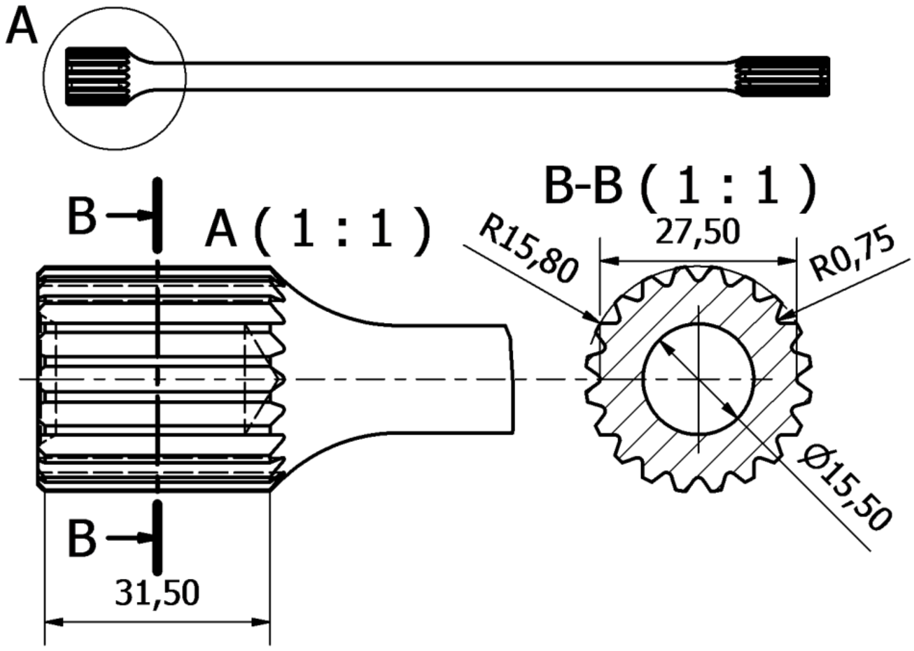

Figure 7.4 BSG inner shaft

Thanks to cooperation with Military Aviation Works No. 1 J.S.C. (MAW-1 J.S.C.) in Łódź and the Military Property Agency of Poland (donated the external part of generator spline joint - part of the gear box) it was able to design BSG mechanical coupling. Figure 7.5 shows the selected shaft of the MI-24 helicopter gearbox.

The spline connection is the same as in MI-28 helicopter in which the commercial BSG are applied.

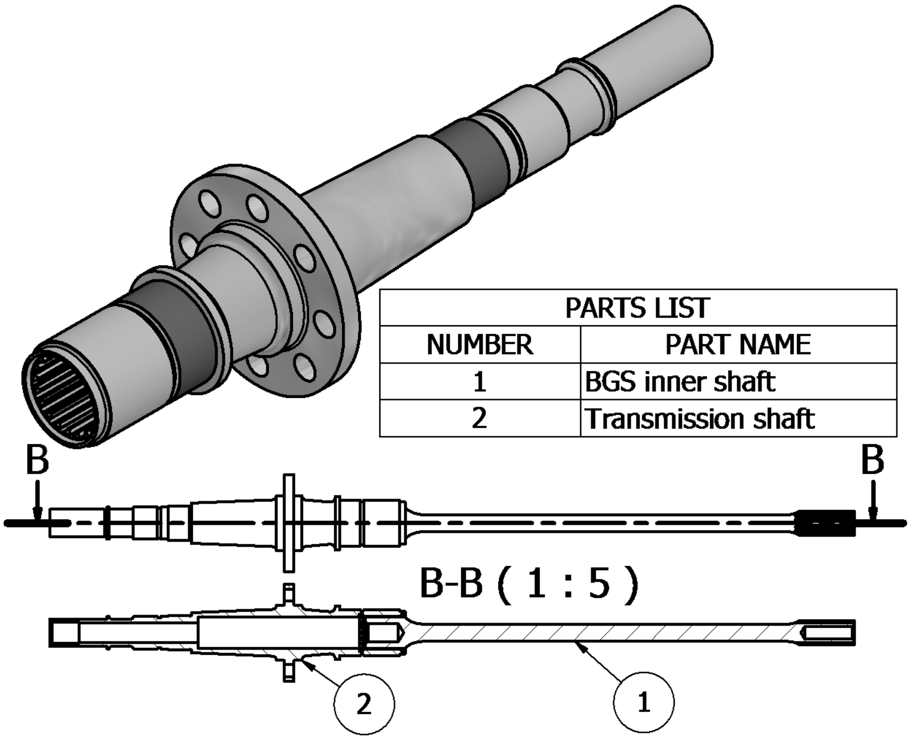

PARTS LIST	
NUMBER	PART NAME
1	BGS inner shaft
2	Transmission shaft

Figure 7.5 Transmission shaft for BSG from MI-24 helicopter

7.3 MEASUREMENTS ON THE TEST BENCH

A series of measurements were conducted on designed test bench (figure 7.6). This test has included steady state operation for:

- no load condition,
- symmetrical 3 phase short circuit condition,
- load condition.

The transient state measurements has included:

- symmetrical 3-phase short circuit,
- load switching on.

At no load condition the load (balanced impedance load – Z) was disconnected (S1 switch open – S1 is Moeller Eaton PN2-160 switch).

In the short circuit test the impedance load was equal zero (shorted terminals of the 3 phase switch S1).

In power load test the load impedance Z had a resistive component of 0.8 ohm and reactive component of 0.15 ohm (for 400 Hz). The value of reactive component was established after the measurement by calculation the power factor from phase voltage and line current. The value of this reactive component includes inductance of the entire load circuit connected to L1 L2 L3 main generator terminals.

Measurement of the subexciter EMF frequency is conducted in order to observe the rotational speed of the BSG.

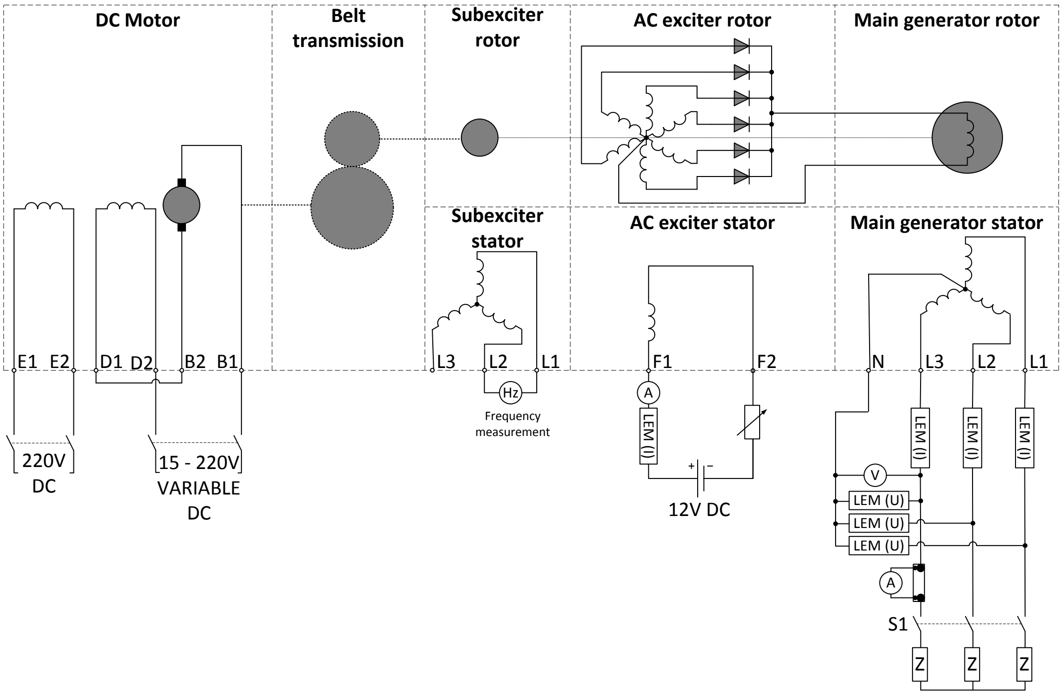

Figure 7.6 Test bench measurement schematic

7.4 SUMMARY

Designed test-bench was built by the “EPiMP” company [115]. During the construction process some changes needed to be applied to the construction of the transmission shaft enclosure. The transmission belt is a Gates PwerGrip GT2 8M which width is 30mm was selected. This drive belt is capable of transferring power up to 50kW in presented configuration. However belt linear speed in this configuration reaches 27.8m/s and is near the limit for this configuration. That means that for achieving higher speed the test bench would have to be modified.

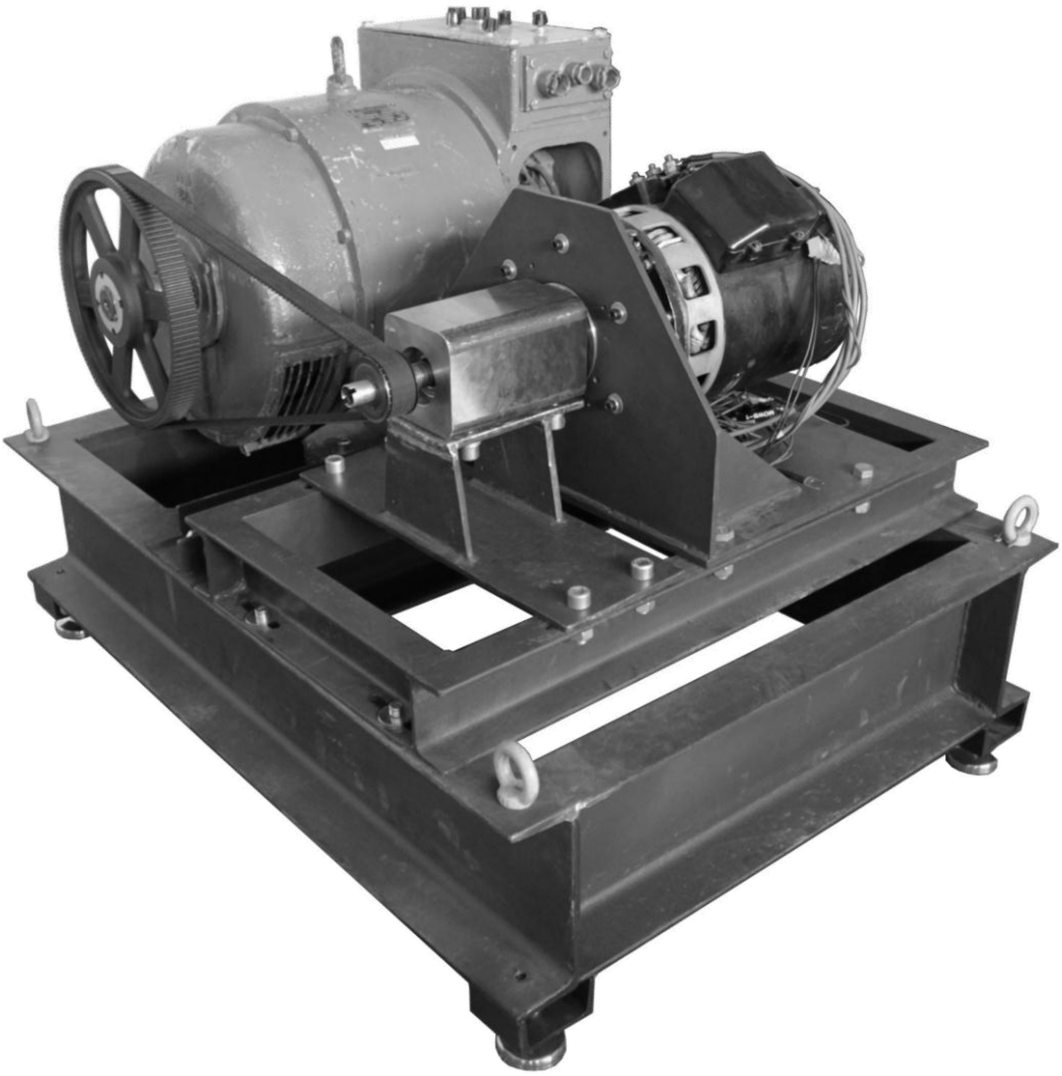

Figure 7.7 Built test bench

The selected bearing for that enclosure were 6306 and 6208, both bearings capable of sustaining 8000rpm constant speed. Selected belt transmission system does not require additional tensioning pulleys, as it was considered earlier in the design process.

8 EXPERIMENTAL ANALYSIS OF BSGS – MEASUREMENTS AND MODEL VERIFICATION

8.1 INTRODUCTION

One of the most important elements in the application of AEPS simulation to design practice is the validation of the simulation results. The prototype GT40PCz8 generator and the commercial generator GT40PCz8 analyses by simulation and empirical testing shall be presented to prove that the Synopys/Saber models' output behaviour have sufficient accuracy for their intended purpose or use over the domain of intended application. It should be noted that even though an insufficient accuracy occurs, this may be not due to simulation errors but due to the inadequate and incorrect data, necessary for model building and testing.

A comparison between the simulation and empirical results has been carried out for the following BSG performances:

- no load at steady state,
- 3-phase short circuit current at steady state,
- load at steady state,
- 3-phase short circuit at transient,
- power load switching on at transient.

These BSG study and operating conditions were selected for thorough verification of the procedures and generator models.

The analysis have been carried out for the prototype generator and for the commercial generator GT40PCz8. Both measurements were conducted at nominal speed of 8000rpm. As a load for the measurements a 3-phase resistor was used. However, the resistance values for test on built test bench and for test bench in laboratory of the Faculty of Ocean Engineering and Ship Technology were different, due to the fact of using different equipment (load resistor).

8.2 NO LOAD STEADY STATE

8.2.1 NO LOAD VOLTAGE FOR COMMERCIAL GENERATOR GT40PCZ8

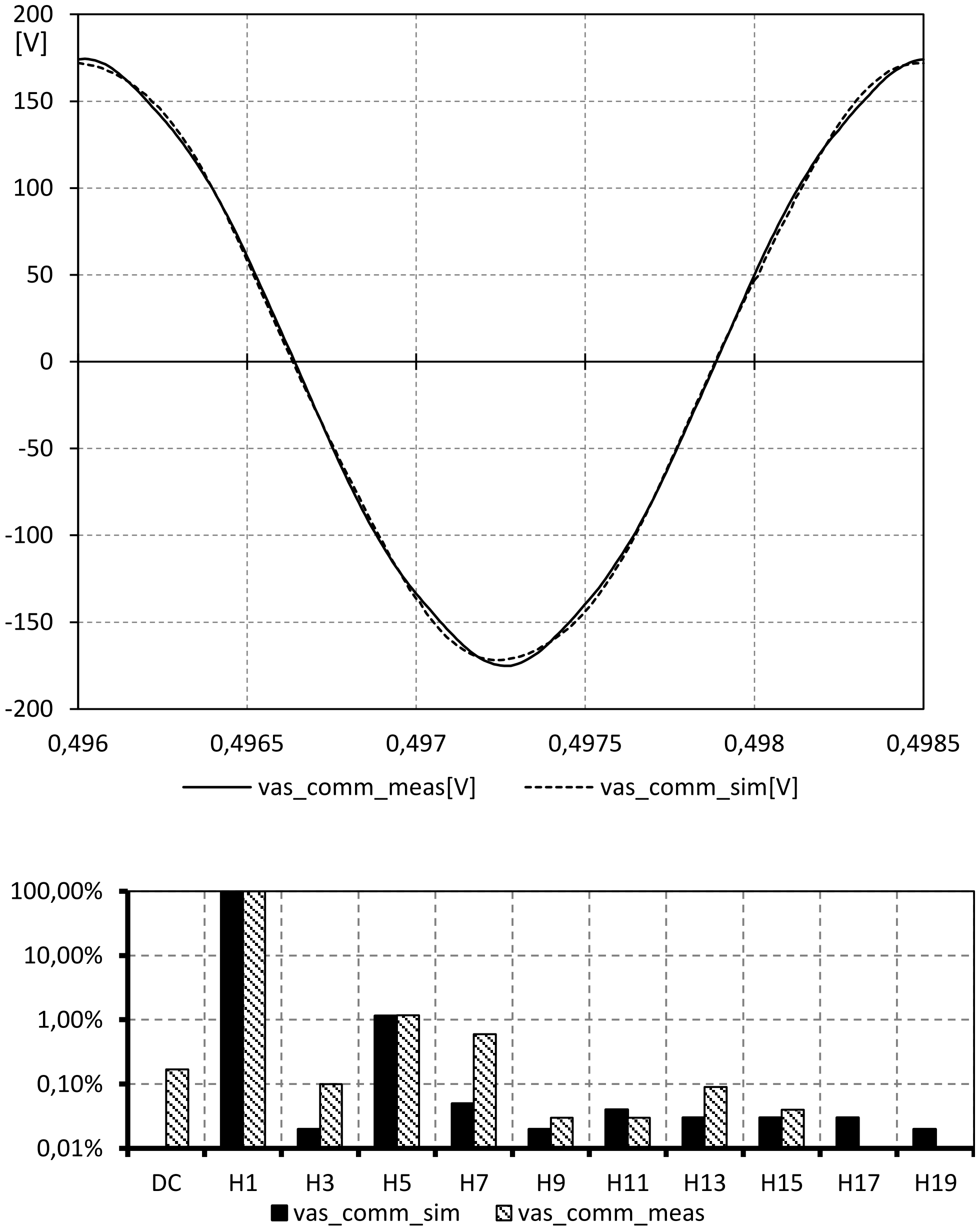

Figure 8.1 No load voltage waveform and harmonics of the commercial GT40PCz8:
vas_comm_meas – measured armature phase voltage,
vas_comm_sim – simulated armature phase voltage

Table 8.1 Parameters of no load voltage at steady state for commercial GT40PCz8

Parameter	Measurement	Simulation	Difference
Voltage fundamental component amplitude	172.02 V	172.60 V	0.34%
Voltage 3'rd harmonic component amplitude	0.17 V	0.04 V	0.08%
Voltage 5'th harmonic component amplitude	2.02 V	2.01 V	0.01%

As can be observed in figure 8.1 the model includes apart from the fundamental component also the 5th harmonic of the stator and rotor MMFs. Table 8.1 shows the amplitudes of the commercial salient pole GT40PCz8 BSG voltage in no load conditions. As can be observed the third harmonic amplitude level is negligible. The 5'th harmonic has amplitude of 1.17% of fundamental component. The difference between measurement and simulation is low.

The difference between measured and simulated values is calculated as a relative error referred to fundamental component:

$$\delta = \frac{|x_{measured} - x_{simulated}|}{|x_{measured\ fundamental\ component}|} \times 100\% \tag{8.1}$$

8.2.2 NO LOAD VOLTAGE FOR PROTOTYPE BSG.

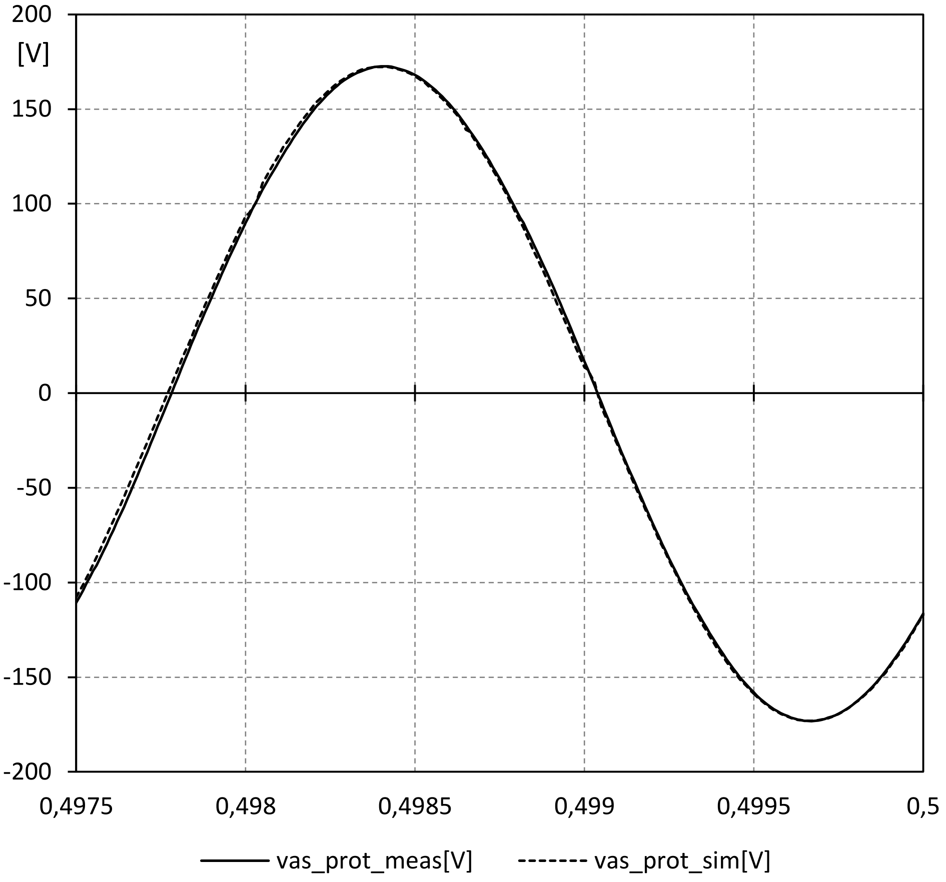

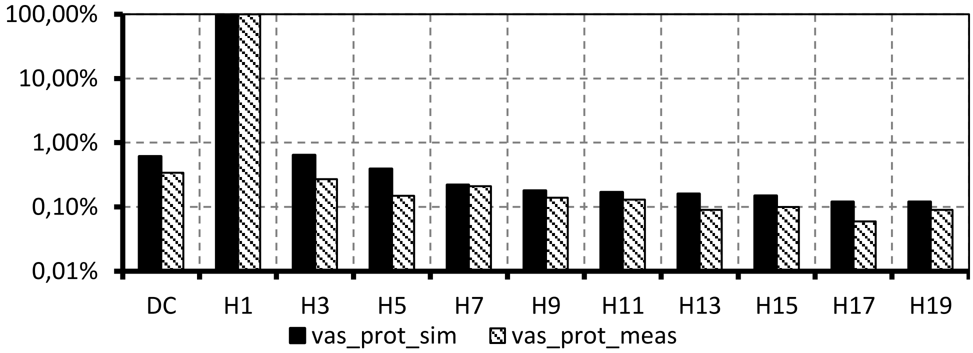

Figure 8.2 No load voltage waveform and harmonics of the prototype BSG: vas_prot_meas – measured armature phase voltage, vas_prot_sim – simulated armature phase voltage

Table 8.2 Parameters of no load voltage at steady state for prototype BSG

Parameter	Measurement	Simulation	Difference
Voltage fundamental component amplitude	172.56 V	172.77 V	0.12%
Voltage 3’rd harmonic component amplitude	0.46 V	1.11 V	0.38%
Voltage 5’th harmonic component amplitude	0.26 V	0.67 V	0.24%

In developed prototype the level of higher harmonics is very low (less than 1% of the fundamental component). Table 8.2 shows the amplitudes of voltage at no load conditions of the prototype BSG. For this BSG a model incorporating only the fundamental frequency harmonic is as adequate as developed model in terms of poliharmonic character of air-gap flux distribution.

8.3 3 PHASE SHORT CIRCUIT STEADY STATE

8.3.1 STEADY STATE SHORT CIRCUIT FOR COMMERCIAL GT40PCz8

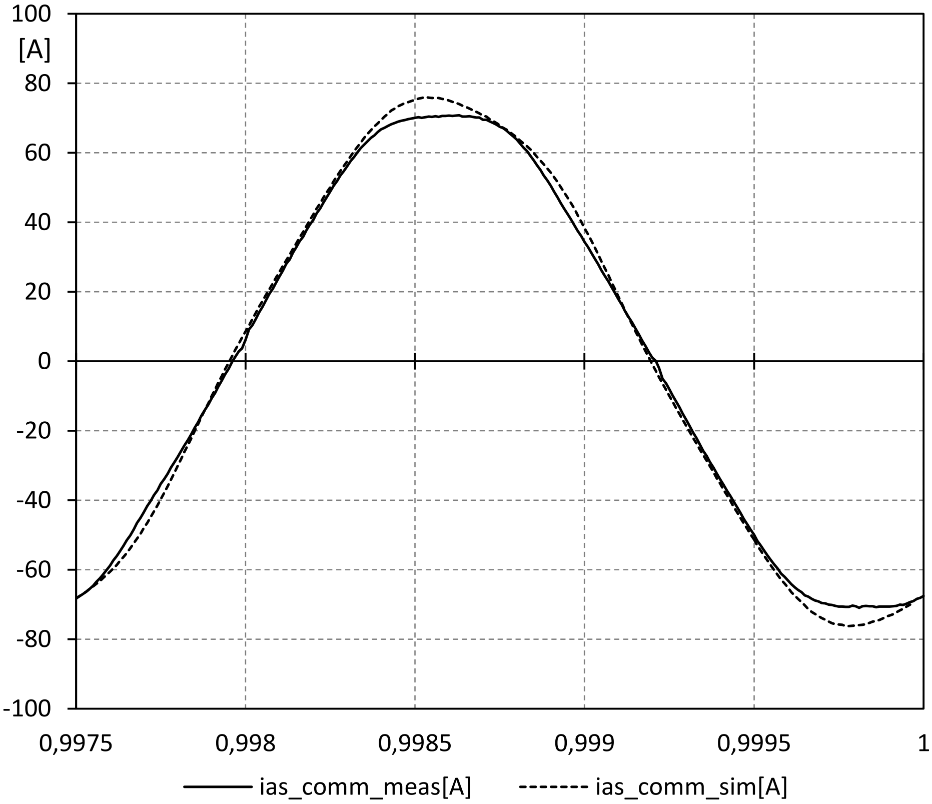

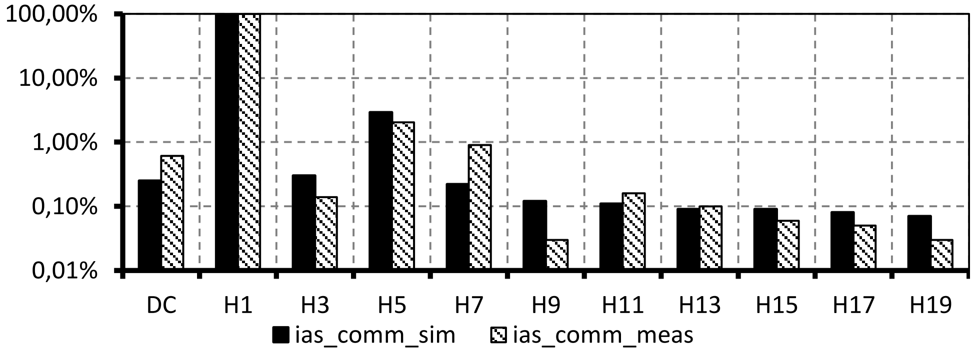

Figure 8.3 3 phase short circuit waveform and harmonics of the commercial GT40PCz8:
ias_comm_meas – measured armature line current,
ias_comm_sim – simulated armature line current

Table 8.3 Parameters of short circuit at steady state for commercial GT40PCz8

Parameter	Measurement	Simulation	Difference
Current fundamental component amplitude	72.86 A	75.93 A	4.21%
Current 3’rd harmonic component amplitude	0.10 A	0.23 A	0.18%
Current 5’th harmonic component amplitude	1.49 A	2.22 A	1.00%

As for no load EMF measurement also in symmetrical 3 phase short circuit waveform for the commercial BSG the 5’th harmonic has a noticeable value. In measurement it is equal to 2.05% and in simulation to 2.92% of fundamental component (figure 8.3). The difference in measurements and simulations can be explained by simplifications made in developed model – like assumption that entire machine and all harmonics have the same level of saturation. During the no load operation some parts of the machine can have different level of saturation and in short circuit test the demagnetising armature reaction significantly decreases the linkage flux amplitude thus causing that the machine operates in nonsaturated state.

8.3.2 STEADY STATE SHORT CIRCUIT FOR PROTOTYPE BSG

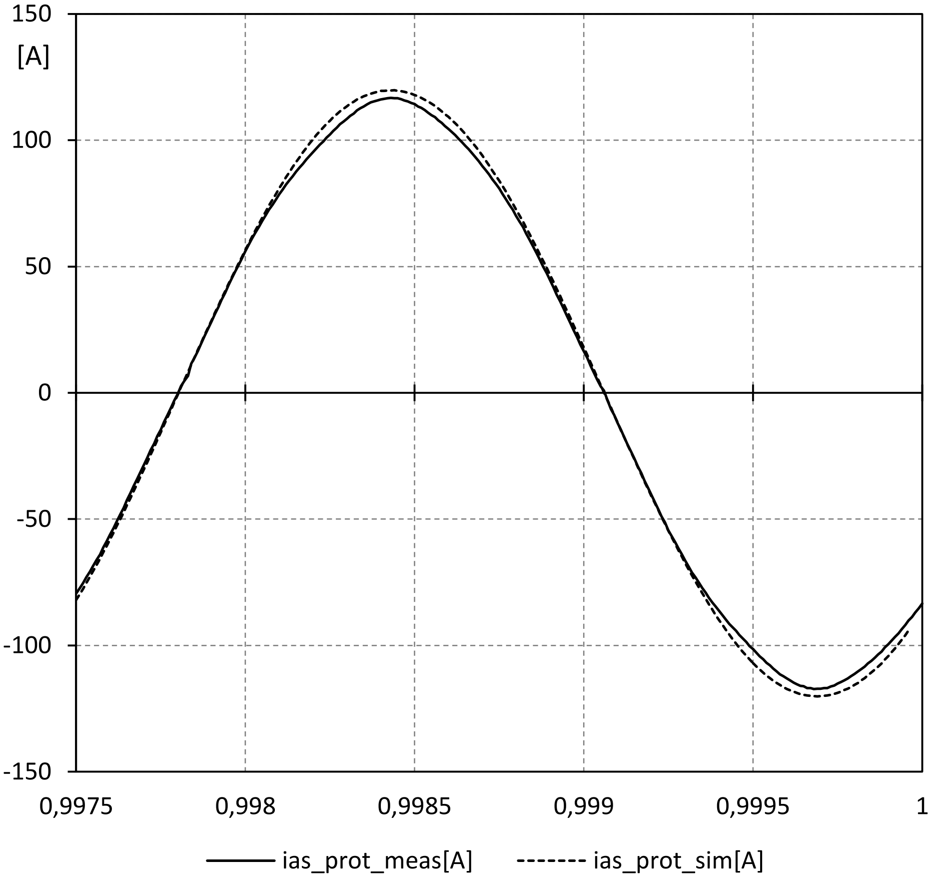

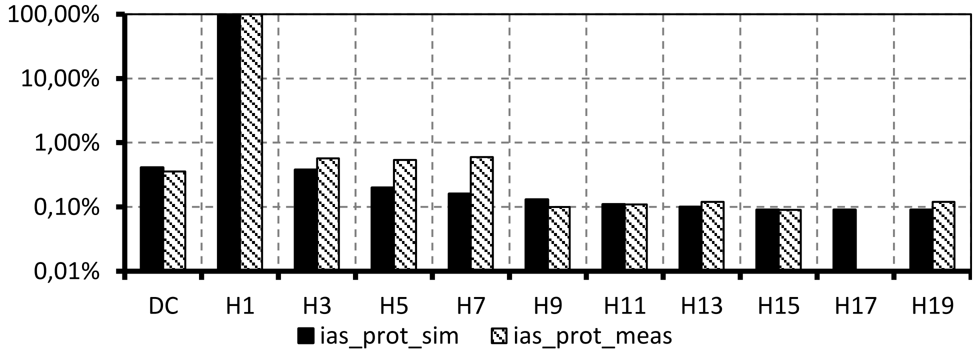

**Figure 8.4 3 phase short circuit current waveform and harmonics of the prototype BSG:
ias_prot_meas – measured armature line current,
ias_prot_sim – simulated armature line current**

Table 8.4 Parameters of short circuit at steady state for prototype BSG

Parameter	Measurement	Simulation	Difference
Current fundamental component amplitude	115.56 A	119.87 A	3.73%
Current 3’rd harmonic component amplitude	0.66 A	0.46 A	0.17%
Current 5’th harmonic component amplitude	0.62 A	0.24 A	0.33%

As in no load EMF measurement also in symmetrical 3 phase short circuit waveform for the prototype BSG the higher harmonics amplitudes of armature current have negligible levels referred to fundamental component.

8.4 LOAD STEADY STATE

8.4.1 STEADY STATE LOAD VOLTAGE AND CURRENT FOR COMMERCIAL GT40PCZ8

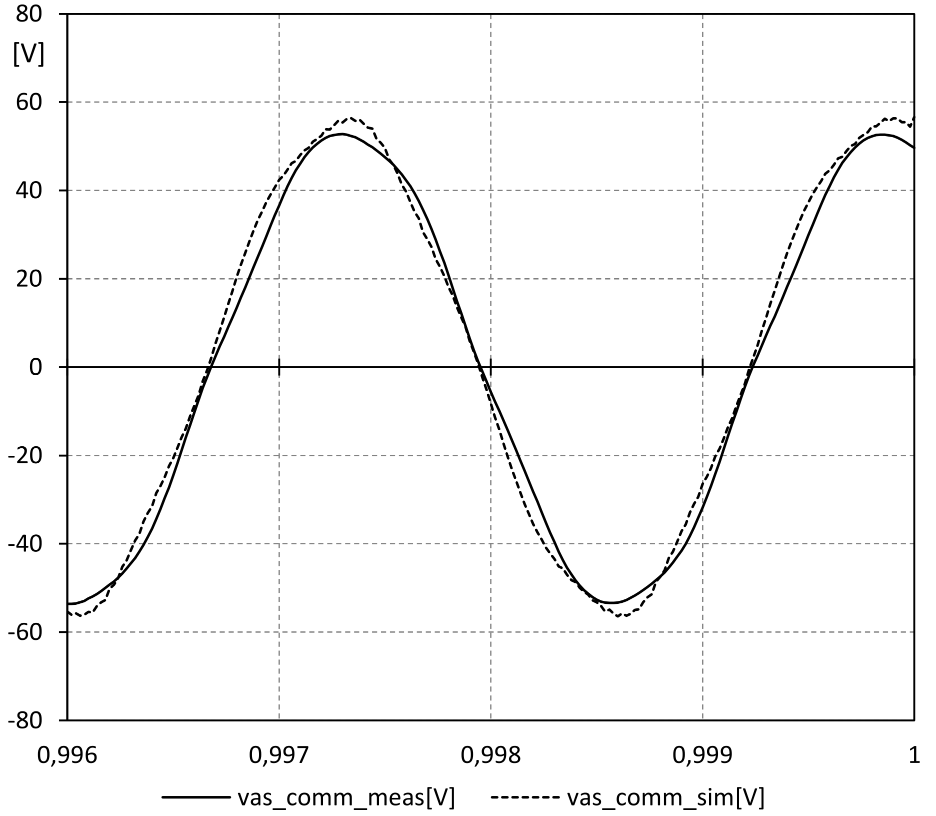

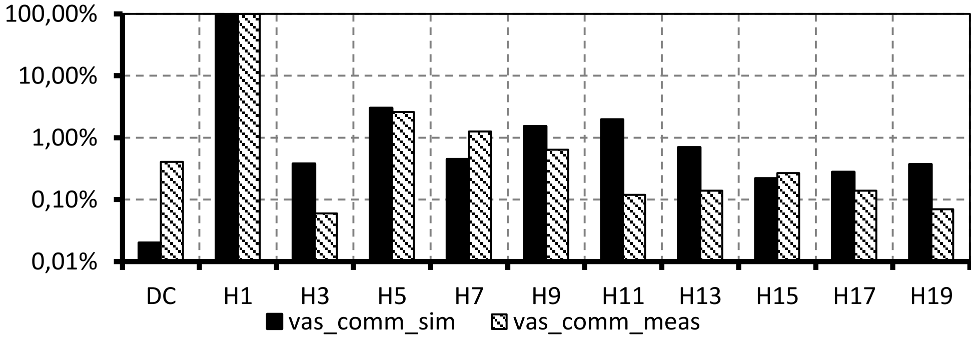

Figure 8.5 Waveform and harmonics of armature voltage at load conditions for the commercial GT40PCz8 (balanced delta connected load R = 2.4 ohm, X = 0.64 ohm, PF = 0.96):
vas_comm_meas – measured armature phase voltage,
vas_comm_sim – simulated armature phase voltage

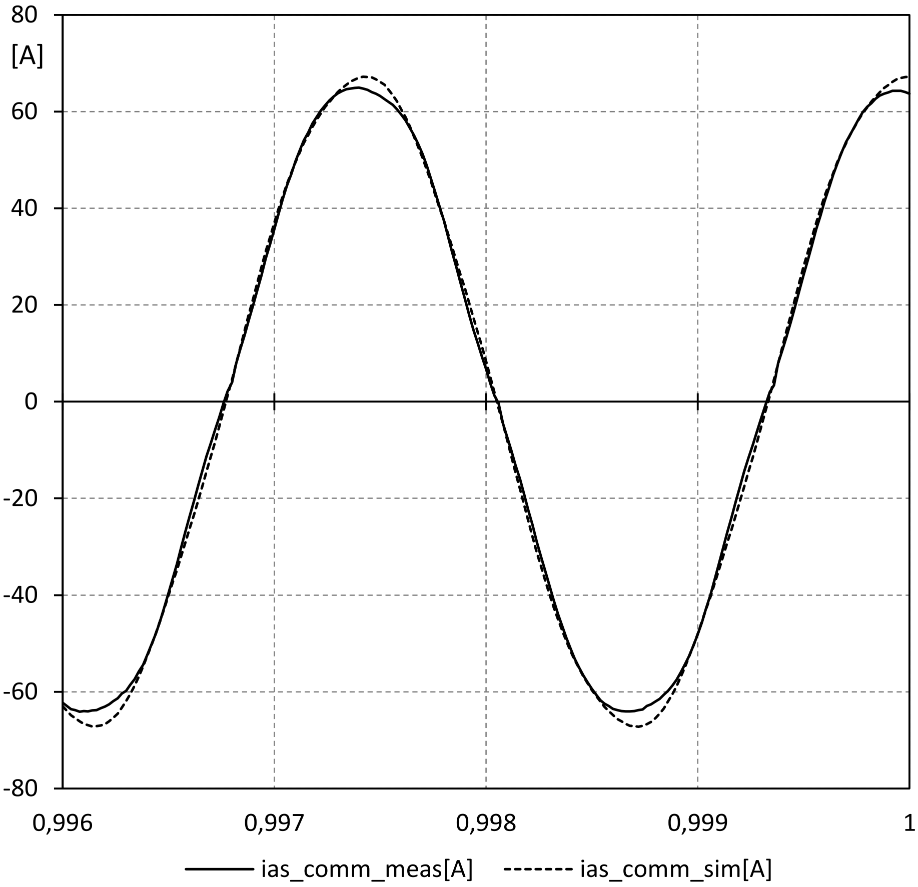

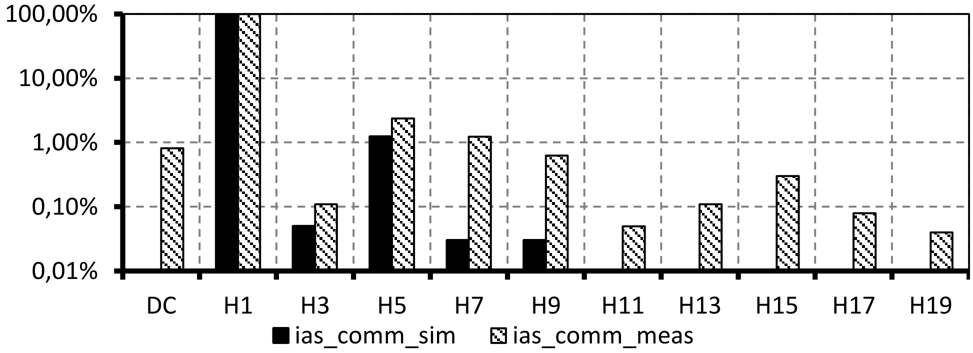

Figure 8.6 Waveform and harmonics of armature current at load conditions for the commercial GT40PCz8 (balanced delta connected load R = 2.4 ohm, X = 0.64 ohm, PF = 0.96):
ias_comm_meas – measured armature line current,
ias_comm_sim – simulated armature line current

Table 8.5 Voltage parameters for load condition at steady state for commercial GT40PCz8 BSG

Parameter	Measurement	Simulation	Difference
Voltage fundamental component amplitude	53.38 V	55.59 V	4.14%
Voltage 3'rd harmonic component amplitude	0.03 V	0.21 V	0.34%
Voltage 5'th harmonic component amplitude	1.40 V	1.67 V	0.51%

Table 8.6 Parameters of load condition current in steady state for commercial GT40PCz8 BSG.

Parameter	Measurement	Simulation	Difference
Current fundamental component amplitude	65.61 A	67.61 A	3.05%
Current 3'rd harmonic component amplitude	0.07 A	0.03 A	0.06%
Current 5'th harmonic component amplitude	1.55 A	0.84 A	1.08%

As in previous tests the 5'th harmonic in commercial BSG is present in power load performance. The measurement is conducted in steady state after power load connection. There is no excitation current regulator and the excitation current has the same value as in no load conditions. Because of armature reaction the amplitude of fundamental frequency component of armature voltage is equal to 53.38V (figure 8.5) and 32% of nominal phase voltage amplitude. The active power in load is 5.04kW And the power factor is 0.96. For load a delta connected resistor was used, with resistance of 2.4ohm in each branch. The reactive power is present due to long connections, the construction of the resistor and the leakage inductance of the machine. The difference in voltage and current 5'th harmonic may be caused by simplifications in the model (uniform level of saturation in the entire magnetic core). However the difference in 5'th harmonic of the current between measurement and simulation in reference to the fundamental frequency component is 1.2% (figure 8.6).

8.4.2 STEADY STATE LOAD VOLTAGE AND CURRENT FOR PROTOTYPE BSG

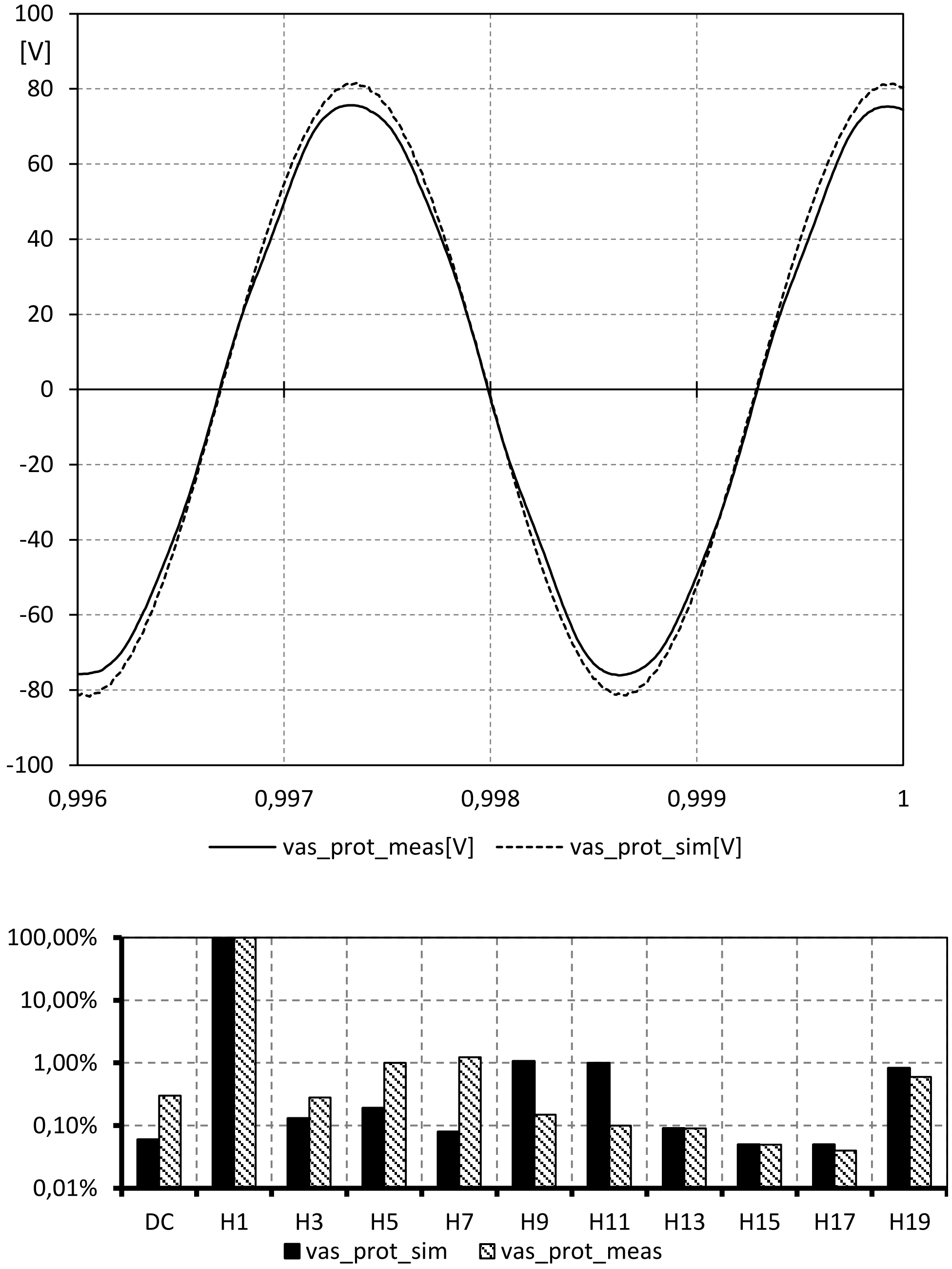

Figure 8.7 Waveform and harmonics of armature voltage at load conditions for the prototype BSG (R = 0.8 ohm, X = 0.15 ohm, PF = 0.98): vas_prot_meas – measured armature phase voltage, vas_prot_sim – simulated armature phase voltage

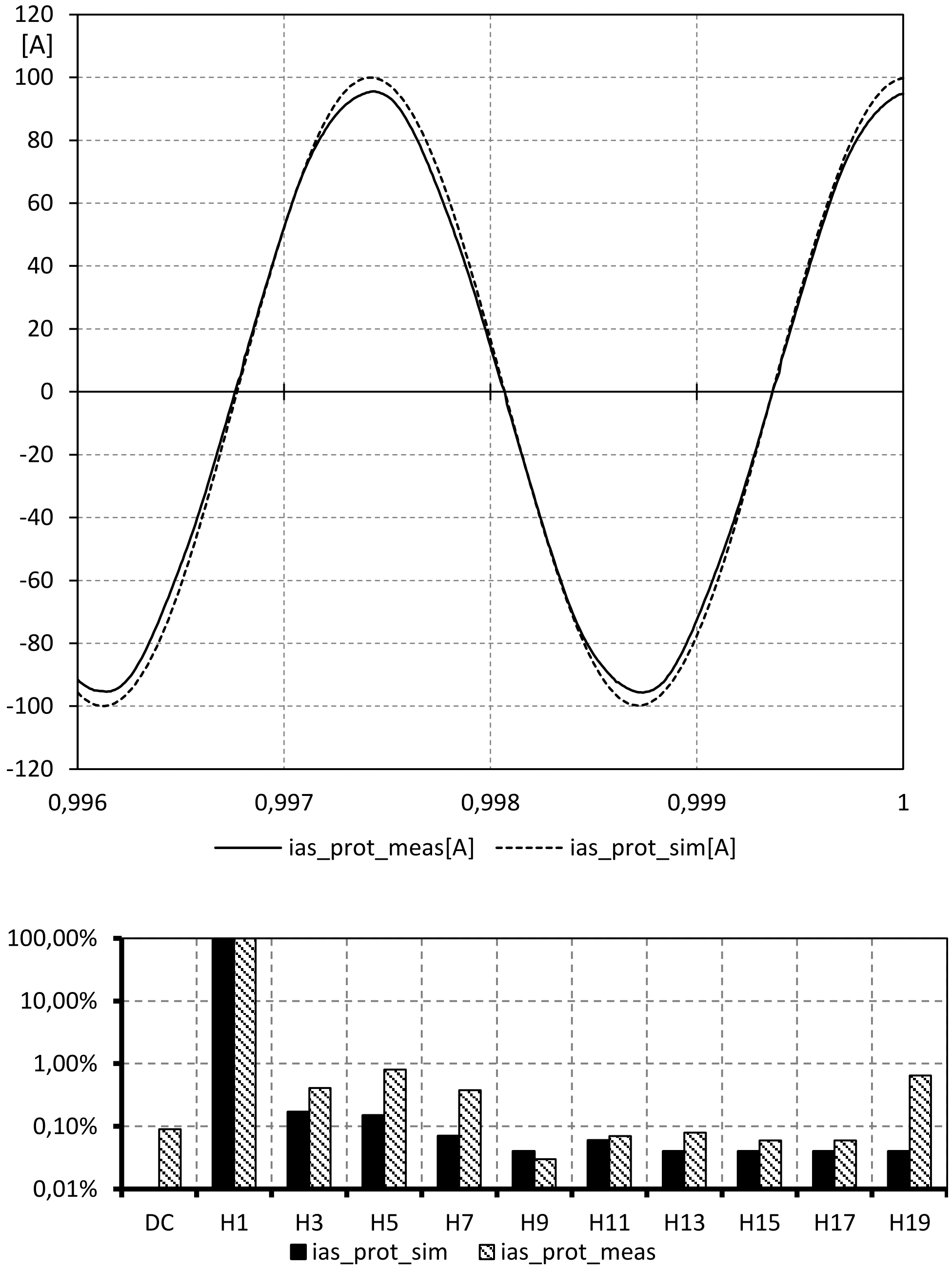

Figure 8.8 Waveform and harmonics of armature current at load conditions for the prototype (BSG R = 0.8 ohm, X = 0.15 ohm, PF = 0.98): ias_prot_meas – measured armature line current, ias_prot_sim – simulated armature line current

Table 8.7 Parameters of load condition voltage in steady state for prototype BSG

Parameter	Measurement	Simulation	Difference
Voltage fundamental component amplitude	76.10 V	80.74 V	6.10%
Voltage 3’rd harmonic component amplitude	0.21 V	0.11 V	0.13%
Voltage 5’th harmonic component amplitude	0.77 V	0.15 V	0.81%

Table 8.8 Parameters of load condition current in steady state for prototype BSG

Parameter	Measurement	Simulation	Difference
Current fundamental component amplitude	95.48 A	99.79 A	4.51%
Current 3’rd harmonic component amplitude	0.39 A	0.17 A	0.23%
Current 5’th harmonic component amplitude	0.77 A	0.15 A	0.65%

For the prototype non-salient pole BSG the voltage and current higher harmonics (higher then fundamental frequency) do not exceed 1% of the fundamental component. The measurement are conducted in steady state after power load connection. The machine operate without a regulator and the excitation current has the same value as in no load state. In load condition steady state measurement the amplitude of the voltage is 76.1V (figure 8.7) and 45% of nominal voltage amplitude. The load is constructed of three wye connected resistors of 0.8ohm in each branch. The active power in the measurement is 10.68kW and the power factor is 0.98. The higher value of voltage in this test as opposed to the commercial GT40PCz8 BSG is due to lower armature reaction in designed machine. This is caused by the different material used for main generator stage metal sheets core.

8.5 3 PHASE SHORT CIRCUIT TRANSIENT

8.5.1 CONDUCTED TESTS FOR COMMERCIAL GT40PCZ8

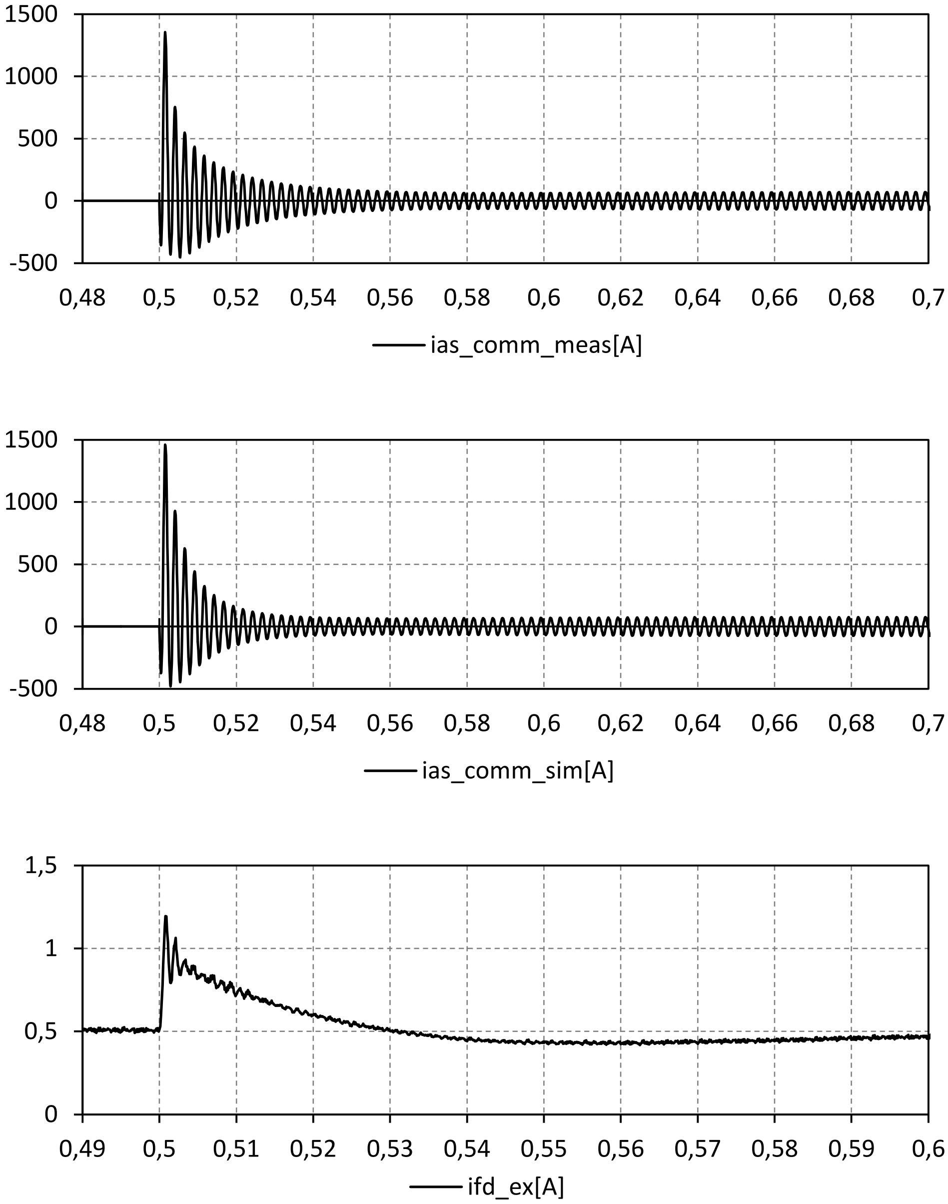

Figure 8.9 3 Waveform of phase short circuit current – transient state for the commercial GT40PCz8:
ias_comm_meas – measured armature line current,
ias_comm_sim – simulated armature line current,
ifd_ex – measured excitation current used in simulation

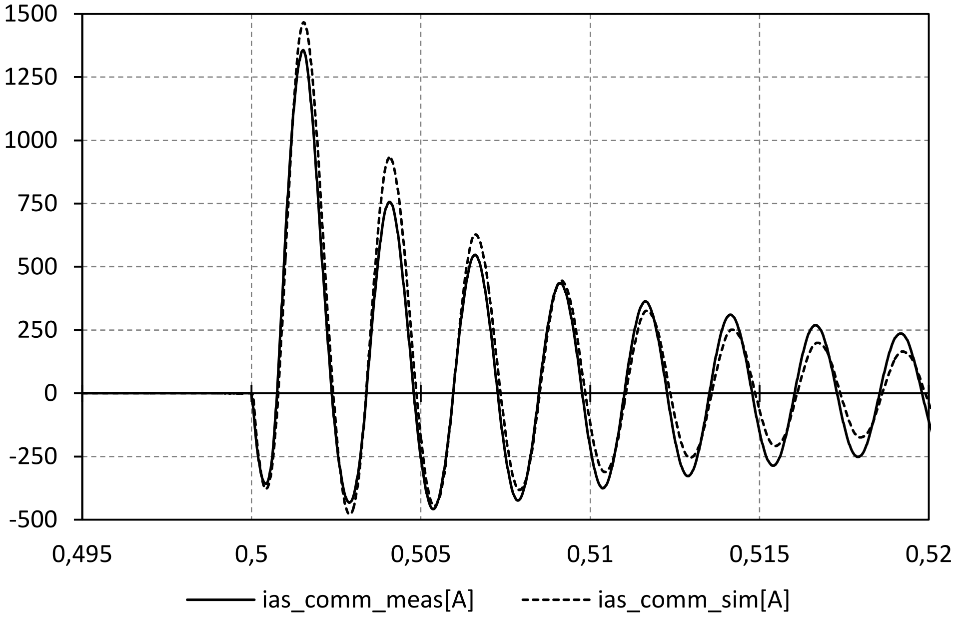

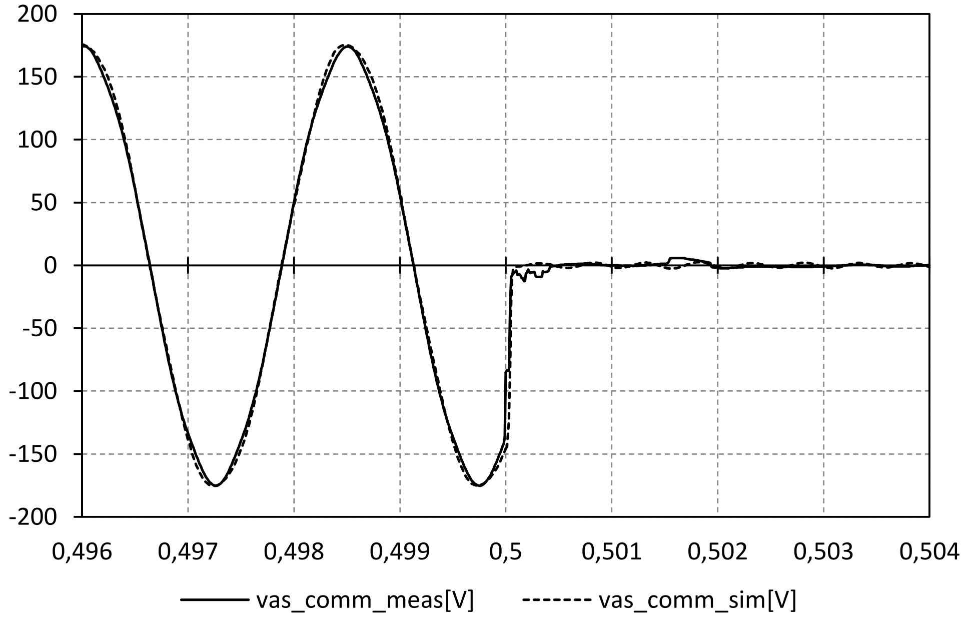

Figure 8.10 3 Waveform of phase short circuit current and voltage – transient state for the commercial GT40PCz8 BSG:
ias_comm_meas – measured armature line current,
ias_comm_sim – simulated armature line current,
vas_comm_meas – measured armature phase voltage,
vas_comm_sim – simulated armature phase voltage

Table 8.9 Parameters of short circuit current at transient state for commercial GT40PCz8

Parameter	Measurement	Simulation	Difference
Maximum value of current	1357 A	1466 A	8%
RMS value of current in steady state	50 A	53 A	6%
RMS value of phase voltage (before short circuit)	120 V	120 V	0%

As can be observed in table 8.9 armature current in steady state in simulation is 6% off from the measurement. In transient state the maximum value of armature current in simulation is 8% off from the measured value (figure 8.10).

The difference between measured and simulated values is calculated as a relative error:

$$\delta = \frac{|x_{measured} - x_{simulated}|}{|x_{measured}|} \times 100\% \tag{8.2}$$

8.5.2 CONDUCTED TESTS FOR PROTOTYPE BSG

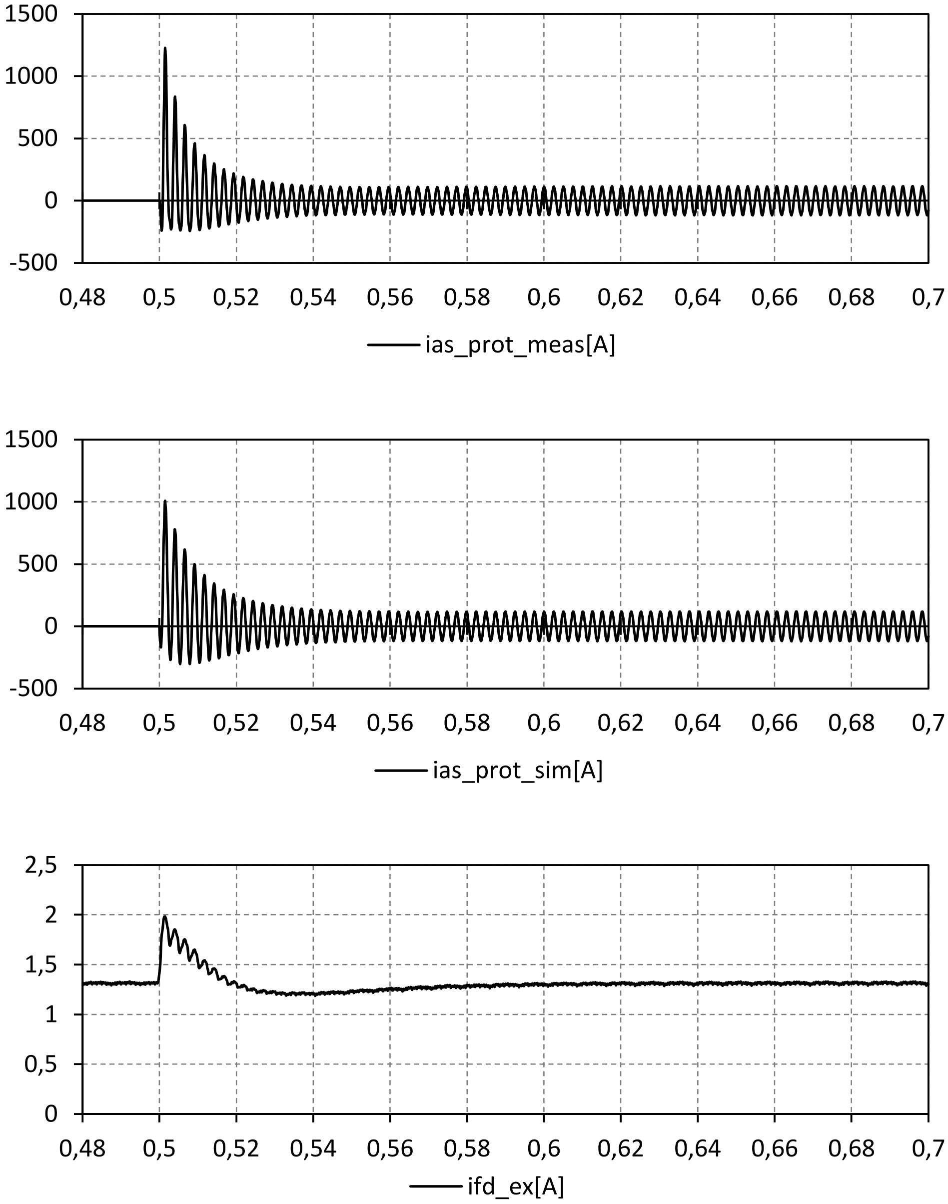

Figure 8.11 3 Waveform phase short circuit current – transient state for the prototype BSG:
ias_prot_meas – measured armature line current,
ias_prot_sim – simulated armature line current,
ifd_ex – measured excitation current used in simulation

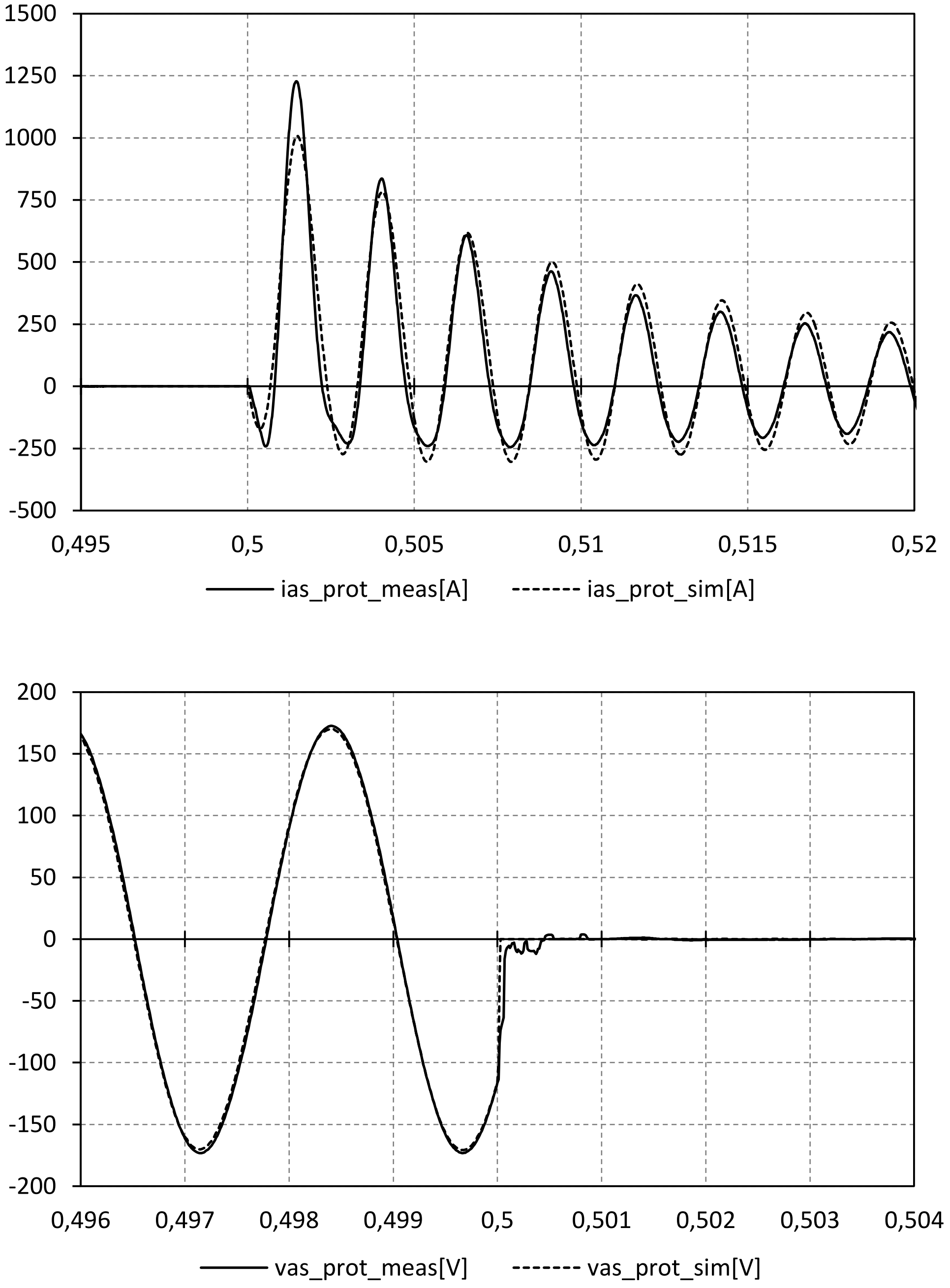

Figure 8.12 3 Waveform of phase short circuit current and voltage– transient state for the prototype BSG:
ias_prot_meas – measured armature line current,
ias_prot_sim – simulated armature line current,
vas_prot_meas – measured armature phase voltage,
vas_prot_sim – simulated armature phase voltage

Table 8.10 Parameters of short circuit at transient state for prototype BSG

Parameter	Measurement	Simulation	Difference
Maximum value of current	1228 A	1007 A	18%
RMS value of current in steady state	81 A	84 A	4%
RMS value of phase voltage (before short circuit)	120 V	120 V	0%

As can be observed in table 8.10 armature current in steady state in simulation is 4% off from the measurement. In transient state the maximum value of armature current in simulation is 18% off from the measured value (figure 8.12). The difference in transient state can be explained by simplification made in model structure. The damping cage is modelled by single branch circuits in direct and quadrature axis. The maximum value and the time constant of armature current transient state depend upon the value of damper cage leakage inductances and resistances. These parameters are established from short circuit transient state analysis (Appendix E) and are a compromise in representation of transient state maximum amplitude and time constant in measurement.

8.6 POWER LOAD SWITCHING ON

8.6.1 CONDUCTED TESTS FOR COMMERCIAL GT40PCZ8

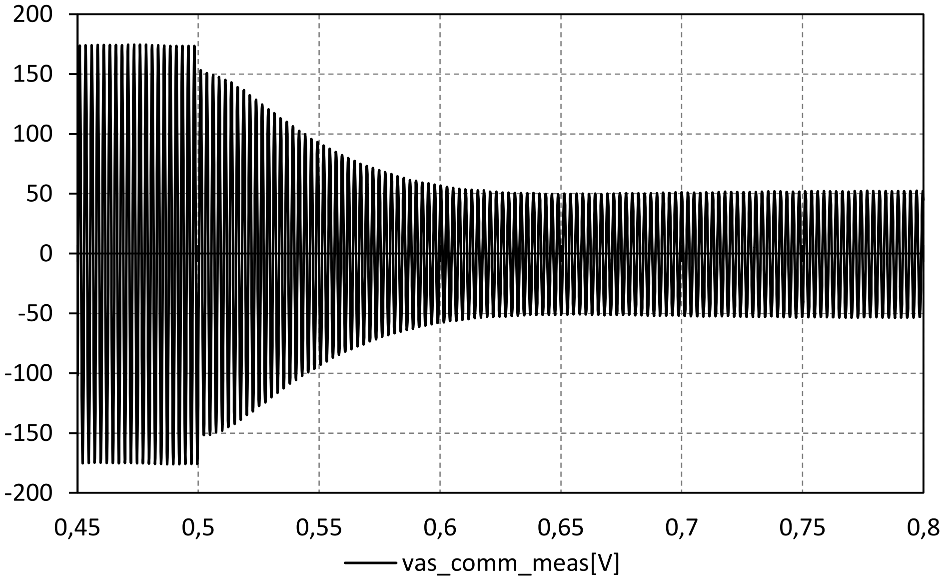

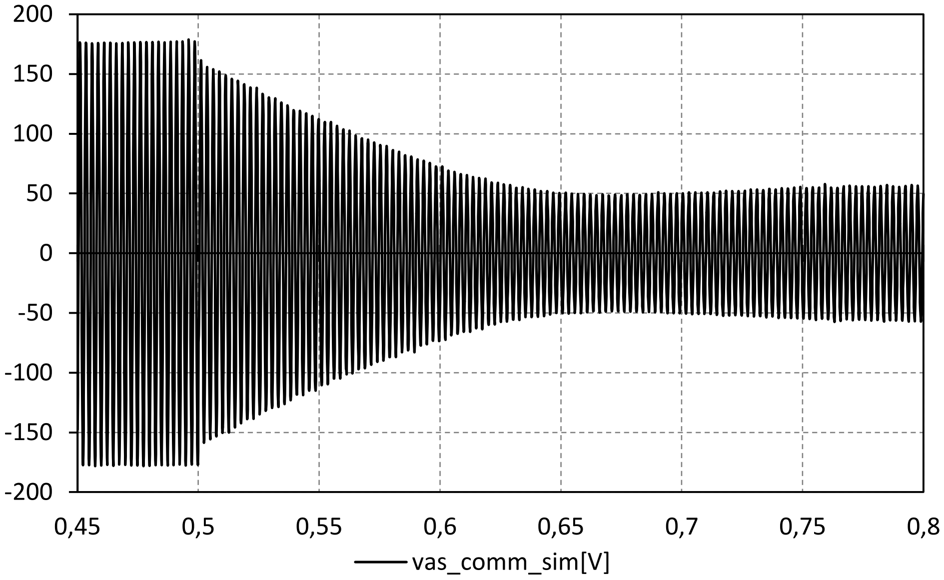

Figure 8.13 Waveform voltage – transient state at load for the commercial GT40PCz8:
vas_comm_meas – measured armature phase voltage,
vas_comm_sim – simulated armature phase voltage

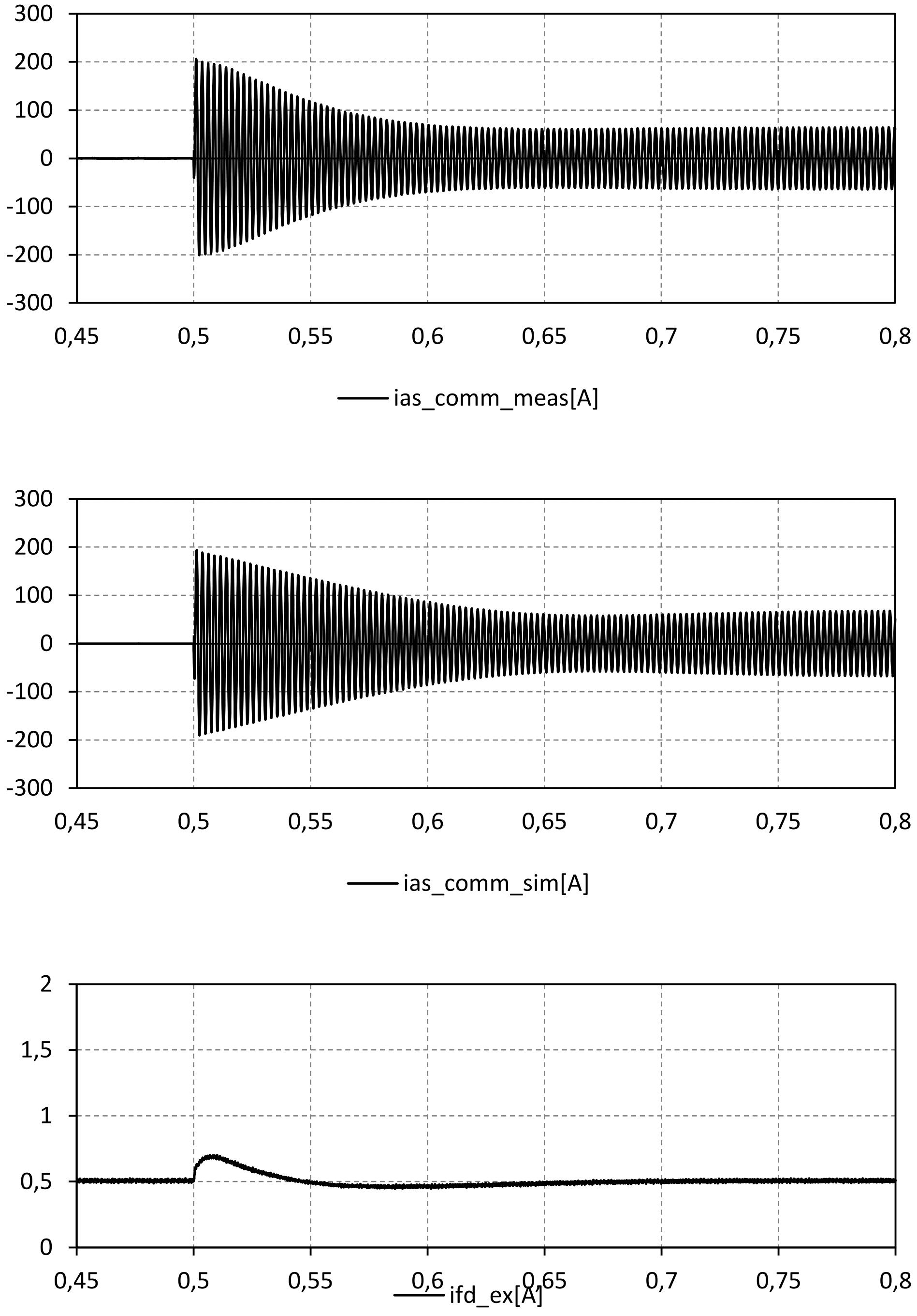

Figure 8.14 Waveform of current – transient state at load for the commercial GT40PCz8:
ias_comm_meas – measured armature line current,
ias_comm_sim – simulated armature line current,
ifd_ex – measured excitation current used in simulation

Table 8.11 Parameters of voltage for load in transient state for commercial GT40PCz8

Parameter	Measurement	Simulation	Difference
RMS value of voltage before load connection (in steady state)	120 V	120 V	0%
RMS value of voltage after load connection (in steady state)	38 V	39 V	3%

Table 8.12 Parameters of load connection current in transient state for commercial GT40PCz8 BSG.

Parameter	Measurement	Simulation	Difference
Maximum value of current in transient state	206 A	194 A	6%
RMS value of current after load connection (in steady state)	46 A	48 A	4%

In the load connection transient state an impedance load described in section 8.4.1 was applied. The maximum value of current in simulation is 6% off form the measured value and in steady state the simulated current RMS value is 4% off from measured value (figure 8.14).

8.6.2 CONDUCTED TESTS FOR PROTOTYPE BSG

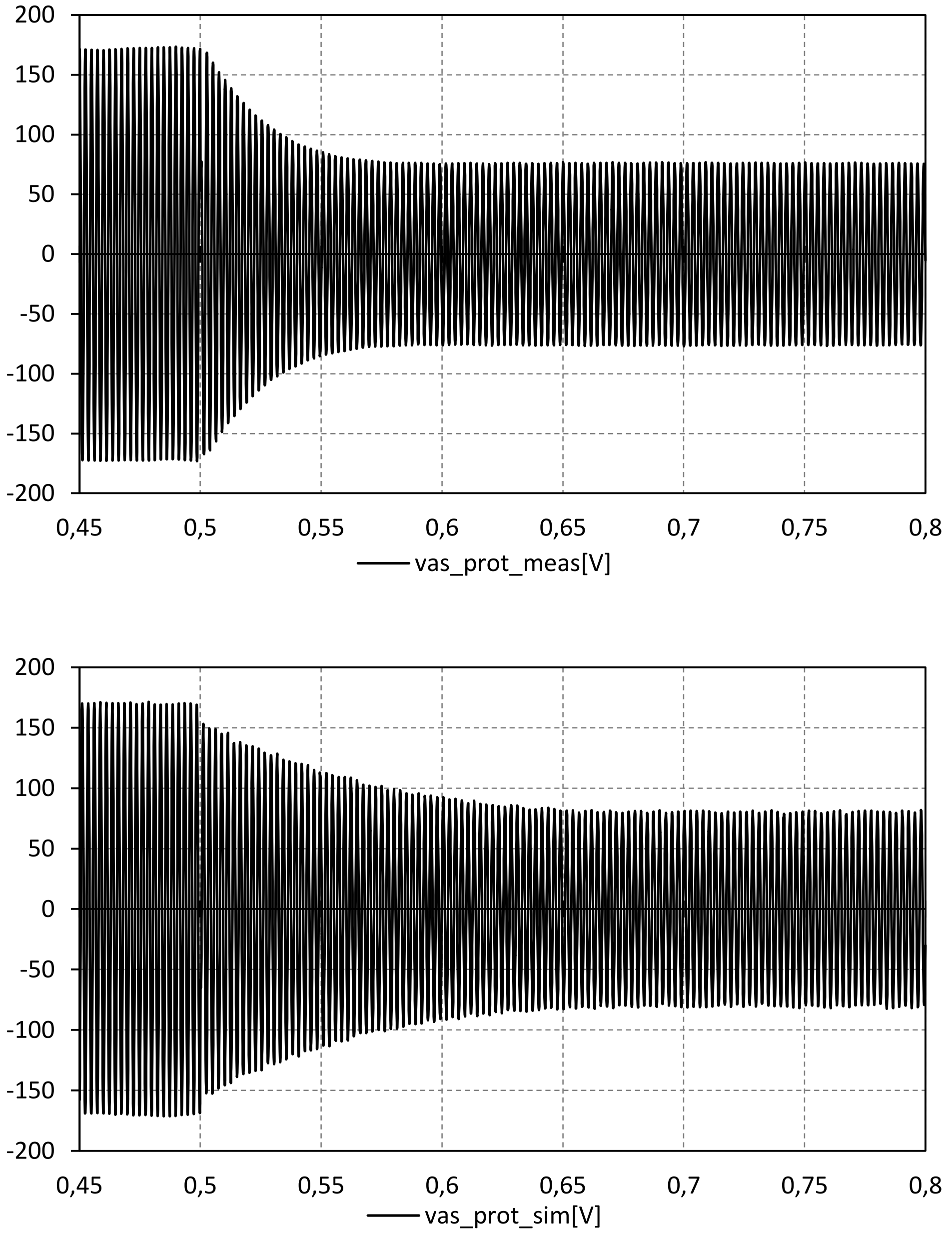

Figure 8.15 Waveform voltage – transient state at load for the prototype BSG: vas_prot_meas – measured armature phase voltage, vas_prot_sim – simulated armature phase voltage

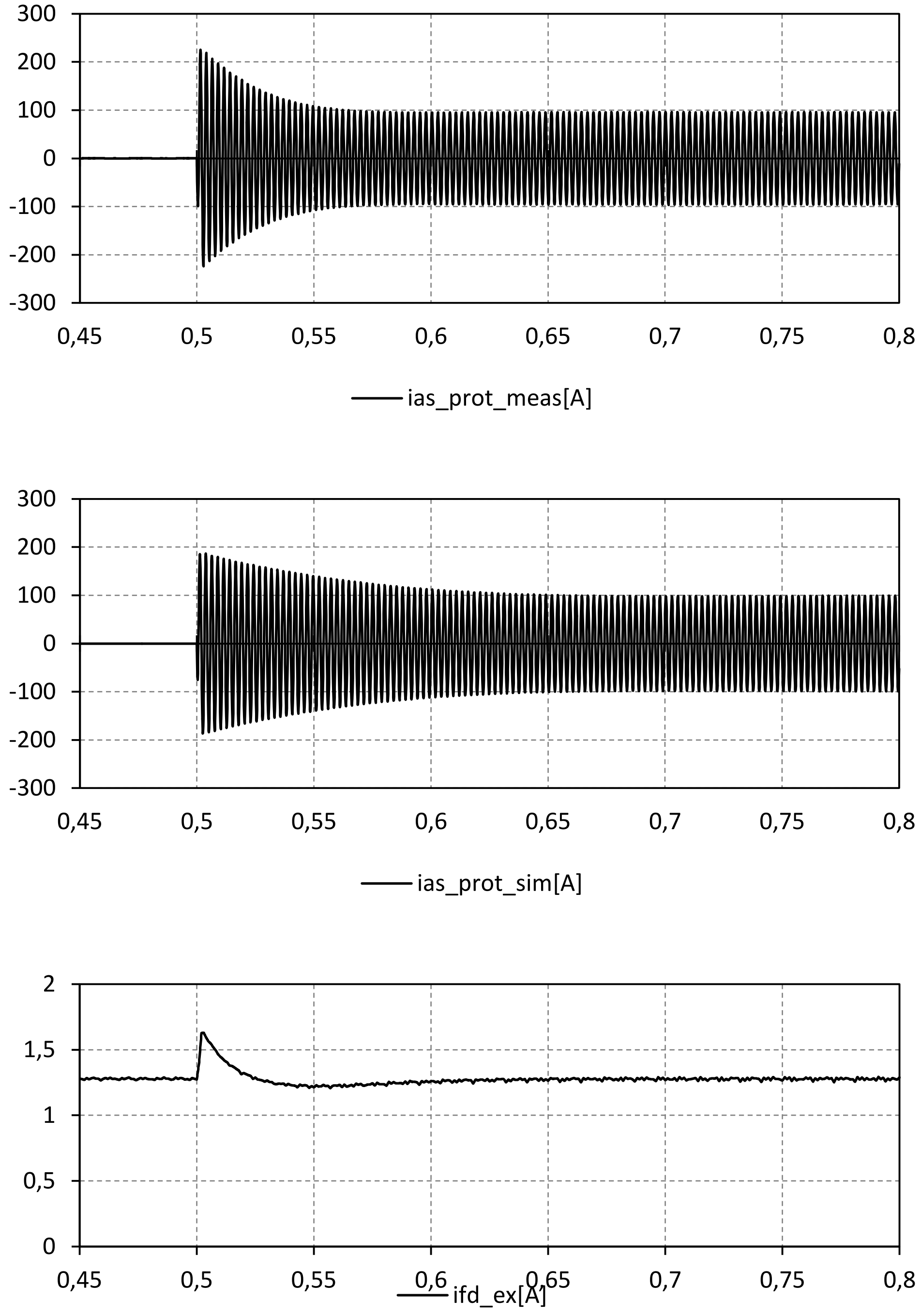

Figure 8.16 Waveform current – transient state at load for the prototype BSG: ias_prot_meas – measured armature line current, ias_prot_sim – simulated armature line current, ifd_ex – measured excitation current used in simulation

Table 8.13 Parameters of voltage at load in transient state for prototype BSG

Parameter	Measurement	Simulation	Difference
RMS value of voltage before load connection (in steady state)	120 V	120 V	0%
RMS value of voltage after load connection (in steady state)	54 V	57 V	6%

Table 8.14 Parameters of load connection current in transient state for prototype BSG.

Parameter	Measurement	Simulation	Difference
Maximum value of current in transient state	226 A	187 A	17%
RMS value of current after load connection (in steady state)	68 A	70 A	3%

In the load switching on transient state an impedance load described in section 8.4.2 was applied. The maximum value of current in simulation is 17% off form the measured value and in steady state the simulated current RMS value is 3% off from measured value (figure 8.16). In this test also clearly observable is the difference in time constant of the transient state. As in short circuit test the simplification made in model damper cage winding can explain the difference.

8.7 SUMMARY

Presented in this chapter simulation and measurement results show differences for the prototype and commercial GT40PCz8 generators. Higher time harmonic voltage and current waveform are present for the commercial BSG – only 5’th harmonic apart from the fundamental component is greater the then 1% of fundamental component. However this value is still relatively small (<2%) and does not show the full potential of presented model.

We can observe that the simulations and measurements results are similar especially for steady states. For higher accuracy for transient states the different structure of the BSG model has to be used. More accurate representation of the damper cage winding is required.

It should be noted that even though an insufficient accuracy occurs, this may be not due to simulation errors but due to the inadequate and incorrect data, necessary for model building and testing.

A comparison between the simulation and empirical results has been carried out to prove that the developed models of the considered BSGs have sufficient accuracy for studying AEPS, particularly for more extensive harmonic analysis.

9 CONCLUSIONS

The thesis formulated in chapter 1 has been proven using analytical, simulation and experimental research approach. Other more important results of the work can be summarised as following:

- simple geometry and windings physical layout have been used for inductance calculations of a salient-pole and cylindrical-rotor BSGs;
- winding function approach has been modified and expressed in general form to take into account the MMF space harmonics for developing expressions for self- and mutual inductance calculations;
- BSG equations in terms of machine variables have been formulated using the simplified machine geometry and windings physical layout;
- developed nonlinear behaviour model of the BSG exhibit a network with the same number of external terminals/ports as the real machine, and represents its behaviour in terms of the electrical (stator and rotor windings) and mechanical (shaft) variables as well;
- main advantage of the developed BSG models is the easy description of AEPS in terms of its topology, and thus providing effective analysis of the steady state and transient states, both for normal and fault operations;
- developed BSG models can be used to determine the voltage and currents of AEPS for more extensive harmonic analysis;
- prototype BSG has been designed and built;
- BSG test bench has been designed and built;
- experimental analysis has been carried out on the two machines: commercially manufactured salient pole BSG (type GT40PCz8), and prototype cylindrical-rotor BSG.

APPENDIX A

The commercially manufactured BSG of the type GT40PCz8 data are presented on figure A.1 and figure A.2.

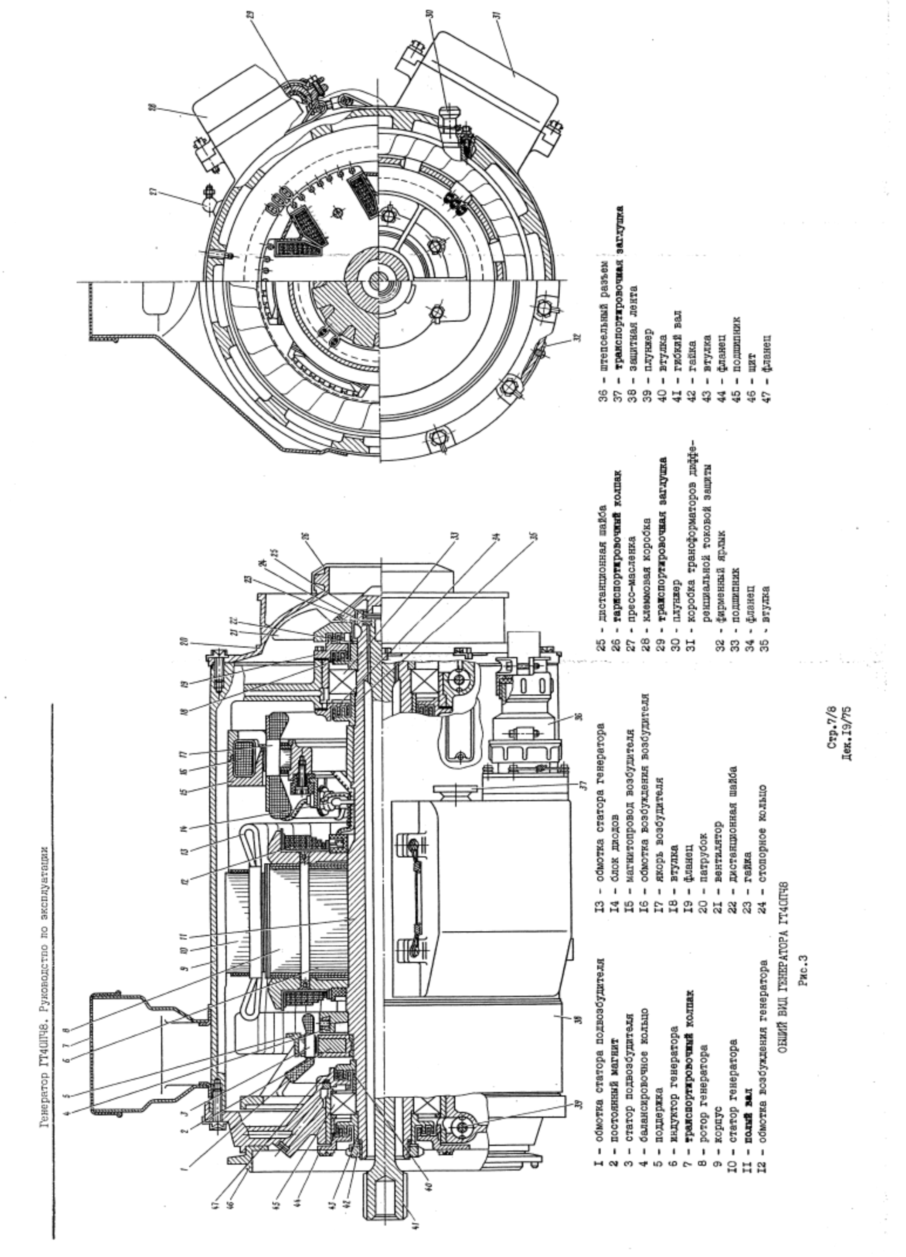

Генератор ГТ40ПЧ8. Руководство по эксплуатации

I - обмотка статора подвозбудителя
2 - **постоянный магнит**
3 - статор подвозбудителя
4 - балансировочное кольцо
5 - поддержка
6 - индуктор генератора
7 - **транспортировочный колпак**
8 - ротор генератора
9 - корпус
I0 - статор генератора
II - **полый вал**
I2 - обмотка возбуждения генератора
I3 - обмотка статора генератора
I4 - блок диодов
I5 - магнитопровод возбудителя
I6 - обмотка возбуждения возбудителя
I7 - якорь возбудителя
I8 - втулка
I9 - фланец
20 - патрубок
2I - вентилятор
22 - дистанционная шайба
23 - гайка
24 - стопорное кольцо
25 - дистанционная шайба
26 - **тарнспортировочный колпак**
27 - пресс-масленка
28 - клеммовая коробка
29 - **транспортировочная заглушка**
30 - плунжер
3I - коробка трансформаторов дифференциальной токовой защиты
32 - фирменный ярлык
33 - подшипник
34 - фланец
35 - втулка
36 - штепсельный разъем
37 - **транспортировочная заглушка**
38 - защитная лента
39 - плунжер
40 - втулка
4I - гибкий вал
42 - гайка
43 - втулка
44 - фланец
45 - подшипник
46 - щит
47 - фланец

ОБЩИЙ ВИД ГЕНЕРАТОРА ГТ40ПЧ8

Рис.3

Стр.7/8
Дек.I9/75

Figure A.1 Commercial GT40PCz8 BSG technical data

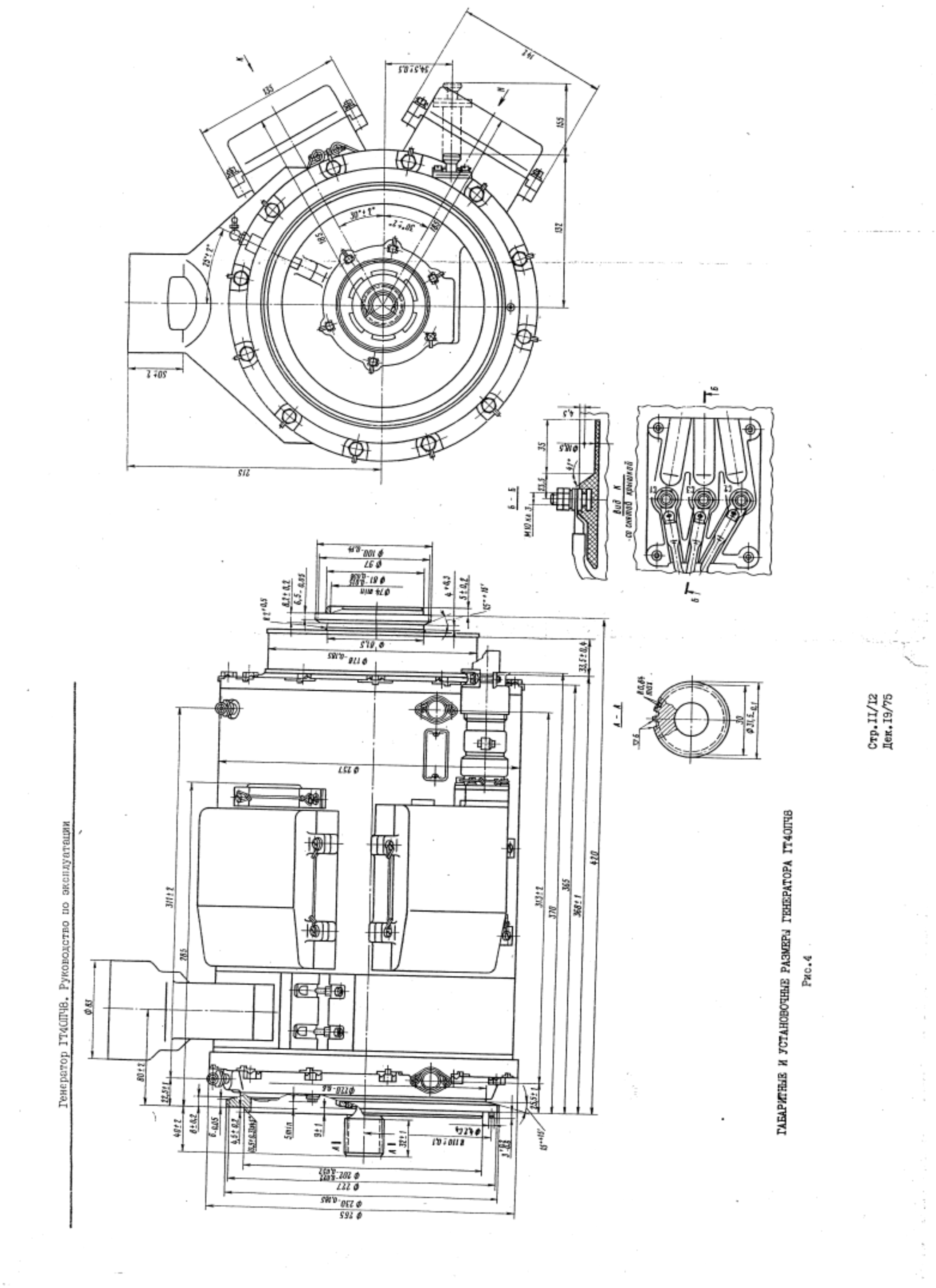

Figure A.2 Commercial GT40PCz8 BSG dimensions

Figure A.3, figure A.4, figure A.5 and figure A.6 shows documentation based on measurements of GT40PCz8 BSG dimensions.

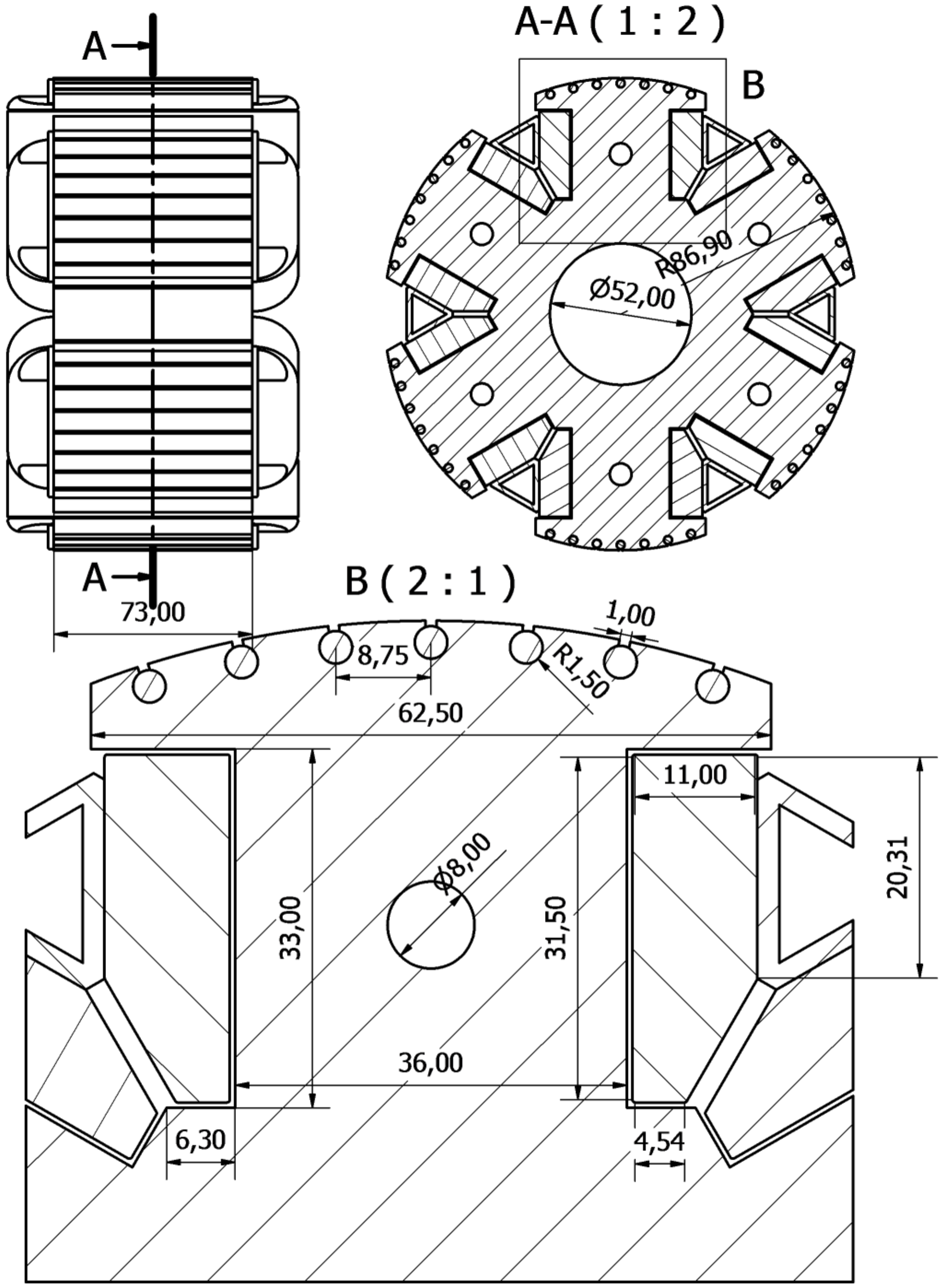

Figure A.3 Commercial GT40PCz8 BSG main generator stage rotor dimensions

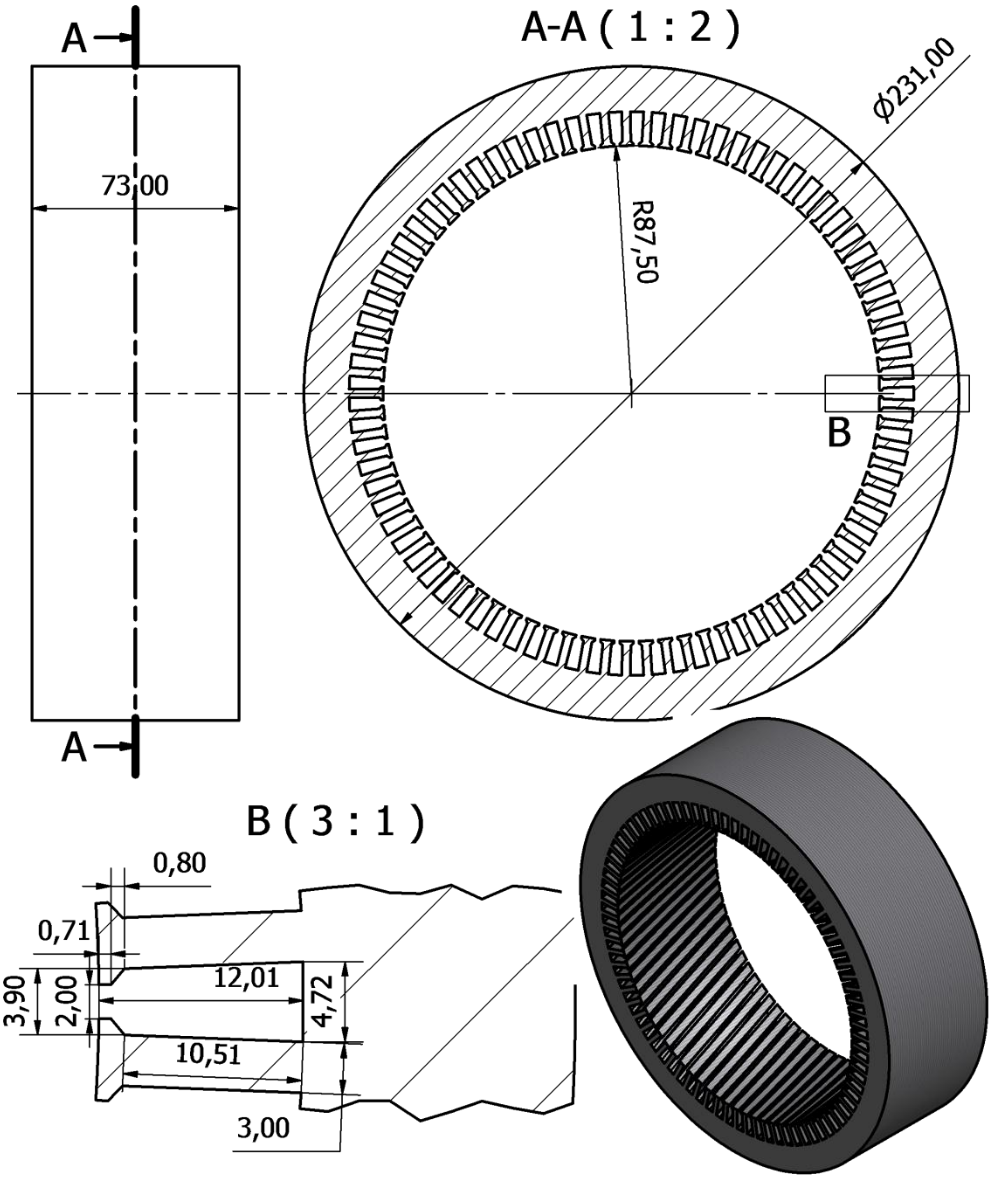

Figure A.4 Commercial GT40PCz8 BSG main generator stator dimensions

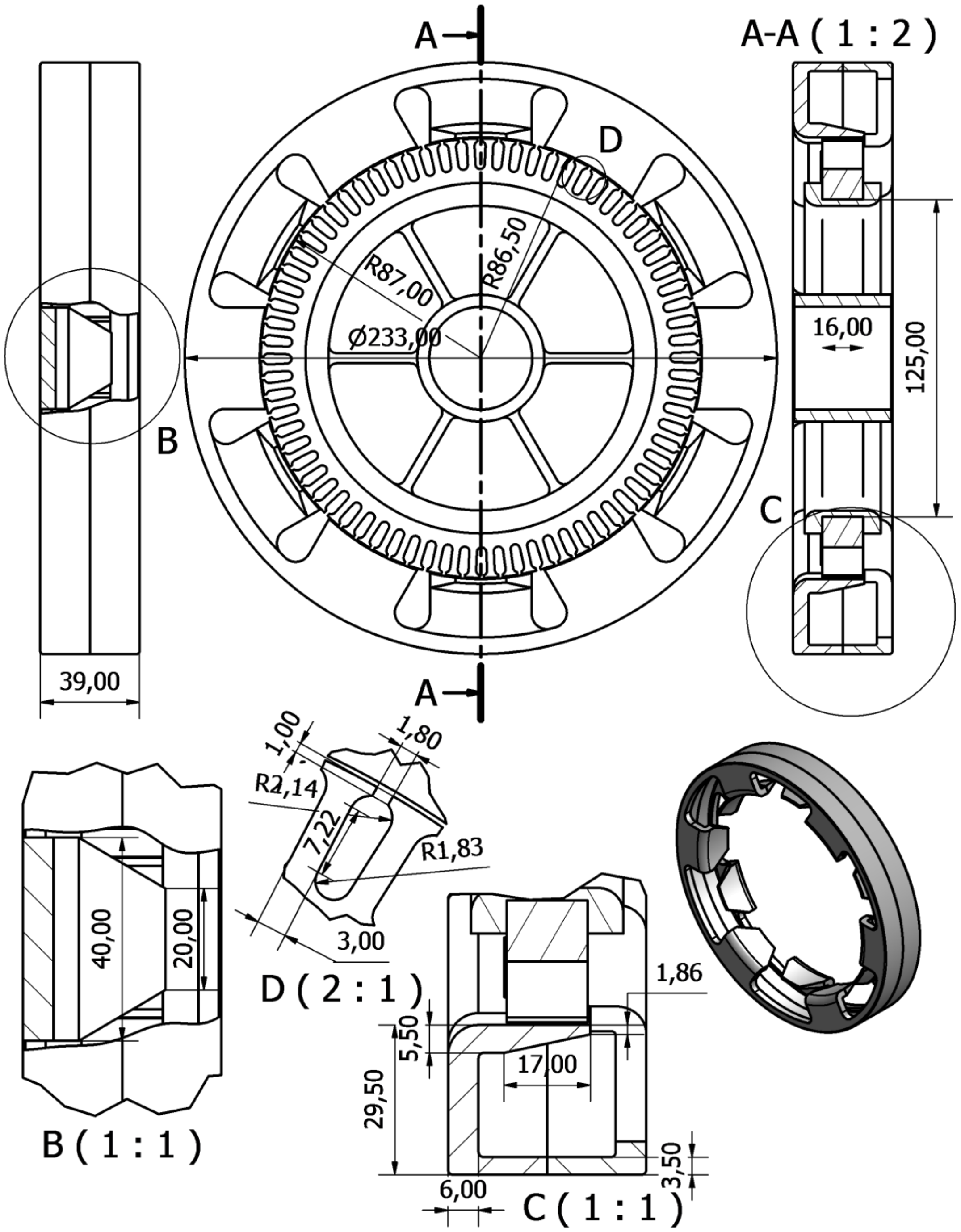

Figure A.5 Commercial GT40PCz8 BSG ac exciter generator dimensions

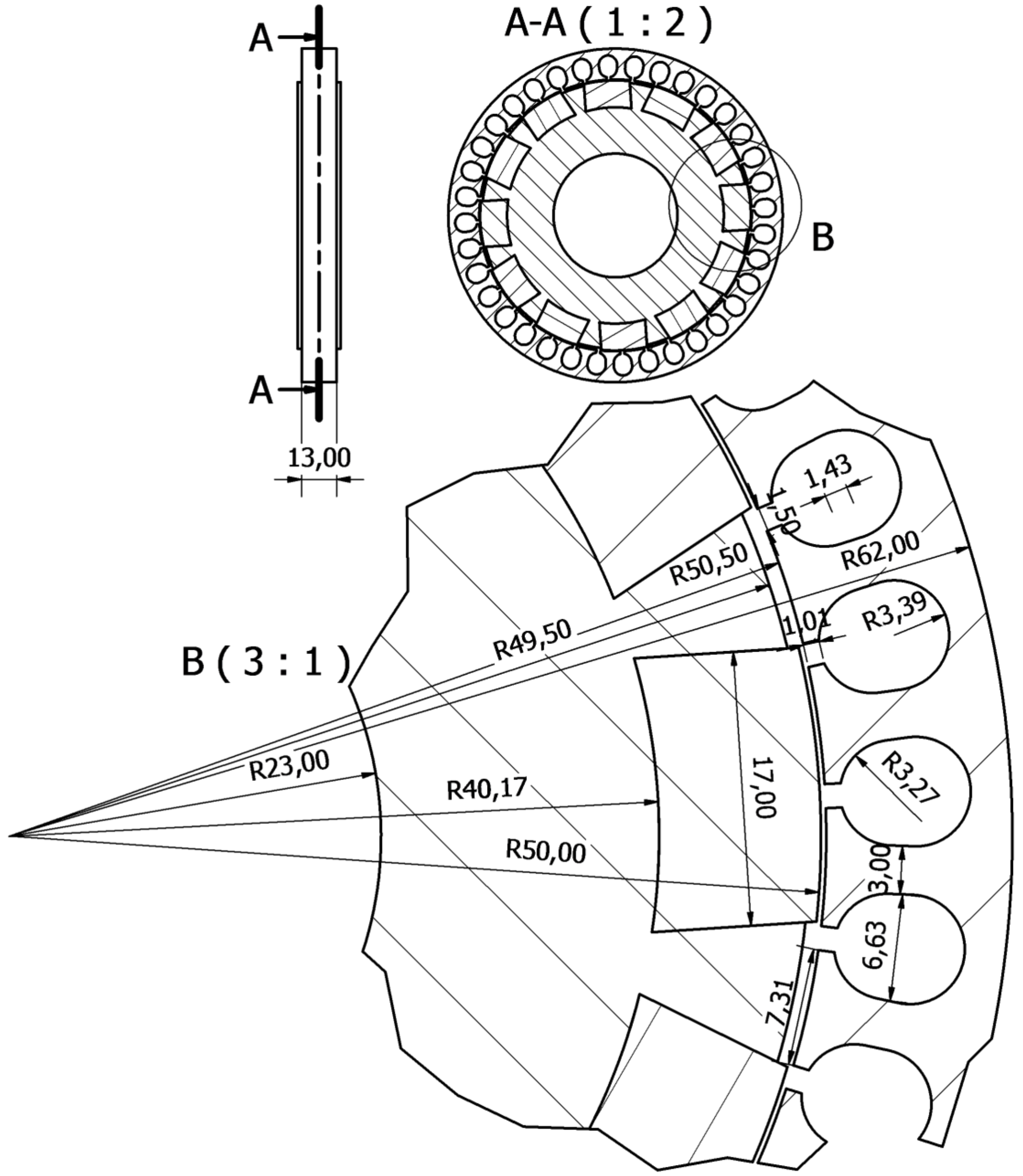

Figure A.6 Commercial GT40PCz8 BSG subexciter dimensions

APPENDIX B

Main generator stage designed process [14,5] was conducted based on assumption presented in table B.1:

Table B.1 Assumptions for main generator stage design process:

Parameter	Value	Description
S_n	40kVA	nominal power
U_s	208V	nominal voltage
I_s	111A	nominal current
f_n	400Hz	nominal frequency
$\cos\varphi_n$	0.8	nominal load power factor
I_{fn}	45A	nominal field winding current
p	3	number of pole pairs
m	3	number of phases
Q_s	81	number of stator slots
Q_r	66	number of rotor slots (including cage slots in wide teeth) – parameters of the prototype BSG
N_s	27	number of armature winding turns
δ	$0.6 \times 10^{-3}\text{m}$	airgap length
D_s	$175 \times 10^{-3}\text{m}$	inner diameter of the stator
l	$73 \times 10^{-3}\text{m}$	machine length
b_1	$2 \times 10^{-3}\text{m}$	stator and rotor slot opening

Above parameters are the parameters of the commercial GT40PCz8 BSG. Based on them the calculation of new parameters were carried out.

The effective core length is:

$$l' = l + 2\delta = (73 + 2 \times 0.6) \times 10^{-3} = 74.2 \times 10^{-3} m \tag{B.1}$$

and the machine pole pitch is:

$$\tau_p = \frac{\pi D}{2\,p} = \frac{\pi\ 0.1744}{6} = 91.3 \times 10^{-3} m \tag{B.2}$$

$$t_p = 81/2p = 13.5 \text{ slots} \tag{B.3}$$

where diameter D is in the middle of the airgap.

In order to calculate the magnitude of the flux density in the airgap the armature winding factor needs to be established and the armature winding distribution factor is:

$$\mathrm{k}_{dv}=\frac{\sin v\,\dfrac{q\alpha_u}{2}}{q\ \sin v\ \dfrac{\alpha_u}{2}}\qquad \mathrm{k}_{d1}=0.957\qquad \text{(B.4)}$$

where: $v -$ harmonic number, $\alpha_u = p \times 360/81 = 13.3(3)° = 0.2327\,rad$ – stator slot angle

The pitch factor is:

$$\mathrm{k}_{pv}=\sin\left(v\frac{W}{t_p}\frac{\pi}{2}\right)\qquad \mathrm{k}_{p1}=0.866\qquad \text{(B.5)}$$

Where coil span $\mathrm{W}=9$ slots

The skewing factor is:

$$\mathrm{k}_{sqv}=\frac{\sin\left(v\dfrac{s}{\tau_p}\dfrac{\pi}{2}\right)}{v\dfrac{s}{\tau_p}\dfrac{\pi}{2}}\qquad \mathrm{k}_{sq1}=0.998\qquad \text{(B.6)}$$

Where s is the skewing (length)

Winding factor:

$$\mathrm{k}_{wv}=\mathrm{k}_{dv}\cdot\mathrm{k}_{pv}\cdot\mathrm{k}_{sqv}\qquad \mathrm{k}_{w1}=0.827\qquad \text{(B.7)}$$

Figure B.1 shows phasor diagram for armature winding (one pole pair) and based on it the winding factor (excluding skewing factor) is $\mathrm{k}_{w1}=0.827$

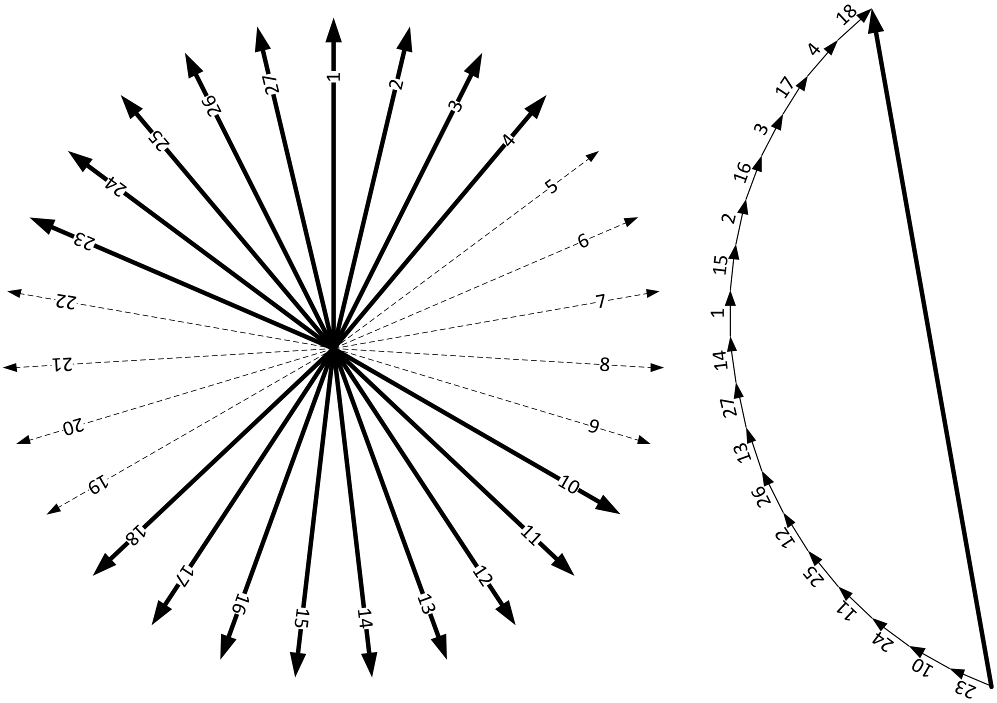

Figure B.1 Phasor diagram for main generator stage of BSG armature winding (1/3 of machine).

Assuming sinusoidal distribution of flux density in the airgap ($\alpha_i = \frac{2}{\pi}$) the magnitude of it is:

$$\hat{B}_\delta = \frac{\sqrt{2}\frac{(1.04U_s)}{\sqrt{3}}}{2\pi f_n \mathrm{k}_{w1}\alpha_i N_s \tau_p l'}$$

$$\hat{B}_\delta = \frac{\sqrt{2}\frac{(1.04 \times 208)}{\sqrt{3}}}{2\pi 400 \times 0.827 \times \frac{2}{\pi} \times 27 \times 91.3 \times 74.2 \times 10^{-6}} = 0.73T \tag{B.8}$$

And the peak value of the airgap flux is:

$$\hat{\Phi}_m = \frac{2}{\pi}\hat{B}_{\delta 1}\tau_p l' = 3.15 \times 10^{-3} V\, s \tag{B.9}$$

The stator slot pitch it:

$$\tau_{us} = \frac{2\,\pi\,\frac{D_s}{2}}{Q_s}$$

$$\tau_{us} = \frac{2\,\pi\,\frac{175\times10^{-3}}{2}}{81} = 6.8\times10^{-3}m \tag{B.10}$$

The rotor slot pitch it:

$$\tau_{ur} = \frac{2\,\pi\,\frac{(D_s+2\delta)}{2}}{Q_r}$$

$$\tau_{ur} = \frac{2\,\pi\,\frac{(175+2\times0.6)\times10^{-3}}{2}}{66} = 8.3\times10^{-3}m \tag{B.11}$$

The equivalent stator slot opening is:

$$b_e = \kappa b_1 \tag{B.12}$$

where:

$$\kappa = \frac{2}{\pi}\left[\tan^{-1}\frac{b_1}{2\delta} - \frac{2\delta}{b_1}\ln\sqrt{1+\left(\frac{b_1}{2\delta}\right)^2}\right] = 0.4 \tag{B.13}$$

The Carter factor for stator slots is:

$$k_{Cs} = \frac{\tau_{us}}{\tau_{us}-b_e} \qquad k_{Cs} = \frac{6.8}{6.8-0.8} = 1.13 \tag{B.14}$$

The Carter factor for rotor slots is:

$$k_{Cr} = \frac{\tau_{ur}}{\tau_{ur}-b_e} \qquad k_{Cr} = \frac{8.3}{8.3-0.8} = 1.11 \tag{B.15}$$

Effective airgap length is:

$$\delta_e = k_{Cs}k_{Cr}\delta \qquad \delta_e = 1.13\times1.11\times0.6\times10^{-3} = 0.75\times10^{-3}\mathrm{m} \tag{B.16}$$

Neglecting saturation and assuming that entire magnetic circuit voltage is in the airgap the main inductance of the machine can be defined as:

$$L_{md} = \frac{m}{2}\frac{2}{\pi}\mu_0 \frac{1}{2}\frac{1}{p}\frac{4}{\pi}\frac{\tau_p}{\delta_e} l'(k_{w1}N_s)^2$$

$$L_{md} = 4\pi \times 10^{-7} \frac{6 \times 91.3}{3\ \pi^2 0.75} 74.2 \times 10^{-3}\ (0.827 \times 27)^2 = 1.14mH \tag{B.17}$$

Assuming the leakage flux is not more the 10% of the main flux the synchronous reactance in direct axis is:

$$X_d = 2\,\pi\, f_n\ 1.1\ L_{md} \qquad X_d = 2\,\pi\ 400\ 1.1\ 1.14 \times 10^{-3} = 3.15\Omega \tag{B.18}$$

In nominal load conditions the machine EMF amplitude is:

$$\hat{E}_0 = \sqrt{\left(\frac{\sqrt{2}U_s}{\sqrt{3}} + X_d\sqrt{2}I_s \sin\varphi\right)^2 + \left(X_d\sqrt{2}I_s\cos\varphi\right)^2}$$

$$\hat{E}_0 = \sqrt{\left(\frac{\sqrt{2}\ 208}{\sqrt{3}} + 3.15 \times \sqrt{2} \times 111 \times 0.6\right)^2 + \left(3.15 \times \sqrt{2} \times 111 \times 0.8\right)^2} = 612V \tag{B.19}$$

Current linkage required to achieve $\hat{E}_0$ EMF is:

$$\Theta_f = \Theta_e - \Theta_{s1} \tag{B.20}$$

Where the Θ_{s1} is stator current linkage and Θ_e is a current linkage resulting from the filed winding action and armature reaction and responsible for achieving nominal voltage on the machine terminals. The Θ_e current linkage is defined as field winding in no load conditions and is:

$$\Theta_e = \frac{\hat{B}_\delta \delta_e}{\mu_0} \qquad \Theta_e = \frac{0.73 \times 0.75 \times 10^{-3}}{4\pi \times 10^{-7}} = 436\ A \tag{B.21}$$

Stator current linkage for nominal current is:

$$\Theta_{\mathrm{sv}} = \frac{\mathrm{m}}{2}\frac{4}{\pi}\frac{\mathrm{k_{wv}N_s}}{\mathrm{p\upsilon}}\frac{1}{2}\sqrt{2}I_s \qquad \Theta_{s1} = \frac{3}{\pi}\frac{27 \cdot 0.827}{3}\sqrt{2} \cdot 111 = 1\ 116\ A \tag{B.22}$$

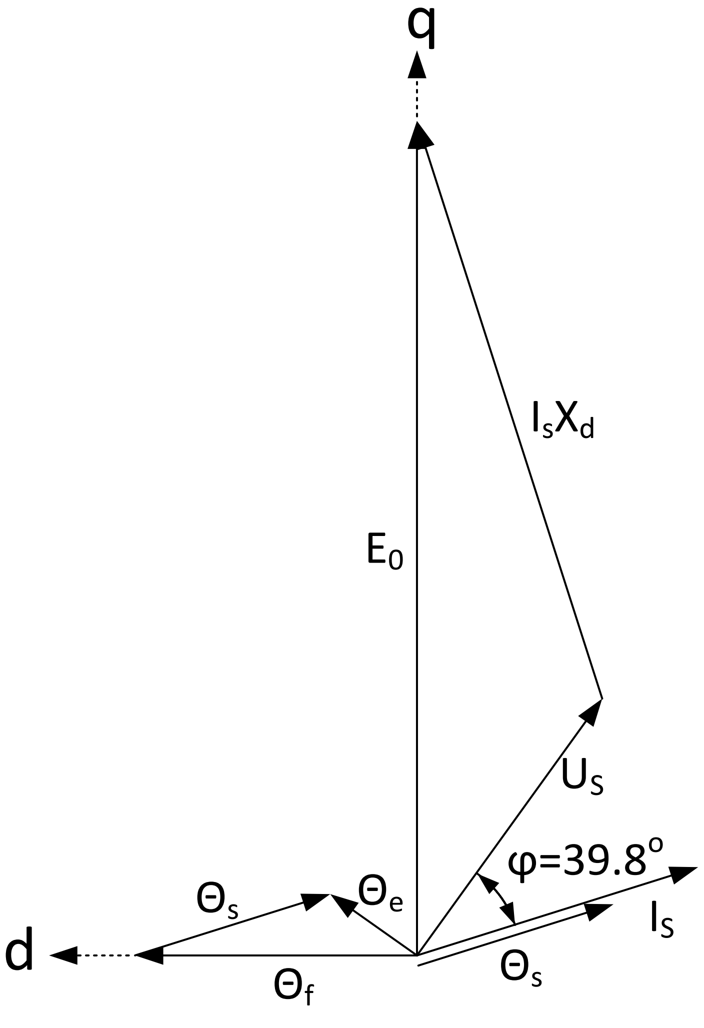

Figure B.2 Designed BSG nominal load vector simplified diagram

And as in (B.21) the current linkage required to achieve $\hat{E}_0$based on figure B.2 is:

$$\Theta_f = \Theta_e - \Theta_{s1} = 1421\ A \tag{B.23}$$

Number of rotor wining turns (one pole) is:

$$\mathrm{N}_{fp} = \frac{\Theta_f}{I_f} \qquad \mathrm{N}_{fp} = \frac{1421}{45} = 32 \tag{B.24}$$

However the commercial GT40PCz8 BSG had 42 turns per pole and the newly design main generator stage should have similar number of turns to allow over-excitation. The designed main generator stage dimensions are presented on figure B.3.

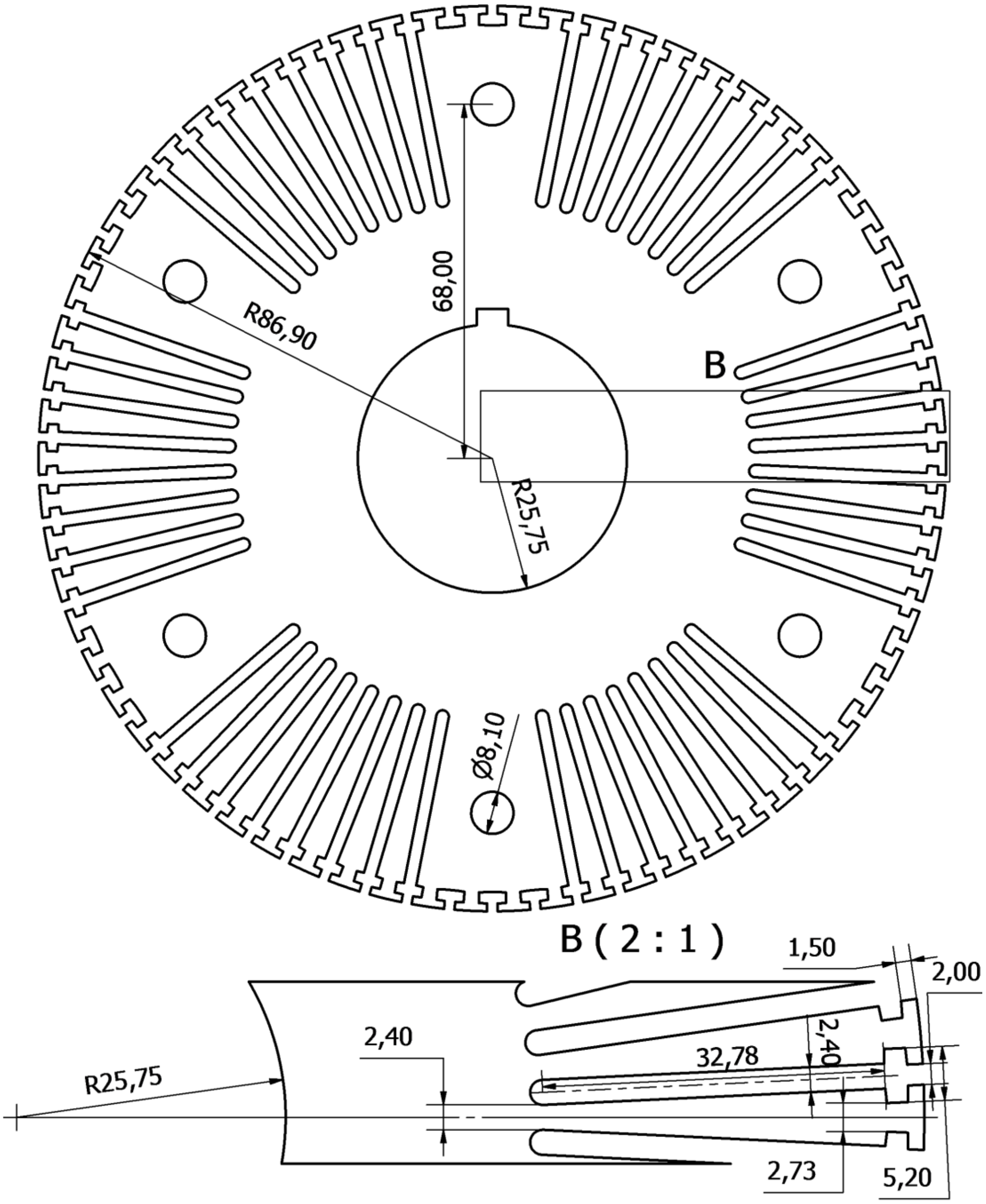

Figure B.3 Dimensions of designed main generator stage rotor

Rotor slot height is $32.78mm$ (part of slot where conductors are), and it has width of $2.4mm$. And the dimensions of filed winding copper conductor are $3 \times 1.5mm$. The maximum number of coils in one pair of slots is 10. Because we assume 8 slots per pole and equal number of turns per coil the number of turns per pole is $\mathrm{N}_{fp} = 40$. And the number of rotor winding turns is:

$$N_f = 2\,p\,N_{fp} \qquad\qquad N_f = 2 \times 3 \times 40 = 240 \qquad \text{(B.25)}$$

APPENDIX C

FEM simulations were conducted using FLUX2D software. In other to conduct transient simulation needed for verification of assumed parameters a circuit model was build (figure C.1). In this model for each armature winding two coils are defined (1/3 of machine): B11 and B21 for first phase, B12 and B22 for second phase and B13 and B23 for third phase. The B_ROTOR_1 and B_ROTOR_2 are coil conductors defined tor excitation winding (2 poles). The R1 to R3, RP1 to RP3 and L1 to L3 represent load. The M1_1 to M1_3 and M2_1 to M2_3 represent damper cage bars (three for each pole), the resistors R4 to R11 represent the connection of the cage bars. The I1 is the field current source.

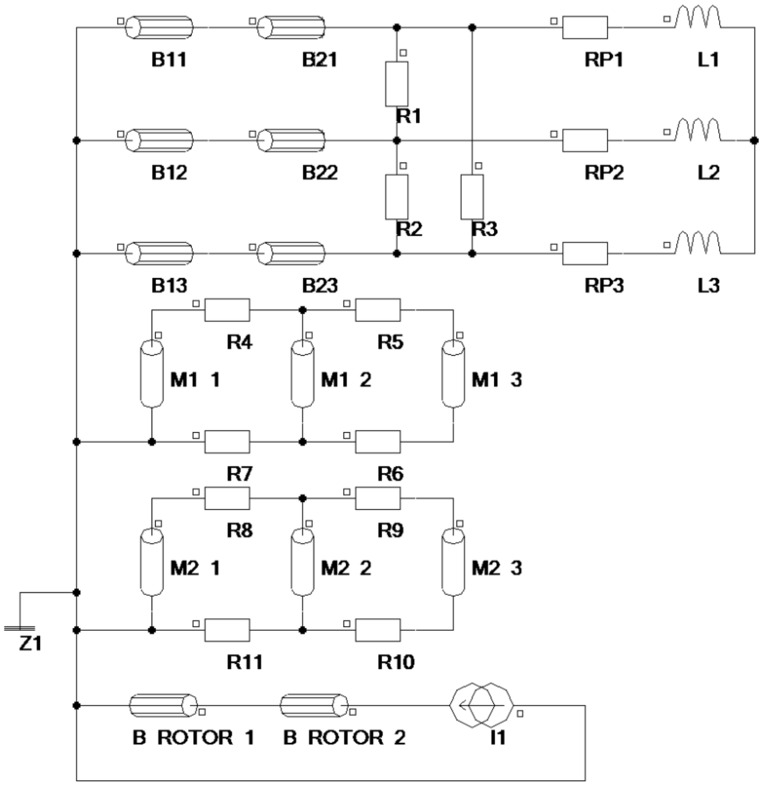

Figure C.1 Circuit model for the main generator stage FEM simulations

The conducted transient test allow to verify the designer generator assumed parameters and dimensions. The test were conducted in no load and 50% of nominal load conditions (respectively figure C.2 and figure C.3).

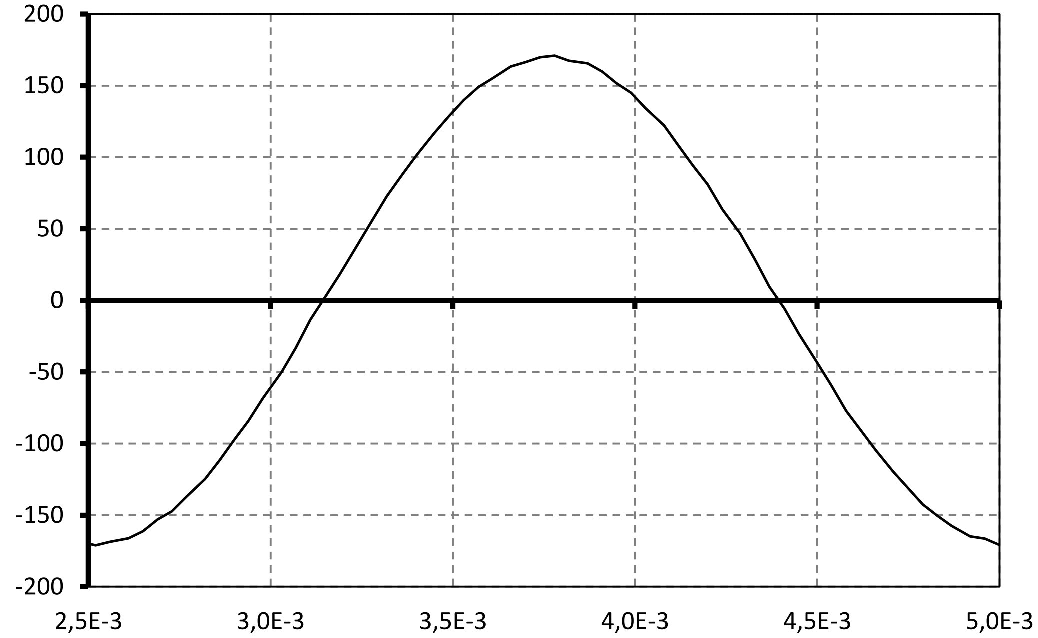

Figure C.2 Developed main generator stage FEM transient simulation result – no load EMF

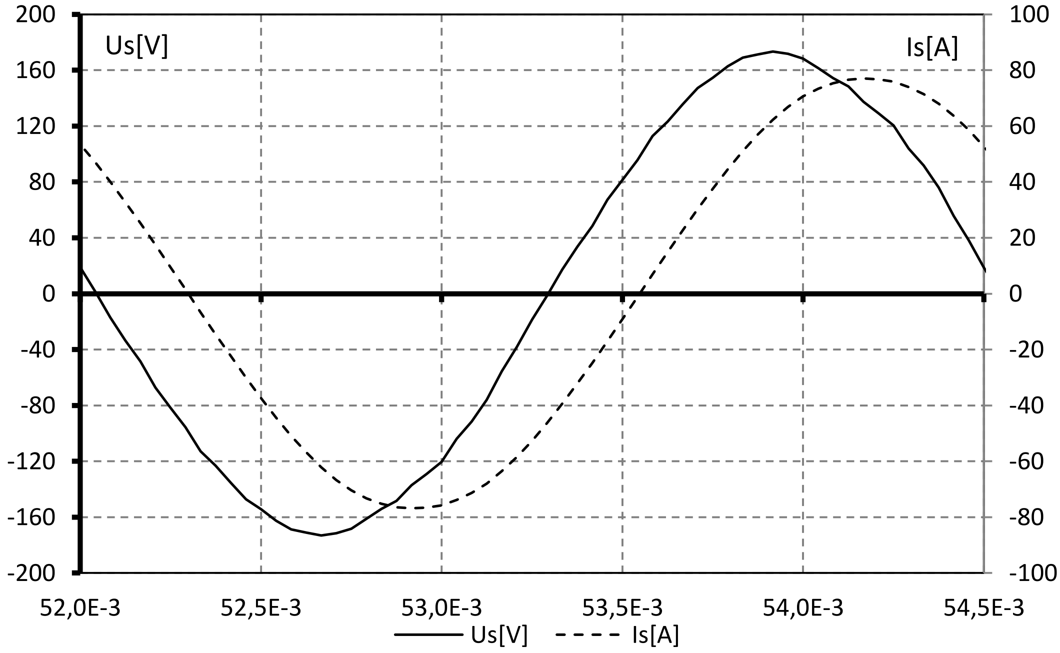

Figure C.3 Developed main generator stage FEM transient simulation result – 50% nominal load armature phase voltage and line current (RP1, RP2, RP3 = 1.727 ohm, L1, L2, L3 = 515 µH, PF=0.8)

APPENDIX D

MAST language model with parameters of the commercial GT40PCz8:

Table D.1 Parameters and variables of the model:

Parameter/Variable	Description
ifd	Main generator field current
ifd_ex	Exciter field current
ias, ibs, ics	Armature current
ifd, ikd, ikq	Rotor currents (field and damper in d and q axes)
vas, vbs, vcs	Armature phase voltages
vfd_ex	Exciter field voltage
Rs	Armature winding resistance
Rex	Exciter field winding resistance
Rkd, Rkq	Rotor damper winding resistances (d and q axes)
phi	Prefix denotes linkage fluxes
Te	Electromagnetic torque
Tl	Load torque
visc	Torque due to friction
mom	Inertia torque
Jw	Rotor inertia
wm	Mechanical rotation speed
alpha	Mechanical rotor angle

The model was implemented with language MAST and tested with the Synopsys/Saber simulator. The MAST file contains the following items:

template *header* *model parameters*

- *And declaration of types and connection points (electrical, rotational, thermal, hydraulic ..) and of the arguments.*
- *Template body: it begins with an opening brace { and ends with a closing brace }.*

{ *local declarations: declare the local parameters, variables and branches that appear in the rest of the template.*

- *Parameter section: causes the simulator to perform one-time calculations after reading the netlist.*

parameters { *parameter assignments and argument testing* **}**

- *netlist components*

values { *value assignments* **}**

Control section: it is a declaration section, although it can contain if-else statements whose conditions are based on constant parameter expressions..

control_section { *simulator-dependent control statements for non-linearities* **}**

- *Equations: Contain the terminal equations of the model.*

equations { *equations describing behaviour* **}**

}

```
#----------------------------------------------------------------------------
template bsg_main_generator_gut_beh_issue2_abcmachine va_p vb_p vc_p va_m vb_m vc_m vf_p vf_m rotor_p rotor_m =
        Lmd, Lsfd, Lskd, Lskq, Lmfd, Lmkd, Lmkq, Lfdkd,
        Lls, Llfd, Llkd, Llkq,
        Rs, Rfd, Rkq, Rkd, Rex, p, fe, Bm, Jw, ic_alpha, k_iex,
        sat_include, sat_file, sat_interp, sat_extrap, sat_density, sat_rpm,
        check, harm
#----------------------------------------------------------------------------
#
# Header
#
#----------------------------------------------------------------------------
# Connection pins declaration
#----------------------------------------------------------------------------
electrical     va_p, vb_p, vc_p, va_m, vb_m, vc_m
electrical     vf_p, vf_m
rotational_vel rotor_p, rotor_m
#----------------------------------------------------------------------------
# Parameters declaration
#----------------------------------------------------------------------------
number Lmd=571.9E-6
number Lls=35.0E-6
number Lsfd=2.04E-3
number Lskd=381E-6
number Lskq=381E-6
number Lmfd=11E-3
number Lmkd=381E-9
number Lmkq=381E-9
number Lfdkd=2.04E-3
number Llfd=834E-6
number Llkd=55E-6
number Llkq=80E-6

number Rs=0.022
number Rfd=0.31
number Rkq=1
number Rkd=50u

number Rex=4.71
number k_iex=31.6

number p=3
number fe=400
number Bm=1m
number Jw=0.01
#----------------------------------------- saturation curve parameters
enum {yes,no} sat_include = no
string sat_file="no_load_voltage.ai_dat"
number sat_interp=0
number sat_extrap[2]=[1,1]
```

```
number sat_density=100
number sat_rpm=8000
#---------------------------------------- initial conditions
number ic_alpha=0
#----------------------------------------
enum {yes, no} check = no       # User diagnostic switch for observing entered and
                                # calculated parameters
struc {
   enum {yes, no} include = yes
   number  As3h=0.006          #[-] 3rd harmonic stator MMF relative value
   number  As5h=0.000          #[-] 5th harmonic stator MMF relative value
   number  Afd3h=0.240         #[-] 3rd harmonic field MMF relative value
   number  Afd5h=0.000         #[-] 5th harmonic field MMF relative value
   number  Akd3h=0            #[-] 3rd harmonic d-axis kage MMF relative value
   number  Akd5h=0            #[-] 5th harmonic d-axis kage MMF relative value
   number  Akq3h=0            #[-] 3rd harmonic q-axis kage MMF relative value
   number  Akq5h=0            #[-] 5th harmonic q-axis kage MMF relative value
   number  a1h=-1.04          #[-] average valu of airgap length relative value
   number  a2h=0.23           #[-] first harmonic of airgap length relative value
   } harm
#-------------------------------------------------------------------------
#
# Beginning of the template
#
#-------------------------------------------------------------------------
{
<consts.sin                  # constants used in mathematical calculations
   #-------------------------------------------------------------------------
   # Constant values and coefficients
   #-------------------------------------------------------------------------
   number ang                #[rad] phase shift
   number kfd               #[-] field winding to stator ratio (2/3*Nfd/Ns)
   number kkd
   number kkq
   number deg_to_rad         #[-] degrees to radians
   number Ls                #[-] aramture self inductance

   #-------------------------------------------------------------------------
   # Saturation curve parameters
   #-------------------------------------------------------------------------
   foreign tlu
   number  datap[*],sp1[*]    # data points and sample points of no-load curve
   val nu Ksat              #[-] saturation coefficient
   val v vsat              #[V] saturation voltage
   val v v_rem              #[V] remanence voltage
   val i ifrem             #[A] current modeling PM for remanence voltage
   val l Lmsat              #[H] saturation inductance

   var i ifd
   #-------------------------------------------------------------------------
   # Poliharmonic amplitydes
   #-------------------------------------------------------------------------
   number As3, Afd3, Akd3, Akq3, a1h, a2h
   number As5, Afd5, Akd5, Akq5
   #-------------------------------------------------------------------------
   # Model inductances
   #-------------------------------------------------------------------------
   val l L_as_as, L_bs_bs, L_cs_cs, L_as_bs, L_as_cs, L_bs_cs
   val l L_fd_fd, L_kd_kd, L_kq_kq, L_fd_kd, L_fd_kq, L_kd_kq
   val l L_as_fd, L_bs_fd, L_cs_fd
   val l L_as_kd, L_bs_kd, L_cs_kd
   val l L_as_kq, L_bs_kq, L_cs_kq
   #-------------------------------------------------------------------------
   # Model rotational inductances
   #-------------------------------------------------------------------------
   val l G_as_as, G_bs_bs, G_cs_cs, G_as_bs, G_as_cs, G_bs_cs
   val l G_fd_fd, G_kd_kd, G_kq_kq, G_fd_kd, G_fd_kq, G_kd_kq
   val l G_as_fd, G_bs_fd, G_cs_fd
```

```
  val l G_as_kd, G_bs_kd, G_cs_kd
  val l G_as_kq, G_bs_kq, G_cs_kq
  #---------------------------------------------------------------------------
  # Model parameters
  #---------------------------------------------------------------------------
  number we0                 #[rad/s] synchronous electrical angular velocity

  #---------------------------------------------------------------------------
  # Model variables
  #---------------------------------------------------------------------------
  val w_radps we              #[rad/s] electrical angular velocity

  var ang_rad alpha           #[rad] rotor position angle
  val tq_Nm   Te             #[Nm] electromagnetic torque
  var tq_Nm   mom              #[Nm]
  val tq_Nm   visc           #[Nm] viscous loss

  val f phias, phibs, phics    #[Wb] stator flux linkage
  val f phifd, phikd, phikq    #[Wb] rotor flux linkage
  var i ikd, ikq

  var i im, imd, imq          #[A] magnetising current
  var i iqs, ids, i0s

  #----------------------- # Connections
   branch ias=i(va_m->va_p),     vas=v(va_p,va_m),                 # stator - phase as
        ibs=i(vb_m->vb_p),     vbs=v(vb_p,vb_m),                 # stator - phase bs
        ics=i(vc_m->vc_p),     vcs=v(vc_p,vc_m),                 # stator - phase bs
        ifd_ex=i(vf_p->vf_m),  vfd_ex=v(vf_p,vf_m),              # rotor - field excitation winding
        Tl=tq_Nm(rotor_m->rotor_p), wm=w_radps(rotor_p,rotor_m)    # torque and mechanical angular velocity of the rotor

    struc{number bp,inc;}sp_mech[*]      # sample points definition for mechanical variable
    struc{number bp,inc;}ns_mech[*]      # newton step definition for mechanical variable
    struc{number bp,inc;}sp_em[*]        # sample points definition for electromagnetic variable
    struc{number bp,inc;}ns_em[*]        # newton step definition for electromagnetic variable

#---------------------------------------------------------------------------
# Parameters section
#---------------------------------------------------------------------------
  parameters {
    ang=2*math_pi/3                                   # phase shift
    sp_mech=[(-1meg,1m),(0,1m),(1meg,0)]                    # sample points
    ns_mech=[(-1meg,10m),(0,10m),(1meg,0)]                   # newton step
    #ns_em=[(-1meg,10m),(0,10m),(1meg,0)]                   # newton step
    sp_em=[(-1meg,0.1m),(0,0.1m),(1meg,0)]                  # sample points
    #sp_em=[(-1meg,10u),(-1,1u),(0,1u),(1,10u),(1meg,0)]       # sample points
    #sp_em=[(-1meg,10u),(-1m,1u),(0,1u),(1m,10u),(1meg,0)]   # sample points

    Ls = Lmd*2/3

    kfd = Lsfd/Lmd                   # field winding to stator ratio
    kkd = Lsfd/Lmkd                     # field winding to direct axis kage ratio
    kkq = Lsfd/Lmkq                     # field winding to quadrature axis kage ratio
    deg_to_rad = math_pi/180
    # TLU data pre-processing
    datap=tlu(0,1,sat_file,"",sat_interp,sat_extrap)
    # TLU returns the sample points array for the independent variable
    sp1=tlu(1,addr(datap),1,sat_density)

    we0=2*math_pi*fe

    if (harm->include==yes) {
       As3=harm->As3h
       As5=harm->As5h
       Afd3=harm->Afd3h
       Afd5=harm->Afd5h
       Akd3=harm->Akd3h
       Akd5=harm->Akd5h
```

```
     Akq3=harm->Akq3h
     Akq5=harm->Akq5h
     a1h=harm->a1h
     a2h=harm->a2h
   }
   else {
     As3=1e-6
     As5=1e-6
     Afd3=1e-6
     Afd5=1e-6
     Akd3=1e-6
     Akd5=1e-6
     Akq3=1e-6
     Akq5=1e-6
     a1h=1
     a2h=1e-6
   }

   if (check == yes) {
    message ("-------------------------REPORT")
    message ("-------------------------Model parameter values")
    message ("Stator winding self inductance Lmd=% [H]", Lmd)
    message ("Stator winding resistance Rs=% [Ohm]", Rs)
    message ("Field winding resistance Rfd=% [Ohm]", Rfd)
    message ("Damper d-axis winding  resistance Rkd=% [Ohm]", Rkd)
    message ("Damper d-axis winding  resistance Rkq=% [Ohm]", Rkq)
    message ("Synchronous electrical angular velocity we0=% [rad/sec]", we0)
    message (" ------------------------REPORT")
   }
  }
#---------------------------------------------------------------------------
# Values section
#---------------------------------------------------------------------------
  values {
    we=p*wm                    # electrical angular velocity

    Ksat=1.0
    ifrem=1e-7
    if (sat_include==yes){
      #------TLU Function Evaluation
      vsat=tlu(2,addr(datap),im)                  # no-load characteristic
      v_rem=tlu(2,addr(datap),0)                  # no-load characteristic
      Lmsat=sqrt(2)*(vsat-v_rem)/((im*k_iex*sat_rpm*math_pi*p/30)+1e-6)
      ifrem=sqrt(2)*v_rem/((sat_rpm*math_pi*p/30)*Lsfd+1e-6)
      Ksat=Lmsat/Lsfd-(Lmsat/Lsfd-1)/2*(1+cos(2*asin((imd+1e-7)/(im+1e-7))))    # saturation coefficient
    }
  #------ Inducatances
    L_as_as = Lls + Ksat*Ls*(a1h*(1 + As3**2 + As5**2) - 0.5*a2h*(1 + 2*As3*(1 + As5))*cos(2*alpha*p))
    L_bs_bs = Lls + Ksat*Ls*(a1h*(1 + As3**2 + As5**2) - 0.5*a2h*(1 + 2*As3*(1 + As5))*cos(2*(-ang + alpha*p)))
    L_cs_cs = Lls + Ksat*Ls*(a1h*(1 + As3**2 + As5**2) - 0.5*a2h*(1 + 2*As3*(1 + As5))*cos(2*(ang + alpha*p)))
    L_as_bs = -0.5*Ksat*Ls*(a1h*(1 - 2*As3**2 + As5**2) + a2h*(1 - As3 - As3*As5)*cos(2*(alpha*p - 0.5*ang)))
    L_as_cs = -0.5*Ksat*Ls*(a1h*(1 - 2*As3**2 + As5**2) + a2h*(1 - As3 - As3*As5)*cos(2*(alpha*p + 0.5*ang)))
    L_bs_cs = -0.5*Ksat*Ls*(a1h*(1 - 2*As3**2 + As5**2) + a2h*(1 - As3*As5 - As3)*cos(2*(alpha*p + (3.0/2.0)*ang)))

    L_as_fd = Ksat*Lsfd*(0.5*(2*a1h + a2h - a2h*Afd3)*sin(alpha*p) - \
            0.5*(a2h - 2*a1h*Afd3 + a2h*Afd5)*As3*sin(3*alpha*p) + \
            0.5*(-(a2h*Afd3) + 2*a1h*Afd5)*As5*sin(5*alpha*p))
    L_bs_fd = Ksat*Lsfd*(-0.5*(2*a1h + a2h - a2h*Afd3)*sin(ang - alpha*p) - \
            0.5*(a2h - 2*a1h*Afd3 + a2h*Afd5)*As3*sin(3*alpha*p) - \
            0.5*(a2h*Afd3 - 2*a1h*Afd5)*As5*sin(5*(ang + alpha*p)))
    L_cs_fd = Ksat*Lsfd*(0.5*(2*a1h + a2h - a2h*Afd3)*sin(ang + alpha*p) - \
            0.5*(a2h - 2*a1h*Afd3 + a2h*Afd5)*As3*sin(3*alpha*p) - \
            0.5*(a2h*Afd3 - 2*a1h*Afd5)*As5*cos(5*(-ang + alpha*p)))

    L_as_kd = Ksat*Lskd*(0.5*(2*a1h + a2h - a2h*Akd3)*sin(alpha*p) - \
            0.5*(a2h - 2*a1h*Akd3 + a2h*Akd5)*As3*sin(3*alpha*p) + \
            0.5*(-(a2h*Akd3) + 2*a1h*Akd5)*As5*sin(5*alpha*p))
    L_bs_kd = Ksat*Lskd*(-0.5*(2*a1h + a2h - a2h*Akd3)*sin(ang - alpha*p) - \
```

```
                0.5*(a2h - 2*a1h*Akd3 + a2h*Akd5)*As3*sin(3*alpha*p) - \
                0.5*(a2h*Akd3 - 2*a1h*Akd5)*As5*sin(5*(ang + alpha*p)))
    L_cs_kd = Ksat*Lskd*(0.5*(2*a1h + a2h - a2h*Akd3)*sin(ang + alpha*p) - \
                0.5*(a2h - 2*a1h*Akd3 + a2h*Akd5)*As3*sin(3*alpha*p) - \
                0.5*(a2h*Akd3 - 2*a1h*Akd5)*As5*cos(5*(-ang + alpha*p)))

    L_as_kq = Ksat*Lskq*(0.5*(2*a1h + a2h*(-1 + Akq3))*cos(alpha*p) + \
                0.5*(-2*a1h*Akq3 + a2h*(-1 + Akq5))*As3*cos(3*alpha*p) + \
                0.5*(a2h*Akq3 - 2*a1h*Akq5)*As5*cos(5*alpha*p))
    L_bs_kq = Ksat*Lskq*(0.5*(2*a1h + a2h*(-1 + Akq3))*cos(ang - alpha*p) - \
                0.5*(a2h + 2*a1h*Akq3 - a2h*Akq5)*As3*cos(3*alpha*p) + \
                0.5*(a2h*Akq3 - 2*a1h*Akq5)*As5*cos(5*(ang + alpha*p)))
    L_cs_kq = Ksat*Lskq*(0.5*(2*a1h + a2h*(-1 + Akq3))*cos(ang + alpha*p) - \
                0.5*(a2h + 2*a1h*Akq3 - a2h*Akq5)*As3*cos(3*alpha*p) + \
                0.5*(a2h*Akq3 - 2*a1h*Akq5)*As5*cos(5*(-ang + alpha*p)))

    L_fd_fd = Llfd + Ksat*Lmfd*(a1h*(1 + Afd3**2 + Afd5**2) + 0.5*a2h*(1 - 2*Afd3*(1 + Afd5)))
    L_kd_kd = Llkd + Ksat*Lmkd*(a1h*(1 + Akd3**2 + Akd5**2) + 0.5*a2h*(1 - 2*Akd3*(1 + Akd5)))
    L_kq_kq = Llkq + Ksat*Lmkq*(a1h*(1 + Akq3**2 + Akq5**2) - 0.5*a2h*(1 - 2*Akq3*(1 - Akq5)))

    L_fd_kd = Ksat*Lfdkd*(a1h*(1 + Afd3*Akd3 + Afd5*Akd5) + 0.5*a2h*(1 - Afd3 - Akd3 - Afd5*Akd3 - Afd3*Akd5))

#------ Rotational inductances
    G_as_as = a2h*(1 + 2*As3*(1 + As5))*Ksat*Ls*sin(2*p*alpha)
    G_bs_bs = a2h*(1 + 2*As3*(1 + As5))*Ksat*Ls*sin(2*(p*alpha - ang))
    G_cs_cs = a2h*(1 + 2*As3*(1 + As5))*Ksat*Ls*sin(2*(p*alpha + ang))
    G_as_bs = -1.0*a2h*(1 - As3 - As3*As5)*Ksat*Ls*sin(2*(p*alpha - 0.5*ang))
    G_as_cs = -1.0*a2h*(1 - As3 - As3*As5)*Ksat*Ls*sin(2*(p*alpha + 0.5*ang))
    G_bs_cs = -1.0*a2h*(1 - As3 - As3*As5)*Ksat*Ls*sin(2*(3.0/2.0*ang + p*alpha))

    G_as_fd = Ksat*Lsfd*(0.5*(2*a1h + a2h - a2h*Afd3)*cos(p*alpha) - \
        1.5*(a2h - 2*a1h*Afd3 + a2h*Afd5)*As3*cos(3*p*alpha) + \
        2.5*(-1.0*a2h*Afd3 + 2*a1h*Afd5)*As5*cos(5*p*alpha))
    G_bs_fd = Ksat*Lsfd*(-1.5*(a2h - 2*a1h*Afd3 + a2h*Afd5)*As3*cos(3*p*alpha) + \
        0.5*(2*a1h + a2h - a2h*Afd3)*cos(p*alpha - ang) - \
        2.5*(a2h*Afd3 - 2*a1h*Afd5)*As5*cos(5*(p*alpha + ang)))
    G_cs_fd = Ksat*Lsfd*(-1.5*(a2h - 2*a1h*Afd3 + a2h*Afd5)*As3*cos(3*p*alpha) + \
        0.5*(2*a1h + a2h - a2h*Afd3)*cos(p*alpha + ang) + \
        2.5*(a2h*Afd3 - 2*a1h*Afd5)*As5*sin(5*(p*alpha - ang)))

    G_as_kd = Ksat*Lskd*(0.5*(2*a1h + a2h - a2h*Akd3)*cos(p*alpha) - \
        1.5*(a2h - 2*a1h*Akd3 + a2h*Akd5)*As3*cos(3*p*alpha) + \
        2.5*(-1.0*a2h*Akd3 + 2*a1h*Akd5)*As5*cos(5*p*alpha))
    G_bs_kd = Ksat*Lskd*(-1.5*(a2h - 2*a1h*Akd3 + a2h*Akd5)*As3*cos(3*p*alpha) + \
        0.5*(2*a1h + a2h - a2h*Akd3)*cos(p*alpha - ang) - \
        2.5*(a2h*Akd3 - 2*a1h*Akd5)*As5*cos(5*(p*alpha + ang)))
    G_cs_kd = Ksat*Lskd*(-1.5*(a2h - 2*a1h*Akd3 + a2h*Akd5)*As3*cos(3*p*alpha) + \
        0.5*(2*a1h + a2h - a2h*Akd3)*cos(p*alpha + ang) + \
        2.5*(a2h*Akd3 - 2*a1h*Akd5)*As5*sin(5*(p*alpha - ang)))

    G_as_kq = Ksat*Lskq*(-0.5*(2*a1h + a2h*(-1 + Akq3))*sin(p*alpha) - \
        1.5*(-2*a1h*Akq3 + a2h*(-1 + Akq5))*As3*sin(3*p*alpha) - \
        2.5*(a2h*Akq3 - 2*a1h*Akq5)*As5*sin(5*p*alpha))
    G_bs_kq = Ksat*Lskq*(1.5*(a2h + 2*a1h*Akq3 - a2h*Akq5)*As3*sin(3*p*alpha) - \
        0.5*(2*a1h + a2h*(-1 + Akq3))*sin(p*alpha - ang) - \
        2.5*(a2h*Akq3 - 2*a1h*Akq5)*As5*sin(5*(p*alpha + ang)))
    G_cs_kq = Ksat*Lskq*(1.5*(a2h + 2*a1h*Akq3 - a2h*Akq5)*As3*sin(3*p*alpha) - \
        2.5*(a2h*Akq3 - 2*a1h*Akq5)*As5*sin(5*(p*alpha - ang)) - \
        0.5*(2*a1h + a2h*(-1 + Akq3))*sin(p*alpha + ang))

    G_fd_fd = 0
    G_kd_kd = 0
    G_kq_kq = 0

    G_fd_kd = 0
#------ Flux linkages
    phias = -1.0*ias*L_as_as - ibs*L_as_bs - ics*L_as_cs + ikq*L_as_kq + (ifd + ifrem)*L_as_fd + ikd*L_as_kd
    phibs = -1.0*ias*L_as_bs - ibs*L_bs_bs - ics*L_bs_cs + ikq*L_bs_kq + (ifd + ifrem)*L_bs_fd + ikd*L_bs_kd
```

```
        phics = -1.0*ias*L_as_cs - ibs*L_bs_cs - ics*L_cs_cs + ikq*L_cs_kq + (ifd + ifrem)*L_cs_fd + ikd*L_cs_kd

        phikq = -1.0*ias*L_as_kq - ibs*L_bs_kq - ics*L_cs_kq + ikq*L_kq_kq
        phifd = -1.0*ias*L_as_fd - ibs*L_bs_fd - ics*L_cs_fd + (ifd + ifrem)*L_fd_fd + ikd*L_fd_kd
        phikd = -1.0*ias*L_as_kd - ibs*L_bs_kd - ics*L_cs_kd + (ifd + ifrem)*L_fd_kd + ikd*L_kd_kd

        visc = Bm*wm

    Te = 0.5*G_as_as*ias**2 + G_as_bs*ias*ibs + 0.5*G_bs_bs*ibs**2 + G_as_cs*ias*ics + G_bs_cs*ibs*ics + \
        0.5*G_cs_cs*ics**2 + G_as_fd*ias*ifd + G_bs_fd*ibs*ifd + G_cs_fd*ics*ifd + 0.5*G_fd_fd*ifd**2 + \
        G_as_kd*ias*ikd + G_bs_kd*ibs*ikd + G_cs_kd*ics*ikd + G_fd_kd*ifd*ikd + 0.5*G_kd_kd*ikd**2 + \
        G_as_kq*ias*ikq + G_bs_kq*ibs*ikq + G_cs_kq*ics*ikq + 0.5*G_kq_kq*ikq**2
    }
#---------------------------------------------------------------------------
# control section
#---------------------------------------------------------------------------
    control_section {
        #--------------------------- mechanical variables
        sample_points ((alpha, mom, Tl),sp_mech)
        newton_step (alpha,ns_mech)
        #--------------------------- electromagnetic variables
        sample_points ((imd, imq, im, iqs, ids, i0s),sp_em)
        sample_points ((ifd, ifd_ex, ikd, ikq, ias, ibs, ics),sp_em) #
        sample_points ((vfd_ex, vas, vbs, vcs),sp_em) #
        #---------------------------- initial conditions
        initial_condition (alpha,deg_to_rad*(ic_alpha))
    }
#---------------------------------------------------------------------------
# Equations section
#---------------------------------------------------------------------------
    equations {
            # equation for calculation magnetising current
            iqs=2/3*(ias*cos(p*alpha)+ibs*cos(p*alpha-ang)+ics*cos(p*alpha+ang))
            ids=2/3*(ias*sin(p*alpha)+ibs*sin(p*alpha-ang)+ics*sin(p*alpha+ang))
            i0s=1/3*(ias+ibs+ics)
            imd = -ids/kfd + ifd + ikd/kkd
            imq = -iqs/kfd + ikq/kkq
            # module of magnetising current
            im=sqrt(imd**2 + imq**2 + (-i0s/kfd)**2)/k_iex

            ifd = ifd_ex*k_iex
            # voltage equations
            ias: vas = -Rs*ias + d_by_dt(phias)
            ibs: vbs = -Rs*ibs + d_by_dt(phibs)
            ics: vcs = -Rs*ics + d_by_dt(phics)
            ifd: vfd_ex = Rex*ifd_ex + d_by_dt(phifd)
            ikd:   0 = Rkd*ikd + d_by_dt(phikd)
            ikq:   0 = Rkq*ikq + d_by_dt(phikq)

            # mechanical equation
            Te = Tl + visc + mom
            mom=d_by_dt(Jw*wm)
            alpha: wm=d_by_dt(alpha)
    }
}
#---------------------------------------------------------------------------
#
# End of the template
#
#---------------------------------------------------------------------------
```

APPENDIX E

Measurements conducted in order to calculate circuit parameters of BSGs: commercial GT40PCz8 and the newly designed machine. The parameters are calculated from three-phase, no-load, sudden-short-circuit test according to [6]. The approximation function is used:

$$i_a(t) = I_{ac}(t)\sin(\omega_r t + \lambda) - I_h(t)\sin(2\omega_r t + \lambda) - I_{dc}(t)\sin(\lambda) \qquad \text{(E.1)}$$

where:

$$I_{ac}(t) = \sqrt{2}E_0\left[\frac{1}{X_d} + \left(\frac{1}{X'_d} - \frac{1}{X_d}\right)e^{-\frac{t}{T'_d}} + \left(\frac{1}{X''_d} - \frac{1}{X'_d}\right)e^{-\frac{t}{T''_d}}\right] \qquad \text{(E.2)}$$

$$I_h(t) = \frac{\sqrt{2}E_0}{2}\left(\frac{1}{X''_d} - \frac{1}{X''_q}\right)e^{-\frac{t}{T_a}} \qquad \text{(E.3)}$$

$$I_{dc}(t) = \frac{\sqrt{2}E_0}{2}\left(\frac{1}{X''_d} + \frac{1}{X''_q}\right)e^{-\frac{t}{T_a}} \qquad \text{(E.4)}$$

are the ac ($I_{ac}(t)$), dc ($I_{dc}(t)$) and second harmonic ($I_h(t)$) components. In case of non-salient pole generator the second harmonic component is not present in approximation function. For mathematical calculation/approximation the Wolfram Mathematica 7.0 software function FindFit was used. This function is searching the value of parameters, in this case transient and subtransient reactances and time constants, to find the best fit of the data to selected expression. It minimalizes the difference between data and approximation using either quasi-Newton method or Levenberg-Marquardt variant of the Gauss-Newton method. The parameters can be limited to certain ranges in order to establish starting point for numeric calculation of this function. The function has a set precision goal witch determine how accurate the approximation is needed to be.

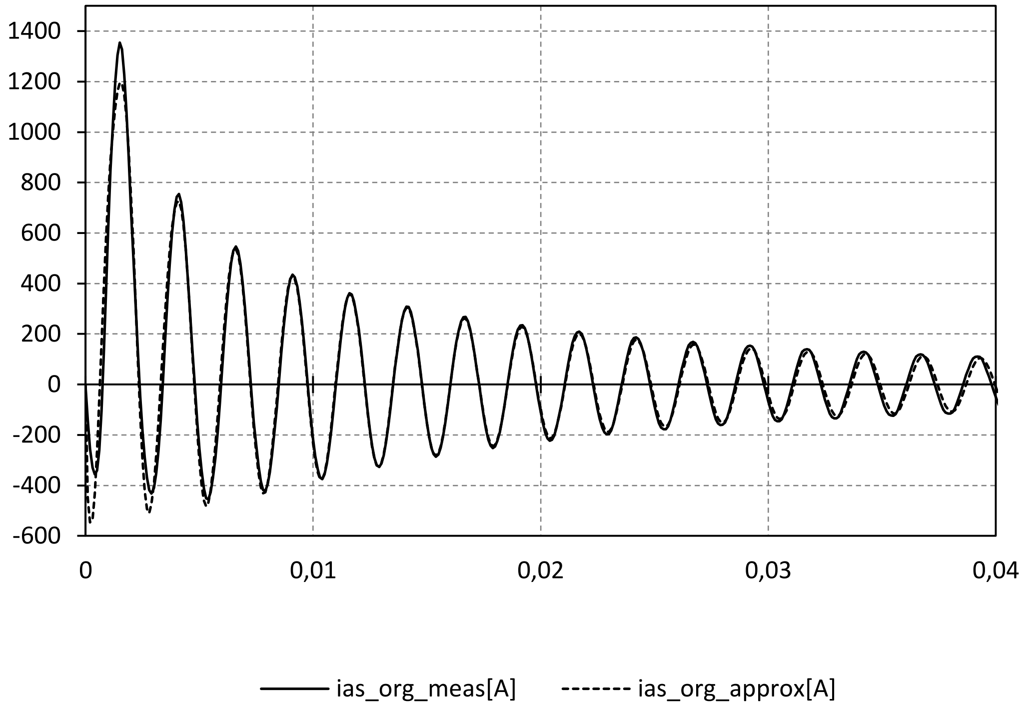

Figure E.1 Commercial GT40PCz8 short circuit transient measurement and approximation

Based on short circuit measurement presented on figure E.1 the calculated value of direct axis synchronous reactance is:

$$E_0 = 122[V] \tag{E.5}$$

$$I_z = 52[A] \tag{E.6}$$

$$X_d = \frac{E_0}{I_z} \qquad X_d = \frac{122}{52} = 2.35[\Omega] \tag{E.7}$$

$$X'_d = 0.22[\Omega] \tag{E.8}$$

$$X''_d = 0.14[\Omega] \tag{E.9}$$

$$X''_q = 0.19[\Omega] \tag{E.10}$$

$$T'_d = 0.013[s] \tag{E.11}$$

$$T''_d = 0.002[s] \tag{E.12}$$

$$T_a = 0.002[s] \tag{E.13}$$

APPENDIX F

Designed test bench is based on DC motor and synchronous belt transmission:

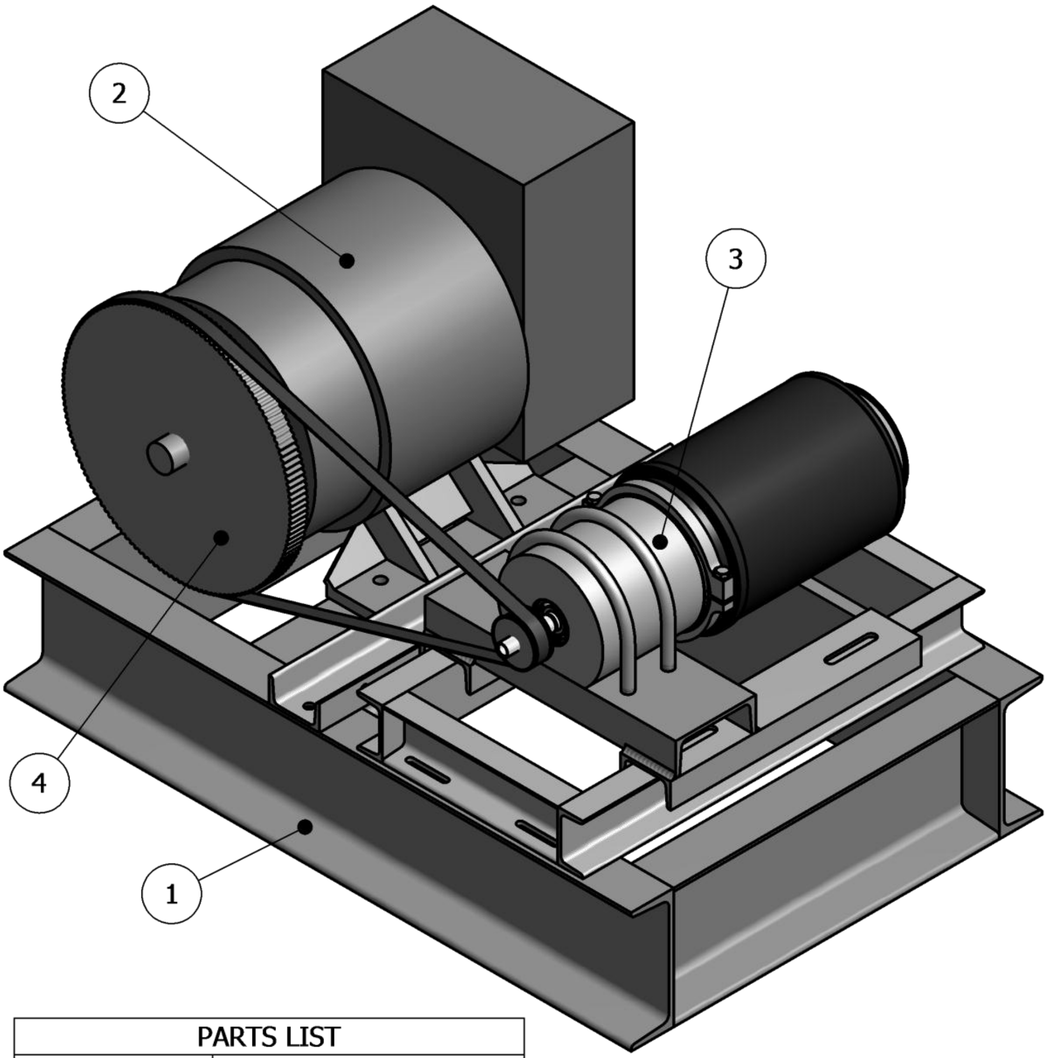

PARTS LIST	
ITEM NUMBER	PART NAME
1	Base
2	DC Motor
3	BSG
4	Belt Transmission

Figure F.1 Proposed test bench

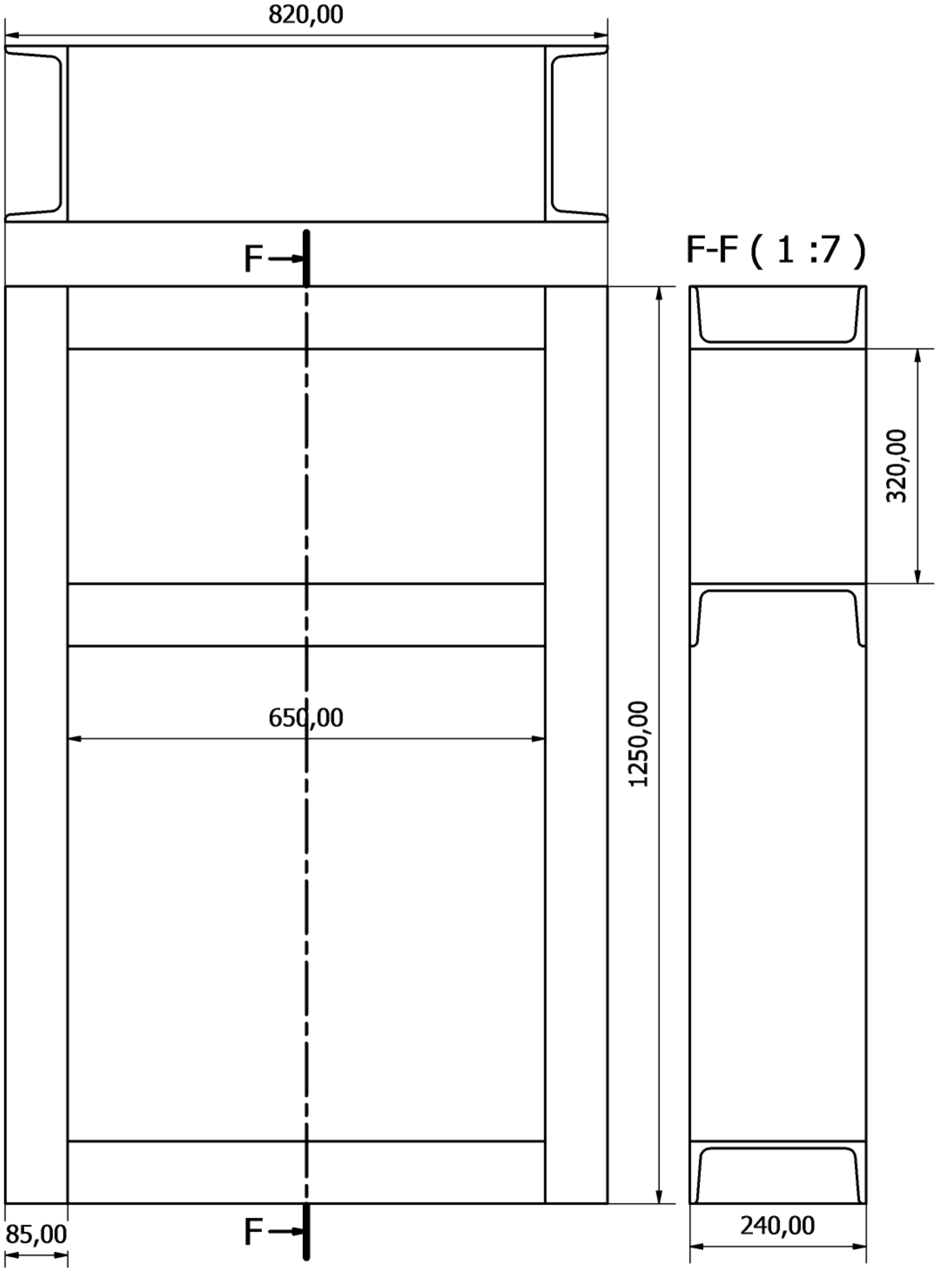

Figure F.2 Base for the test bench

The base of the test bench was designed based on existing one used in different laboratory.

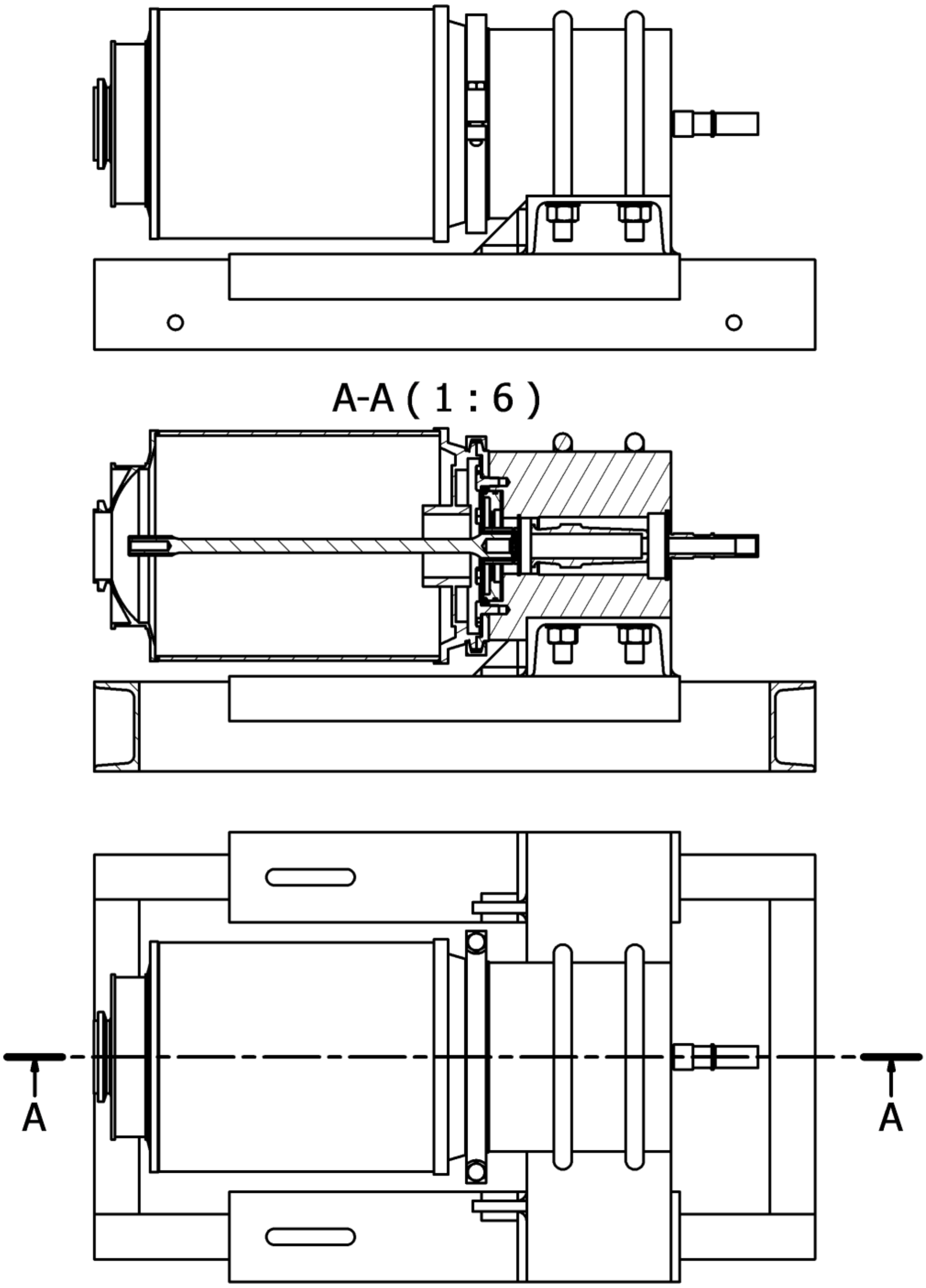

Figure F.3 BSG stand for the test bench

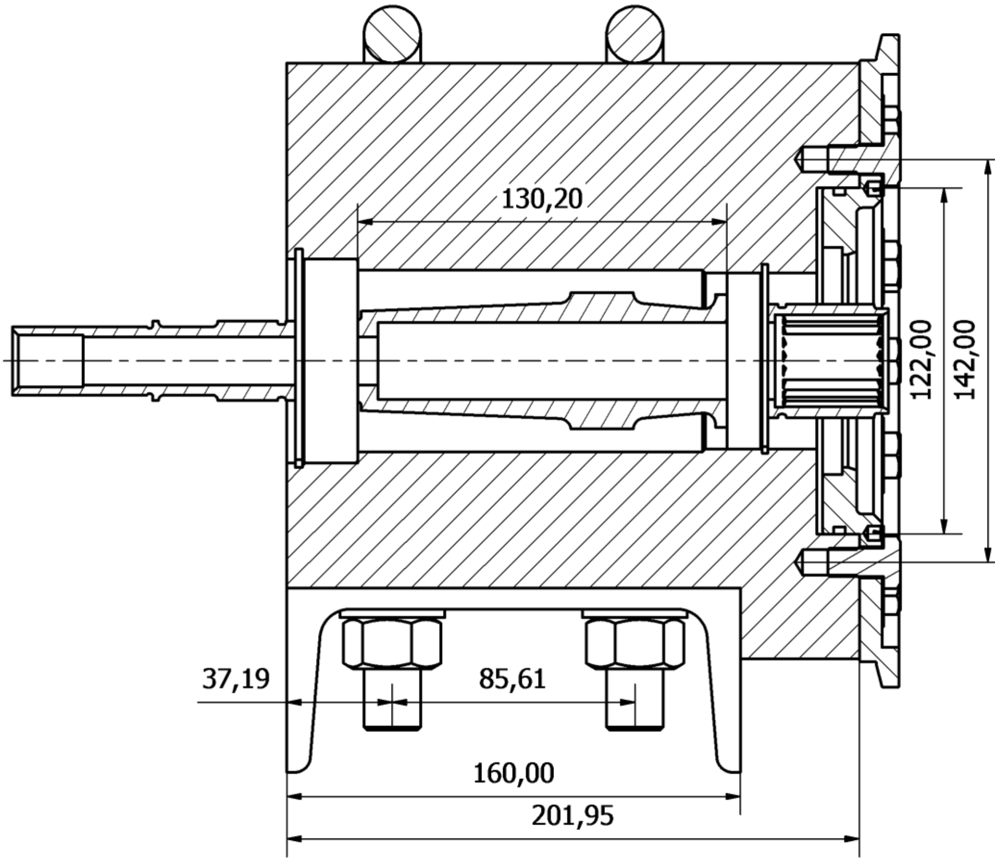

Figure F.4 BSG stand external shaft housing for the test bench

Figure F.3 and figure F.4 shows proposed shield mounting of the GT40PCz8 enclosure.

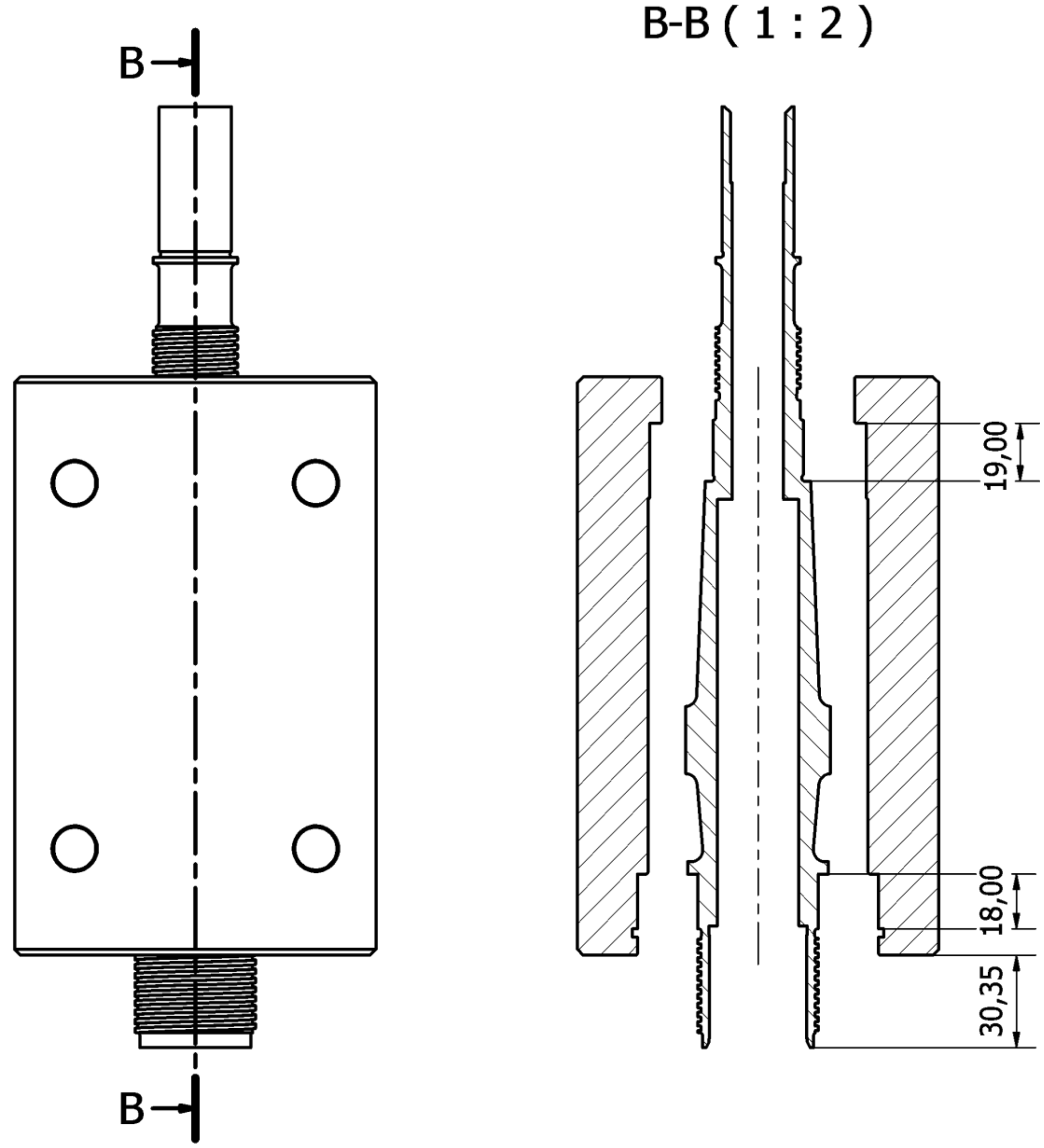

Figure F.5 Modified BSG stand external shaft housing for the test bench

After the proposed solution on figure F.4 turned out to be difficult and expensive to make a different solution for the housing of the external shaft was proposed (figure F.5).

Figure F.6 shows report from Gates Company Design Flex software. The selected transmission was the verified by BDI Poland, from whom the transmission components were bought.

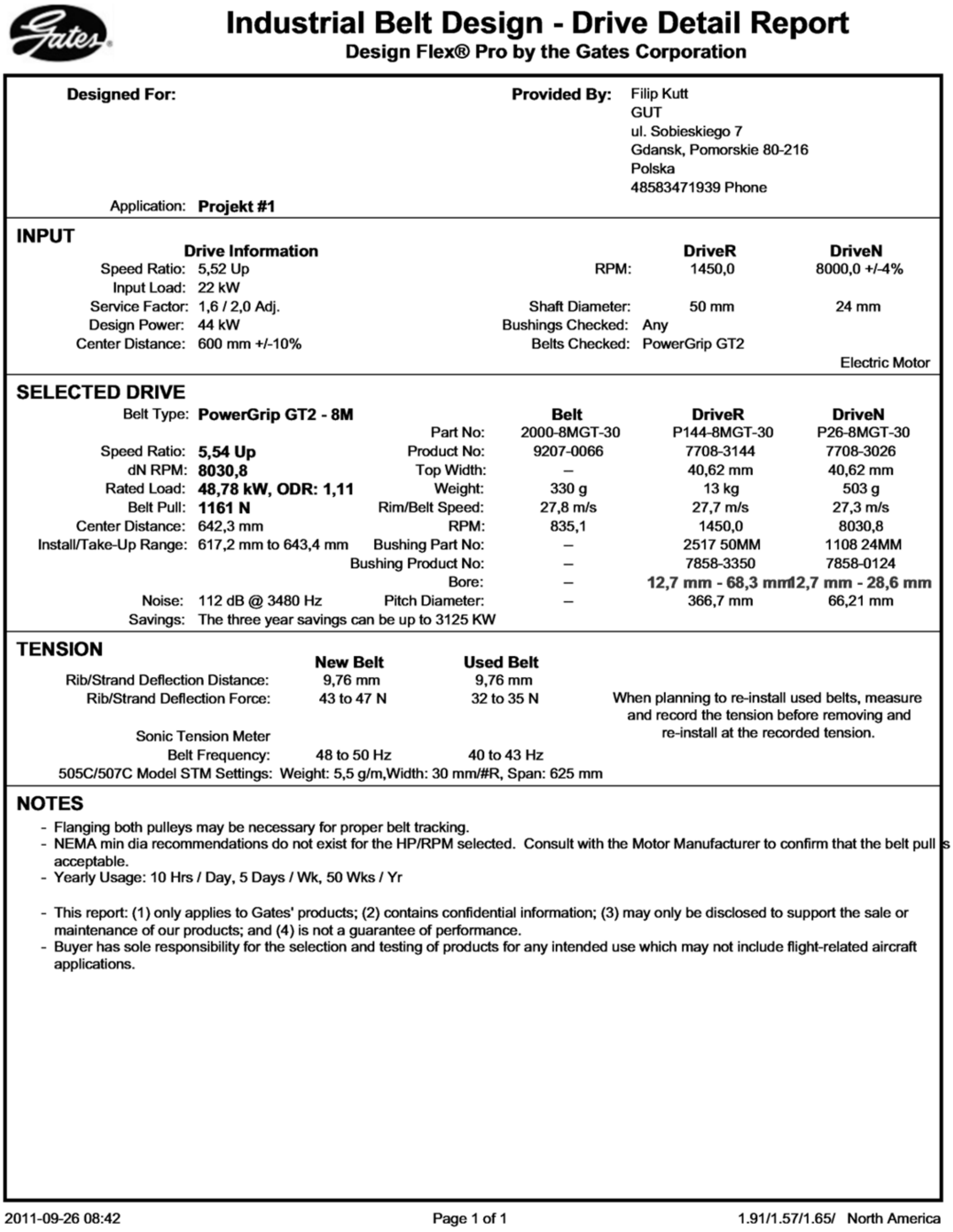

Industrial Belt Design - Drive Detail Report

Design Flex® Pro by the Gates Corporation

Designed For:

Provided By:
Filip Kutt
GUT
ul. Sobieskiego 7
Gdansk, Pomorskie 80-216
Polska
48583471939 Phone

Application: **Projekt #1**

INPUT

Drive Information			DriveR	DriveN
Speed Ratio:	5,52 Up	RPM:	1450,0	8000,0 +/-4%
Input Load:	22 kW			
Service Factor:	1,6 / 2,0 Adj.	Shaft Diameter:	50 mm	24 mm
Design Power:	44 kW	Bushings Checked:	Any	
Center Distance:	600 mm +/-10%	Belts Checked:	PowerGrip GT2	
				Electric Motor

SELECTED DRIVE

			Belt	DriveR	DriveN
Belt Type:	**PowerGrip GT2 - 8M**	Part No:	2000-8MGT-30	P144-8MGT-30	P26-8MGT-30
Speed Ratio:	**5,54 Up**	Product No:	9207-0066	7708-3144	7708-3026
dN RPM:	**8030,8**	Top Width:	–	40,62 mm	40,62 mm
Rated Load:	**48,78 kW, ODR: 1,11**	Weight:	330 g	13 kg	503 g
Belt Pull:	**1161 N**	Rim/Belt Speed:	27,8 m/s	27,7 m/s	27,3 m/s
Center Distance:	642,3 mm	RPM:	835,1	1450,0	8030,8
Install/Take-Up Range:	617,2 mm to 643,4 mm	Bushing Part No:	–	2517 50MM	1108 24MM
		Bushing Product No:	–	7858-3350	7858-0124
		Bore:	–	**12,7 mm - 68,3 mm**	**12,7 mm - 28,6 mm**
Noise:	112 dB @ 3480 Hz	Pitch Diameter:	–	366,7 mm	66,21 mm
Savings:	The three year savings can be up to 3125 KW				

TENSION

	New Belt	Used Belt
Rib/Strand Deflection Distance:	9,76 mm	9,76 mm
Rib/Strand Deflection Force:	43 to 47 N	32 to 35 N
Sonic Tension Meter		
Belt Frequency:	48 to 50 Hz	40 to 43 Hz

When planning to re-install used belts, measure and record the tension before removing and re-install at the recorded tension.

505C/507C Model STM Settings: Weight: 5,5 g/m,Width: 30 mm/#R, Span: 625 mm

NOTES

- Flanging both pulleys may be necessary for proper belt tracking.
- NEMA min dia recommendations do not exist for the HP/RPM selected. Consult with the Motor Manufacturer to confirm that the belt pull is acceptable.
- Yearly Usage: 10 Hrs / Day, 5 Days / Wk, 50 Wks / Yr

- This report: (1) only applies to Gates' products; (2) contains confidential information; (3) may only be disclosed to support the sale or maintenance of our products; and (4) is not a guarantee of performance.
- Buyer has sole responsibility for the selection and testing of products for any intended use which may not include flight-related aircraft applications.

2011-09-26 08:42 Page 1 of 1 1.91/1.57/1.65/ North America

Figure F.6 Designed belt transmission (Gates Company Design Flex software)

REFERENCES

Books

[1] A. Boboń, J. Kudła, and A. Żywiec, *Parametry elektromagnetyczne maszyny synchronicznej. Wykorzystanie metody elementów skończonych.*, Z Kleszczewski, Ed. Gliwice, Polska: Wydawnictwo Politechniki Śląskiej, 1998.

[2] C. Concordia, *Synchronous machines, theory and performance*.: Wiley, 1951.

[3] A. Demenko, *Obwodowe modele układów z polem elektromagnetycznym*. Poznań: Wydawnictwo Politechniki Poznańskiej, 2006.

[4] J. F. Gieras, *Advancements in Electric Machines*.: Springer, 2009.

[5] J. F. Gieras, *Permanent Magnet Motor Technology: Design and Applications*, 3rd ed.: CRC Press, 2009.

[6] IEEE Power Engineering Society, *IEEE Guide for Synchronous Generator Modeling Practices and Applications in Power System Stability Analyses*. New York, USA: The Institute of Electrical and Electronics Engineers, Inc., 2002.

[7] P. C. Krause, O. Wasynczuk, and S. D. Sudhoff, *Analysis of Electric Machinery and Drive Systems*, Secorrd Edition ed., M. E. El-Hawary, Ed. New York, United States of America: A John Wiley & Sons, inc., 2002.

[8] J. Kudła, *Modele matematyczne maszyn elektrycznych prądu przemiennego uwzględniające nasycenie magnetyczne rdzeni*. Gliwice, Polska: Wydawnictwo Politechniki Ślaskiej, 2005.

[9] J. Meisel, *Principles of Electromechanical Energy Conversion*.: Krieger Pub Co, 1984.

[10] I. Moir and A. Seabridge, *Aircraft Systems. Mechanical, electrical, and avionics subsystems integration.*, Third Edition ed. Southern Gate, Chichester, West Sussex PO19 8SQ, England: John Wiley & Sons Ltd, 2008.

[11] W. Paszek, *Stany nieustalone maszyn elektrycznych prądu przemiennego*, M Storożyńska, Ed. Warszawa, Polska: Wydawnictwa Naukowo-Techniczne, 1986.

[12] M. Pehnt et al., *Micro Cogeneration: Towards Decentralized Energy Systems*, A. Oelschläger, Ed. Berlin, Germany: Springer-Verlag, 2006.

[13] A. Pochanke, *Modele obwodowo-polowe pośrednio sprzężone silników bezzstykowych z uwarunkowaniami zasilania*. Warszawa, Polska: Oficyna Wydawnicza Politechniki Warszawskiej, 1999.

[14] J. Pyrhönen, T. Jokinen, and V. Hrabovcová, *Design of Rotating Electrical Machines*, Firsf Edition ed., translated by Hanna Niemelä, Ed. Southern Gate, Chichester, West Sussex, PO19 8SQ, United Kingdom: John Wiley & Sons, Ltd., 2008.

[15] T. J. Sobczyk, *Metodyczne aspekty modelowania matematycznego maszyn indukcyjnych*, M Kasperska, Ed. Warszawa, Polska: Wydawnictwa Naukowo-Techniczne, 2004.

[16] Synopsys, *Saber® MAST Language User Guide. Version Z-2007.03*. U.S.A., 2007.

[17] A. Wilk, *Modelowanie obwodowo-polowe transformatorów trakcyjnych w aspekcie diagnostyki opartej na modelu referencyjnym*, R Szymkiewicz, Ed. Gdańsk, Polska: Wydawnictwo Politechniki Gdańskiej, 2012.

Articles in journals and periodicals

[18] M. A. Abdel-Halim and C. D. Manning, "Modelling saturation of laminated salient-pole synchronous machines," *Electric Power Applications, IEE Proceedings B*, vol. 134, no. 4, pp. 215-223, July 1987.

[19] N. C. Adcock and A. W. Ford, "Excitation systems for a.c. aircraft generators," *Proceedings of the IEE - Part A: Power Engineering*, vol. 103, no. 1, pp. 206-211, May 1956.

[20] D. C. Aliprantis, S. D. Sudhoff, and B. T. Kuhn, "A Synchronous Machine Model With Saturation and Arbitrary Rotor Network Representation," *Energy Conversion, IEEE Transactions on*, vol. 20, no. 3, pp. 584-594, Sep. 2005.

[21] D. C. Aliprantis, S. D. Sudhoff, and B. T. Kuhn, "Experimental Characterization Procedure for a Synchronous Machine Model With Saturation and Arbitrary Rotor Network Representation," *Energy Conversion, IEEE Transactions on*, vol. 20, no. 3, pp. 595-603, Sep. 2005.

[22] D. C. Aliprantis, O. Wasynczuk, and C. D. Rodriguez Valdez, "A Voltage-Behind-Reactance Synchronous Machine Model With Saturation and Arbitrary Rotor Network Representation," *Energy Conversion, IEEE Transactions on*, vol. 23, no. 2, pp. 499-508, Jun. 2008.

[23] T. D. Batzel and D. C. Swanson, "Prognostic Health Management of Aircraft Power Generators," *Aerospace and Electronic Systems, IEEE Transactions on*, vol. 45, no. 2, pp. 473-482, Apr. 2009.

[24] Boeing, "787 No-Bleed Systems: Saving Fuel and enhancing operational efficiencies," vol. 28, no. Qtr_04, pp. 6-11, 2007.

[25] V. Brandwajn, "Representation of Magnetic Saturation in the Synchronous Machine Model in an Electro-Mlagnetic Transients Program," *Power Apparatus and Systems, IEEE Transactions on*, vol. PAS-99, no. 5, pp. 1996-2002, Sept. 1980.

[26] Jie Chang and Anhua Wang, "New VF-power system architecture and evaluation for future aircraft," *Aerospace and Electronic Systems, IEEE Transactions on*, vol. 42, no. 2, pp. 527-539, Apr. 2006.

[27] P. L. Chapman, S. D. Sudhoff, and C. A. Whitcomb, "Multiple reference frame analysis of non-sinusoidal brushless DC drives," *Energy Conversion, IEEE Transactions on*, vol. 14, no. 3, pp. 440-446, Sep. 1999.

[28] K. A. Corzine, B. T. Kuhn, S. D. Sudhoff, and H. J. Hegner, "An improved method for incorporating magnetic saturation in the q-d synchronous machine model," *Energy Conversion, IEEE Transactions on*, vol. 13, no. 3, pp. 270-275, Sep. 1998.

[29] F. P. de Mello and L. N. Hannett, "Representation of Saturation in Synchronous Machines," *Power Systems, IEEE Transactions on*, vol. 1, no. 4, pp. 8-14, Nov. 1986.

[30] Nhut-Quang Dinh and J. Arrillaga, "A salient-pole generator model for harmonic analysis," *Power Systems, IEEE Transactions on*, vol. 16, no. 4, pp. 609-615, Nov. 2001.

[31] M. E. Elbuluk and M. D. Kankam, "Potential starter/generator technology for future aerospace application," *Aerospace and Electronic Systems Magazine*, vol. 11, no. 10, pp. 17-24, Oct. 1996.

[32] A. M. El-Serafi, A. S. Abdallah, M. K. El-Sherbiny, and E. H. Badawy, "Experimental study of the saturation and the cross-magnetizing phenomenon in saturated synchronous machines," *Energy Conversion, IEEE Transactions on*, vol. 3, no. 4, pp. 815-823, Dec. 1988.

[33] A. M. El-Serafi and N. C. Kar, "Methods for determining the intermediate-axis saturation Characteristics of salient-pole synchronous Machines from the measured D-axis Characteristics," *Energy Conversion, IEEE Transactions on*, vol. 20, no. 1, pp. 88-97, Mar. 2005.

[34] R. Escarela-Perez, T. Niewierowicz, and E. Campero-Littlewood, "A study of the variation of synchronous machine parameters due to saturation: a numerical approach," *Electric Power Systems Research*, vol. 72, no. 1, pp. 1-11, Nov. 2004.

[35] J. Faiz and I. Tabatabaei, "Extension of winding function theory for nonuniform air gap in electric machinery," *Magnetics, IEEE Transactions on*, vol. 38, no. 6, pp. 3654-3657, Nov. 2002.

[36] A. W. Ford, "Brushless Generators for Aircraft - a Review of Current Developments," *Proceedings of the IEE - Part A: Power Engineering*, vol. 109, no. 47, pp. 437-452, October 1962.

[37] T. Fukami et al., "Steady-State Analysis of a Permanent-Magnet-Assisted Salient-Pole Synchronous Generator," *Energy Conversion, IEEE Transactions on*, vol. 25, no. 2, pp. 388-393, Jun. 2010.

[38] K. E. Hallenius, P. Vas, and J. E. Brown, "The analysis of a saturated self-excited asynchronous generator," *Energy Conversion, IEEE Transactions on*, vol. 6, no. 2, pp. 336-345, Jun. 1991.

[39] D. Hamdi-Sepen, "Saturation Effects in Synchronous Machines," *Power Apparatus and Systems, Part III. Transactions of the American Institute of Electrical Engineers*, vol. 73, no. 2, pp. 1349-1353, Jan. 1954.

[40] R. G. Harley, D. J. N. Limebeer, and E. Chirricozzi, "Comparative study of saturation methods in synchronous machine models," *Electric Power Applications, IEE Proceedings B*, vol. 127, no. 1, pp. 1-7, January 1980.

[41] K. Hirayama, "Practical detailed model for generators," *Energy Conversion, IEEE Transactions on*, vol. 10, no. 1, pp. 105-110, Mar. 1995.

[42] M. Houwing, R. R. Negenborn, and B. De Schutter, "Demand Response With Micro-CHP Systems," *Proceedings of the IEEE*, vol. 99, no. 1, pp. 200-213, Jan. 2011.

[43] I. Iglesias, L. Garcia-Tabares, and J. Tamarit, "A d-q model for the self-commutated synchronous machine considering the effects of magnetic saturation," *Energy Conversion, IEEE Transactions on*, vol. 7, no. 4, pp. 768-776, Dec. 1992.

[44] I. Kamwa, R. Wamkeue, and X. Dai-Do, "General approaches to efficient d-q simulation and model translation for synchronous machines: a recap," *Electric Power Systems Research*, vol. 42, no. 3, pp. 173-180, Sep. 1996.

[45] R. J. Kennett, "Integrated drive generators for aircraft," *Electronics and Power*, vol. 17, no. 2, pp. 73-76, February 1971.

[46] P. C. Krause, "Method of Multiple Reference Frames Applied to the Analysis of Symmetrical Induction Machinery," *Power Apparatus and Systems, IEEE Transactions on*, vol. PAS-87, no. 1, pp. 218-227, Jan. 1968.

[47] P. C. Krause and J. R. Hake, "Method of Multiple Reference Frames Applied to the Analysis of a Rectifier - Inverter Induction Motor Drive," *Power Apparatus and Systems, IEEE Transactions on*, vol. PAS-88, no. 11, pp. 1635-1641, Nov. 1969.

[48] F. Kutt, M. Michna, P. J. Chrzan, and M. Ronkowski, "Nonlinear model of a synchronous generator for analysis of more electric aircraft power systems," *Zeszyty Problemowe : Maszyny Elektryczne*, no. 83, pp. 173-178, 2009.

[49] F. Kutt, M. Michna, M. Ronkowski, and P. J. Chrzan, "Polyharmonic model of synchronous generator for analysis of autonomous power generation systems.," *Zeszyty Problemowe : Maszyny Elektryczne*, no. 92, pp. 109-114, 2011.

[50] F. Kutt and M. Ronkowski, "Koncepcja i symulacja polowa generatora o zmiennej częstotliwości. Zastosowanie w autonomicznych systemach elektroenergetycznych.," *Zeszyty Problemowe : Maszyny Elektryczne*, no. 86, pp. 169-173, 2010, English title: Conception and field simulations of a variable frequency generator. Application for autonomous power generation system.

[51] E. Levi, "Modelling of magnetic saturation in smooth air-gap synchronous machines," *Energy Conversion, IEEE Transactions on*, vol. 12, no. 2, pp. 151-156, Jun 1997.

[52] E. Levi, "Saturation modelling in d-q axis models of salient pole synchronous machines," *Energy Conversion, IEEE Transactions on*, vol. 14, no. 1, pp. 44-50, May 1999.

[53] E. Levi and V. A. Levi, "Impact of dynamic cross-saturation on accuracy of saturated synchronous machine models," *Energy Conversion, IEEE Transactions on*, vol. 15, no. 2, pp. 224-230, Jun. 2000.

[54] A. Maalouf, L. Idkhajine, S. Le Ballois, and E. Monmasson, "Field programmable gate array-based sensorless control of a brushless synchronous starter generator for aircraft application," *Electric Power Applications, IET*, vol. 5, no. 1, pp. 181-192, Jan. 2011.

[55] W Matulewicz, "Analiza metod wyznaczania parametrów jawnobiegunowych generatorów z uwzględnieniem mozliwości wspomagania komputerowego," *Zaszyty Naukowe Politechniki Gdańskiej, Elektryka 64*, no. 423, 1988.

[56] W Matulewicz, "Właściwości wyznaczania parametrów jawnobiegunowych prądnic synchronicznych," *Zeszyty Naukowe Politechniki Gdańskiej, Elektryka 64*, vol. 423 Suplement, 1991.

[57] A. Medina and J. Arrillaga, "Analysis of transformer-generator interaction in the harmonic domain," *IEE Proceedings - Generation, Transmission and Distribution*, vol. 141, no. 1, pp. 38-46, January 1994.

[58] M. Michna, F. Kutt, P. J. Chrzan, and M. Ronkowski, "Modelling and analysis of a synchronous generator in more electric aircraft power system using Synopsys/Saber simulator," *Prace Instytutu Elektrotechniki*, no. 240, pp. 31-46, 2009.

[59] R. H. Park, "Two-reaction theory of synchronous machines generalized method of analysis-part I," *Transactions of the American Institute of Electrical Engineers*, vol. 48, no. 3, pp. 716-727, July 1929.

[59] R H Park, "Two-reaction theory of synchronous machines generalized method of analysis-part I," *Transactions of the American Institute of Electrical Engineers*, vol. 48, no. 3, pp. 716-727, July 1929.

[60] R. H. Park, "Two-reaction theory of synchronous machines-II," *Transactions of the American Institute of Electrical Engineers*, vol. 52, no. 2, pp. 352-354, June 1933.

[60] R H Park, "Two-reaction theory of synchronous machines-II," *Transactions of the American Institute of Electrical Engineers*, vol. 52, no. 2, pp. 352-354, June 1933.

[61] N. Patin et al., "Control of a Hybrid Excitation Synchronous Generator for Aircraft Applications," *Industrial Electronics, IEEE Transactions on*, vol. 55, no. 10, pp. 3772-3783, Oct. 2008.

[62] A. Paweletz, "Efficient Energy Conversion through the Evolution of the Electrical Machine Topology," *Przegląd Elektrotechniczny*, no. 6, pp. 49-58, 2008.

[63] S. D. Pekarek, E. A. Walters, and B. T. Kuhn, "An efficient and accurate method of representing magnetic saturation in physical-variable models of synchronous machines," *Energy Conversion, IEEE Transactions on*, vol. 14, no. 1, pp. 72-79, Mar. 1999.

[64] P. P. Predd, "A Power Plant for the Home," *Spectrum, IEEE*, vol. 44, no. 4, pp. 14-15, Apr. 2007.

[65] H. Rehaoulia, H. Henao, and G.A. Capolino, "Modeling of synchronous machines with magnetic saturation," *Electric Power Systems Research*, vol. 77, no. 5-6, pp. 652-659, Apr. 2007.

[66] M. Ronkowski, "Circuit-oriented models of electrical machines for simulation of converter systems," *Zesz. Nauk. Pol. Gdańskiej*, vol. 523, no. Elektryka nr LXXVIII, 1995.

[67] J. A. Rosero, J. A. Ortega, E. Aldabas, and L. Romeral, "Moving towards a more electric aircraft," *Aerospace and Electronic Systems Magazine*, vol. 22, no. 3, pp. 3-9, March 2007.

[68] A. Semlyen, E. Acha, and J. Arrillaga, "Newton-type algorithms for the harmonic phasor analysis of nonlinear power circuits in periodical steady state with special reference to magnetic nonlinearities," *IEEE Transactions on Power Delivery*, vol. 3, no. 3, pp. 1090-1098, July 1988.

[69] A. Semlyen, J. F. Eggleston, and J. Arrillaga, "Admittance Matrix Model of a Synchronous Machine for Harmonic Analysis," *IEEE Transactions on Power Systems*, vol. 2, no. 4, pp. 833-839, November 1987.

[70] K. Srivastava and B. Berggren, "Simulation of synchronous machines in phase coordinates including magnetic saturation," *Electric Power Systems Research*, vol. 56, no. 3, pp. 177-183, Dec. 2000.

[71] S. D. Sudhoff, "Multiple reference frame analysis of a multistack: variable-reluctance stepper motor," *Energy Conversion, IEEE Transactions on*, vol. 8, no. 3, pp. 418-424, Sep. 1993.

[72] S. D. Sudhoff, "Multiple reference frame analysis of an unsymmetrical induction machine," *Energy Conversion, IEEE Transactions on*, vol. 8, no. 3, pp. 425-432, Sep. 1993.

[73] G. B. Sugden, "Oil-cooled a.c. generators for aircraft - present trends," *Students' Quarterly Journal*, vol. 40, no. 160, pp. 128-133, June 1970.

[74] I. Tabatabaei, J. Faiz, H. Lesani, and M. T. Nabavi-Razavi, "Modeling and Simulation of a salient-pole synchronous Generator with dynamic eccentricity using modified winding function theory," *Magnetics, IEEE Transactions on*, vol. 40, no. 3, pp. 1550-1555, May 2004.

[75] S. A. Tahan and I. Kamwa, "A two-factor saturation model for synchronous machines with multiple rotor circuits," *Energy Conversion, IEEE Transactions on*, vol. 10, no. 4, pp. 609-616, Dec. 1995.

[76] H. A. Toliyat and N. A. Al-Nuaim, "Simulation and detection of dynamic air-gap eccentricity in salient-pole synchronous machines," *Industry Applications, IEEE Transactions on*, vol. 35, no. 1, pp. 86-93, Jan/Feb 1999.

[77] V. V. Vadher, I. R. Smith, and S. Williams, "Mathematical Modeling of a VSCF Aircraft Generating System," *Aerospace and Electronic Systems, IEEE Transactions on*, vol. AES-22, no. 5, pp. 573-582, Sept. 1986.

[78] L. Wang, J. Jatskevich, and H. W. Dommel, "Re-examination of Synchronous Machine Modeling Techniques for Electromagnetic Transient Simulations," *Power Systems, IEEE Transactions on*, vol. 22, no. 3, pp. 1221-1230, Aug. 2007.

[79] G. Xie and R. S. Ramshaw, "Nonlinear Model of Synchronous Machines with Saliency," *Energy Conversion, IEEE Transactions on*, vol. EC-1, no. 3, pp. 198-204, Sept. 1986.

[80] J. Yong, G. Kostro, F. Kutt, M. Michna, and M. Ronkowski, "Conception and design of a hybrid exciter for brushless synchronous generator. Application for autonomous electrical power systems.," *Zeszyty Naukowe Politechniki Śląskiej. Elektryka.*, no. 1(213), pp. 7-21, 2010.

Conference proceedings

[81] F. M. Bruck and F. A. Himmelstoss, "Modelling and simulation of a synchronous machine," in *Computers in Power Electronics, 1998. 6th Workshop on*, 1998, pp. 81-86.

[82] A. Campeanu and M. Stiebler, "Modeling of saturation in salient pole synchronous machines," in *Optimization of Electrical and Electronic Equipment (OPTIM), 2010 12th International Conference on*, 2010, pp. 258-263.

[83] F. Delhasse and F. Biais, "High power starter generators for airliners," in *Changes in Aeronautical and Space Systems*, 2006.

[84] A. M. El-Serafi and N. C. Kar, "A new method for calculating the q-axis saturation characteristics of salient-pole synchronous machines," in *Electrical and Computer Engineering, 2001. Canadian Conference on*, 2001, pp. 557-562.

[85] W. Gao, A. P. S. Meliopoulos, E. V. Solodovnik, and R. Dougal, "A nonlinear model for studying synchronous machine dynamic behavior in phase coordinates," in *Industrial Technology, 2005. ICIT 2005. IEEE International Conference on*, 2005, pp. 1092-1097.

[86] J. F. Gieras, "PM synchronous generators with hybrid excitation systems and voltage control Capabilities: A review," in *XXth International Conference on Electrical Machines*, 2012, pp. 2573-2579.

[87] S. Guha and N. C. Kar, "A New Method of Modeling Magnetic Saturation in Electrical Machines," in *Electrical and Computer Engineering, 2006. CCECE '06. Canadian Conference on*, 2006, pp. 1094-1097.

[88] J. D. Harrison, "Micro combined heat and power: potential impact on the electricity supply industry," in *Electricity Distribution, 2001. Part 1: Contributions. CIRED. 16th International Conference and Exhibition on (IEE Conf. Publ No. 482) vol.4*, 2001, p. 5.

[89] D. Hiramatsu et al., "Study of saturation characteristic of equivalent circuits for cylindrical synchronous machine," in *Power and Energy Society General Meeting, 2010 IEEE*, 2010.

[90] R. Jablko, C. Saniter, R. Hanitsch, and S. Holler, "Technical and economical comparison of micro CHP systems," in *Future Power Systems, 2005 International Conference on*, 2005, p. 6.

[91] I. Jadric, D. Borojevic, and M. Jadric, "A simplified model of a variable speed synchronous generator loaded with diode rectifier," in *Power Electronics Specialists Conference, 1997. PESC '97 Record., 28th Annual IEEE*, 1997, pp. 497-502.

[92] N. C. Kar and A. M. El-Serafi, "A new model for the saturated synchronous machines using the intermediate-axis saturation characteristics," in *Electrical and Computer Engineering, 2002. IEEE CCECE 2002. Canadian Conference on*, 2002, pp. 172-177.

[93] N. C. Kar and A. M. El-Serafi, "Effect of the main flux saturation on the transient short-circuit performance of synchronous machines," in *Electrical and Computer Engineering, 2005. Canadian Conference on*, 2005, pp. 629-632.

[94] S. A. Kharitonov and M. V. Riabchitsky, "New Structure of Autonomous Power System," in *Computational Technologies in Electrical and Electronics Engineering, 2008. SIBIRCON 2008. IEEE Region 8 International Conference on*, 2008, pp. 192-193.

[95] F. Kutt, M. Michna, M. Ronkowski, and G. Kostro, "Prototype of a High Speed Multi-Pole Non-Salient Brushless Synchronous Generator for application in Autonomous Power Generation Systems," in *More Electric Aircraft*, Bordeaux, 2012.

[96] T. A. Lipo, T. Komatsu, and K. Shinohara, "Simulation of a salient pole synchronous machine with Both field pole and stator core saturation," in *Electrical Machines and Power Electronics, 2007. ACEMP '07. International Aegean Conference on*, 2007, pp. 331-336.

[97] P. H. Mellor, S. G. Burrow, T. Sawata, and M. Holme, "A wide speed range permanent magnet generator for future embedded aircraft generation systems," in *Electric Machines and Drives Conference, 2003. IEMDC'03. IEEE International*, 2003, pp. 1308-1313.

[98] M. Michna and F. Kutt, "Modeling of generator performance of BLDC machine using Mathematica software," in *Prace Naukowe Instytutu Maszyn, Napędów i Pomiarów Elektrycznych Politechniki Wrocławskiej. Studia i Materiały*, Wrocław, 2008, pp. 582-587.

[99] M. Michna, F. Kutt, M. Ronkowski, and P. J. Chrzan, "Nonlinear Model of High Speed Multi-Pole Non-Salient Brushless Synchronous Generator for Analysis Of More Electric Aircraft Power Systems," in *More Electric Aircraft*, Bordeaux, 2012.

[100] K. Muehlbauer and D. Gerling, "Two-generator-concepts for electric power generation in More Electric Aircraft Engine," in *Electrical Machines (ICEM), 2010 XIX International Conference on*, 2010, pp. 1-5.

[101] M. Olaiya and N. Buchan, "High power variable frequency generator for large civil aircraft," in *IEE Colloquium on Electrical Machines and Systems for the More Electric Aircraft (Ref. No. 1999/180)*, 1999, pp. 3/1-3/4.

[102] R. E. J. Quigley, "More Electric Aircraft," in *Applied Power Electronics Conference and Exposition, 1993. APEC '93. Conference Proceedings 1993., Eighth Annual*, Mar. 1993, pp. 906-911.

[103] O. Rodriguez and A. Medina, "Fast periodic steady state solution of a synchronous machine model in phase coordinates incorporating the effects of magnetic saturation and hysteresis," in *Power Engineering Society Winter Meeting vol.3*, 2001, pp. 1431-1436.

[104] J. Spetlik and J. Tlusty, "Analysis of distributed generation sources using abc synchronous machine model," in *Future Power Systems, 2005 International Conference on*, 2005, p. 6.

[105] P. Staszewski, "Field method of performance characteristics shaping of electrical machine by construction modifications," in *Second International Conference on Computation in Electromagnetics*, 1994, pp. 243-246.

[106] A. Tantawy, X. Koutsoukos, and G. Biswas, "Aircraft AC generators: Hybrid system modeling and simulation," in *Prognostics and Health Management, 2008. PHM 2008. International Conference on*, 2008, pp. 1-11.

[107] F. Wang, "A nonlinear saturation model for salient-pole synchronous machines in high performance drive applications," in *Industry Applications Conference, 2003. 38th IAS Annual Meeting. Conference Record of the*, 2003, pp. 906-910.

[108] L. Wang, J. Jatskevich, N. Ozog, and A. Davoudi, "A Simple Explicit Method of Representing Magnetic Saturation of Salient-Pole Synchronous Machines in Both Rotor Axes Using Matlab-Simulink," in *Electrical and Computer Engineering. CCECE 2007. Canadian Conference on*, 2007.

[109] J. A. Weimer, "The role of electric machines and drives in the more electric aircraft," in *Electric Machines and Drives Conference, 2003. IEMDC'03. IEEE International*, 2003, pp. 11-15.

Reports

[110] T. Jomier - Airbus Operations S.A.S., "MOET Technical Report (deliverable D0.02.3)," MOET Consortium Partners, Technical Report MOET-0.02-AF-DEL-PublicReport-0001-09-R1.0, 2009, http://www.eurtd.com/moet/.

[111] G. R. Simader, R. Krawinkler, and G. Trnka, "Micro CHP systems: state-of-the-art," Austrian Energy Agency, Vienna, Deliverable 8 (D8) of Green Lodges Project (EIE/04/252/S07.38608) Final Report 2006.

Internet sites

[112] European Conference on More Electric Aircraft MEA 2012, 20-21 November, 212, Bordeaux, France. [Online]. http://www.mea2012.eu/

[113] MOET Project office. (2009, December) More Open Electrical Technologies MOET FP6 project. [Online]. http://www.eurtd.com/moet/

[114] Synopsys. (2012, March) Synopsys.com. [Online]. http://www.synopsys.com

[115] Wiesław Lis, EPiMP Maszyny Elektryczne. (2012, December) [Online]. http://www.epimp.com.pl